Thermal Hall Effect Measurements Using Strontium Titanate Microthermometers

by

Colin Tinsman

A dissertation submitted in partial fulfillment
of the requirements for the degree of
Doctor of Philosophy
(Applied Physics)
in the University of Michigan
2019

Doctoral Committee:

Professor Lu Li, Chair
Professor Çagliyan Kurdak
Associate Professor Kai Sun
Associate Professor Zhaohui Zhong

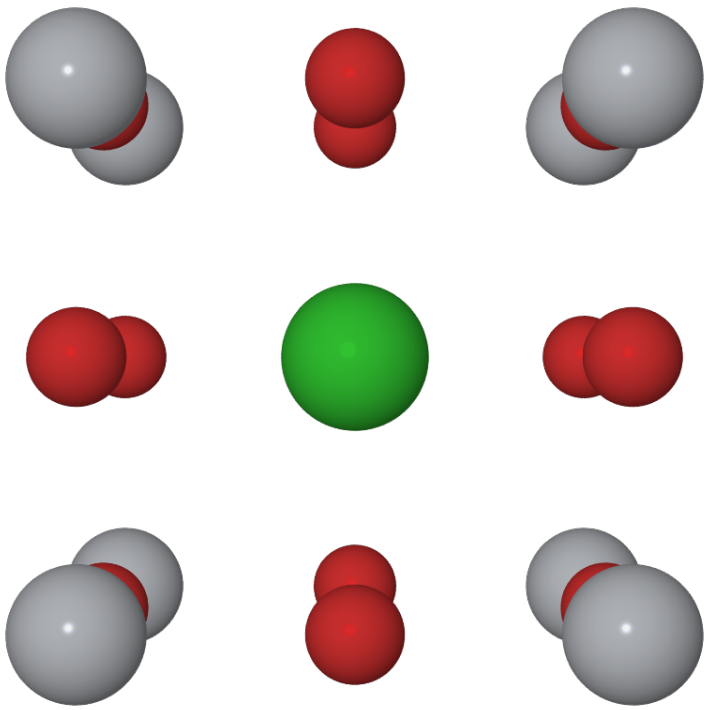

Colin Tinsman

tinsmanc@umich.edu

ORCID iD: 0000-0002-1439-7999

DEDICATION

For Matthew, who I deeply wish could be here to see this.

ACKNOWLEDGMENTS

First, I would like I would like to thank my advisor Lu Li, for his guidance in starting this project and providing the context for how it would contribute to the field as a whole. I would also like to thank the postdoctoral researchers Gang Li and Ziji Xiang for their hands-on experience in performing thermal transport measurements and in keeping all the low-temperature systems running. I also must thank my fellow Li group graduate students Ben Lawson, Tomoya Asaba, Fan Yu, Lu Chen, and Dmitri Mihaliov for their support as well as the intellectual stimulation I got both from having them work on my project and from me working on theirs. I should also thank Çagliyan Kurdak as well as his students Yun Suk Eo and Alexa Rakoski for their collaboration over the years, as well as Trevor Bailey for discussions about thermal measurements in general. Since these measurements would not be possible without materials to work on, I should thank Ctirad Uher for providing the bismuth crystals, as well as Sara Haravifard for providing the strontium copper borate samples. Finally, I must thank my parents Michele and Robert Tinsman for helping support me at every stage of my academic journey.

TABLE OF CONTENTS

LIST OF FIGURES

LIST OF TABLES

LIST OF APPENDICES

ABSTRACT

Thermal measurements are an important tool for experimental condensed matter physics. They are the most general methods available: any excitation in a solid will carry energy, and thus heat. Such measurements require accurate and precise temperature readings at multiple points on a crystal, often only a few millimeters apart. This is especially important when making thermal Hall effect measurements, which require precision in intense magnetic fields that can interfere with resistive thermometers. We have exploited the strongly temperature dependent dielectric permittivity of strontium titanate to make capacitive thermometers which are not subject to this interference. To test these thermometers, thermal Hall effect measurements were carried out on crystalline bismuth. Bismuth is one of the best known semimetals, a material which hosts both electrons and holes with high mobility. With the strontium titante microthermometers, we were able to conduct measurements up to 10 T and at temperatures down to 40 K. A large thermal Hall coefficient is measured, indicative of high mobility carriers. Another application of these techniques is thermal measurements of frustrated magnets. These systems often have itinerant excitations which do not carry charge, making thermal measurements all the more important. We discuss our measurements on strontium copper borate, in which pairs of spin-1/2 sites are paired up in strongly coupled dimers. The magnetic excitations of this system are mobile triplet states, called triplons. It has been predicted that these triplet bands could have non-trivial topology, making strontium copper borate a bosonic topological insulator, and resulting in a specific thermal Hall effect signal. Experimental measurements in this system fail to find this signal, casting doubt on this theory. However, we observe magnetic field dependent thermal conductivity at temperatures below 1 K, where the triplet excitations should be

frozen out. This may be related to another phenomena found in this material: the formation of spin superlattices.

CHAPTER 1

The Thermal Hall Effect

1.1 Thermal Hall Conductivity in General

The thermal Hall effect is the thermal analogue of the much more well known (electrical) Hall effect. As the Hall effect can be understood as generalizing the electrical conductivity σ to a tensor in Ohm's law:

$$\mathbf{j} = \sigma \mathbf{E} \Rightarrow \begin{pmatrix} j_x \\ j_y \end{pmatrix} = \begin{pmatrix} \sigma_{xx} & \sigma_{xy} \\ -\sigma_{xy} & \sigma_{yy} \end{pmatrix} \begin{pmatrix} E_x \\ E_y \end{pmatrix}$$

the thermal Hall effect generalizes the thermal conductivity κ to a tensor in Fourier's law:

$$\mathbf{q} = -\kappa \nabla u \Rightarrow \begin{pmatrix} q_x \\ q_y \end{pmatrix} = - \begin{pmatrix} \kappa_{xx} & \kappa_{xy} \\ -\kappa_{xy} & \kappa_{yy} \end{pmatrix} \begin{pmatrix} \partial_x u \\ \partial_y u \end{pmatrix}$$

where u is the temperature field and $\mathbf{q}$ is the heat current. Before discussing the origin of of the thermal Hall conductivity κ_{xy}, we should establish how heat flows through such a material. Let's assume we have an isotropic material (i.e. $\kappa_{xx} = \kappa_{yy}$). The conductivity tensor can be rewritten as

$$\begin{pmatrix} \kappa_{xx} & \kappa_{xy} \\ -\kappa_{xy} & \kappa_{xx} \end{pmatrix} = \kappa_{xx} \begin{pmatrix} 1 & \kappa_{xy}/\kappa_{xx} \\ -\kappa_{xy}/\kappa_{xx} & 1 \end{pmatrix} = \kappa_{xx} \begin{pmatrix} 1 & \tan\theta_H \\ -\tan\theta_H & 1 \end{pmatrix}$$

where $\theta_H = \arctan \kappa_{xy}/\kappa_{xx}$ is the definition of the thermal Hall angle. Writing down the heat equation, and splitting the conductivity into its symmetric and antisymmetric parts:

$$\begin{aligned} -\nabla \cdot \mathbf{q} = c\rho\partial_t u = \nabla \cdot (\kappa \nabla u) &= \nabla \cdot (\kappa_{xx}(\mathbb{I} + \kappa_{\text{antisym}})\nabla u) \\ &= \kappa_{xx}\nabla^2 u + \kappa_{xx}\nabla \cdot (\kappa_{\text{antisym}}\nabla u) \end{aligned}$$

where c is the heat capacity and ρ is the mass density. Writing out the κ_{antisym} term explicitly:

$$\begin{aligned} \begin{pmatrix} \partial_x & \partial_y \end{pmatrix} \begin{pmatrix} 0 & \tan\theta_H \\ -\tan\theta_H & 0 \end{pmatrix} \begin{pmatrix} \partial_x u \\ \partial_y u \end{pmatrix} &= \begin{pmatrix} \partial_x & \partial_y \end{pmatrix} \begin{pmatrix} \tan\theta_H \partial_x u \\ -\tan\theta_H \partial_y u \end{pmatrix} \\ &= \tan\theta_H \partial_{xy} u - \tan\theta_H \partial_{xy} u = 0 \end{aligned}$$

Thus the equation reduces to the isotropic heat equation, $c\rho\partial_t u = \kappa_{xx}\nabla^2 u$! Thus, it might seem like the thermal Hall conductivity would have no effect on the flow of heat through the material. Indeed, when studying the heat equation, the conductivity tensor κ is usually assumed to be symmetric. However, if we impose the Neumann boundary condition $g = -\hat{n} \cdot \mathbf{q}$ for some known function g, the effect of the thermal Hall conductivity can be seen:

$$\begin{aligned} -\hat{n} \cdot \mathbf{q} &= \hat{n} \cdot \kappa \nabla u \\ &= \kappa_{xx} \begin{pmatrix} n_x & n_y \end{pmatrix} \begin{pmatrix} 1 & \tan\theta_H \\ -\tan\theta_H & 1 \end{pmatrix} \begin{pmatrix} \partial_x u \\ \partial_y u \end{pmatrix} \\ &= \kappa_{xx} \begin{pmatrix} n_x & n_y \end{pmatrix} \begin{pmatrix} \partial_x u + \tan\theta_H \partial_y u \\ -\tan\theta_H \partial_x u + \partial_y u \end{pmatrix} \\ &= \kappa_{xx} n_x (\partial_x u + \tan\theta_H \partial_y u) + \kappa_{xx} n_y (-\tan\theta_H \partial_x u + \partial_y u) \end{aligned}$$

Taking for example $\hat{n} = (1, 0)$ and $g = 0$ (perfectly insulating boundary conditions):

$$0 = -\hat{n} \cdot \mathbf{q} = \kappa_{xx}(\partial_x u + \tan\theta_H \partial_y u) \Rightarrow \partial_x u = -\tan\theta_H \partial_y u$$

In general, the derivative normal to the boundary is specified in terms of the transverse derivative and the thermal Hall angle.

In order to see what this kind of boundary condition does in practice, we can simulate a material with a thermal Hall coefficient using the finite element method. For simplicity, we will look first at steady state solutions (i.e. those with $\partial_t u = 0$). Thus we will need to solve the elliptic partial differential equation $-\nabla \cdot (\kappa \nabla u) = 0$. We start by expressing this equation in weak form by multiplying it by a test function v and integrating over the function's domain Ω:

$$-\nabla \cdot (\kappa \nabla u) = 0 \Rightarrow -\int_\Omega \nabla \cdot (\kappa \nabla u) v dx = 0$$

The function $u(x, y)$ is said to solve the weak problem if this equation holds for all functions $v(x, y)$, where $v(x, y) = 0$ anywhere we have specified u on the boundary (i.e. imposed Dirichlet boundary conditions). By integrating by parts, this becomes:

$$-\int_\Omega \nabla \cdot (\kappa \nabla u) v dx = \int_\Omega \kappa \nabla u \cdot \nabla v dx - \int_{\partial\Omega} (\hat{n} \cdot \kappa \nabla u) v ds$$

where the second integral on the right hand side is over the boundary of Ω. The second integral can be rewritten in terms of the Neumann boundary condition:

$$-\int_{\partial\Omega} (\hat{n} \cdot \kappa \nabla u) v ds = \int_{\partial\Omega} g v ds$$

and so we have cast the problem in a form suitable for solving with the finite element

method, in terms of the bilinear form

$$a(u,v) = \int_\Omega \kappa \nabla u \cdot \nabla v dx$$

and the linear form

$$L(v) = -\int_{\partial\Omega} gv ds$$

as $a(u,v) = L(v)$. By discretizing the problem using standard methods over a suitable mesh, the problem reduces to solving a linear system. There are many references which go into detail on finite element analysis, but I used [1] which covered the specific Python library I used to run the following simulations. The python code to generate these figures is reproduced in appendix A.

This dependence of the Hall signal on the particular boundary condition should not be surprising to anyone who is experienced making electrical transport measurements. Indeed, DC electrical transport can be modeled using an analogous partial differential equation

$$\nabla \cdot (\sigma \nabla V) = 0$$

where V is the electric potential and σ is the conductivity tensor. The typical geometry for a (non-thermal) Hall effect measurement involves measuring the voltage at four points on the sample, with the edges of the sample electrically insulating. This gives us the same Neumann boundary condition as before, via Ohm's law rather than Fourier's law:

$$\hat{n} \cdot \mathbf{j} = \hat{n} \cdot \sigma \nabla V = 0$$

where **i** is the current density. If instead we wish to eliminate the effect of the Hall conductivity, a different geometry known as a Corbino disk is used [2]. This geometry consists of two large electrodes in the shape of concentric rings, leaving an annular region where current flows through the sample of interest. In effect, this clamps the voltage at each point

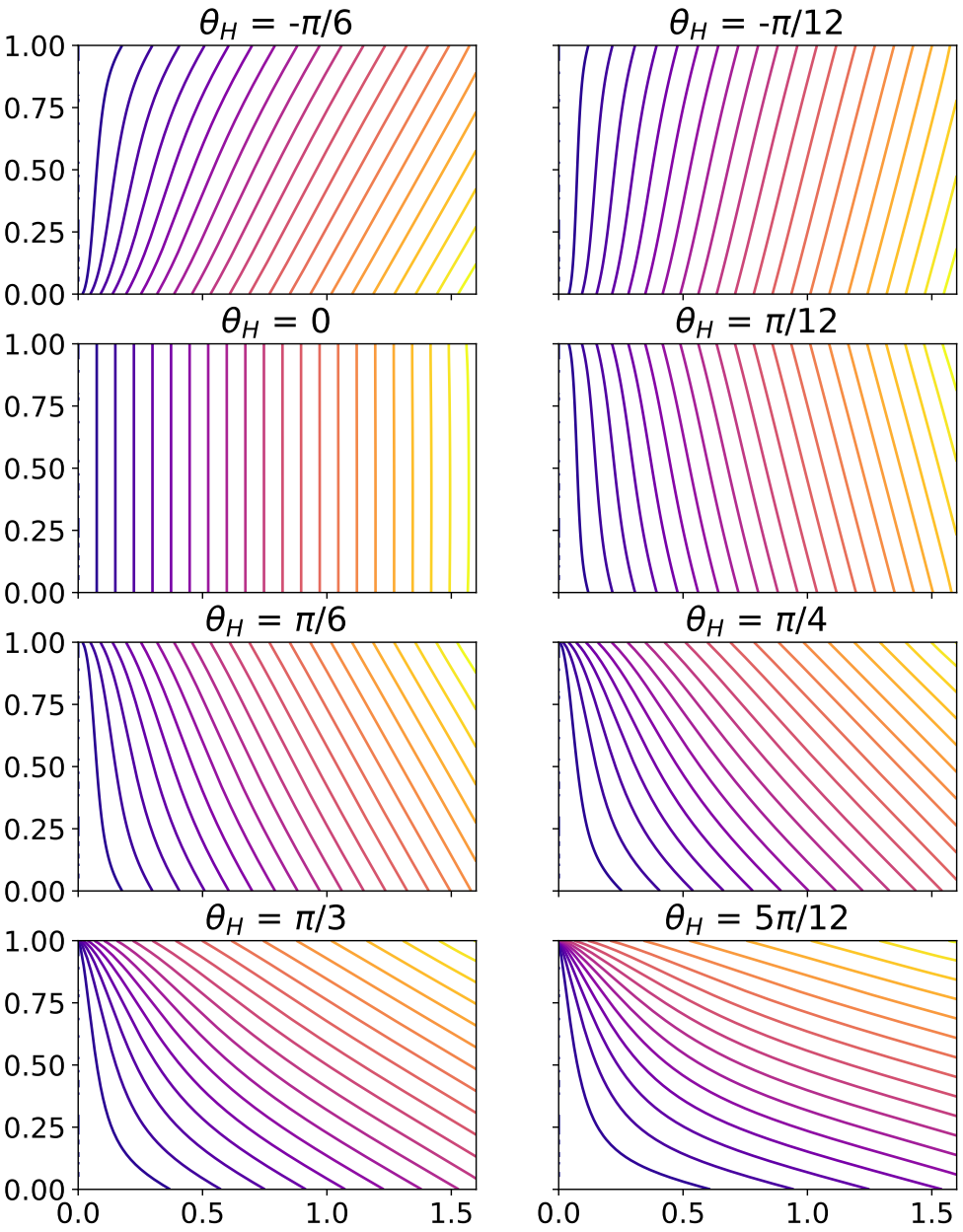

Figure 1.1: Thermal Hall Isotherms. The left side of each simulation is held to $T = 0$, the right has a heater with unit power, and the upper and lower edges are insulating.

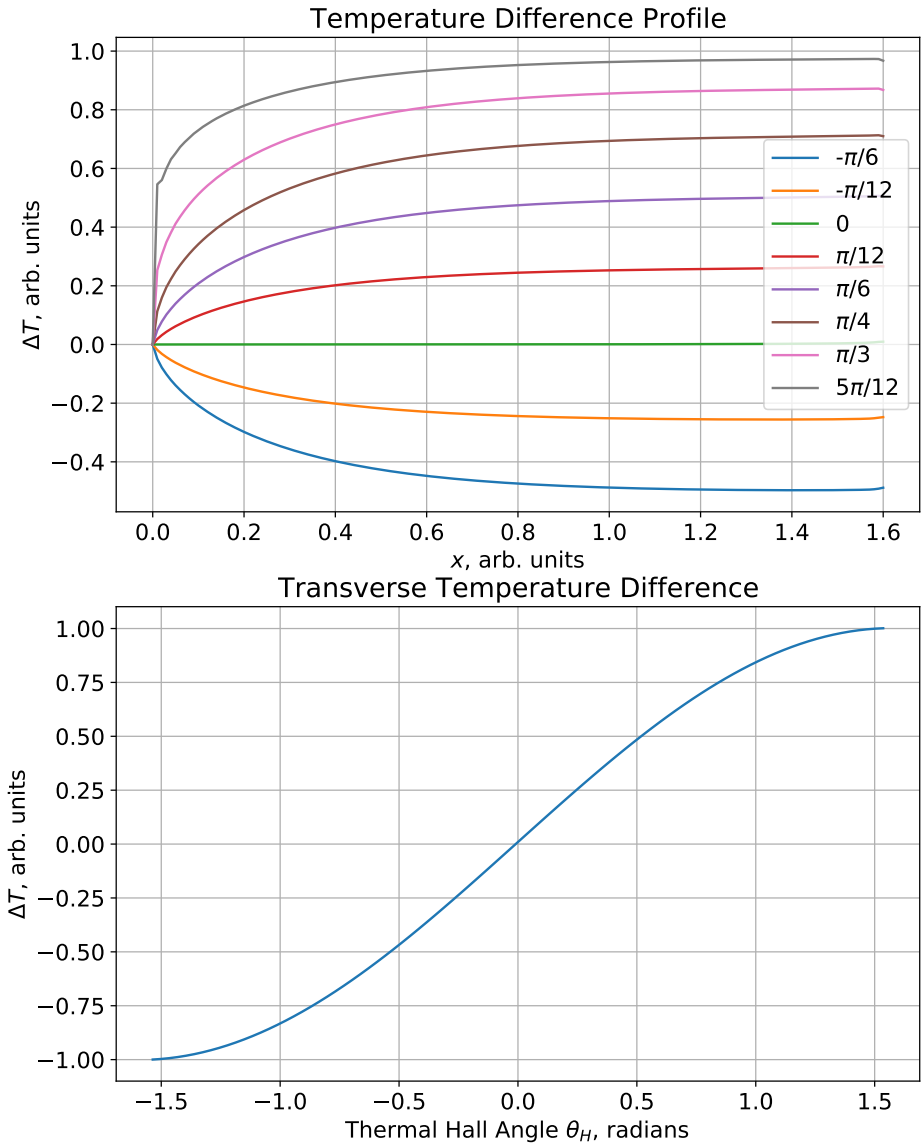

Figure 1.2: Thermal Hall Temperature Profiles. Top: Temperature difference across the sample transverse to the applied heat (y axis in figure 1.1) at different points along the sample for different thermal Hall angles. Note that for each angle, the temperature difference approaches a constant value far from the cold finger. Bottom: The same temperature difference at a fixed position as a function of the thermal Hall angle. Note that for experimentally relevant values of the thermal Hall angle ($\theta_H \approx 1^\circ$), ΔT is proportional to θ_H.

Figure 1.3: Electrical Transport Geometries. Left: Hall bar geometry. Current is fed in through the gold contacts on the left and right, and the voltage measured at the black points. The upper and lower boundaries are insulating. Right: Corbino disk. The voltage is measured between the inner and outer contacts (gold). Since there is no insulating boundary, the Hall conductivity is suppressed.

on the two rings (to values which depend on the applied current and the conductivity of the sample), effectively giving us a Dirichlet boundary condition (i.e. specifying the voltage) at every point on the boundary. This suppresses the effect of the Hall conductivity, and thus this type of of measurement is good for isolating the magnetoresistance of a sample.

This analogy between thermal and electrical transport begs the question: Could one measure thermal conductivity with a "thermal Corbino disk"? Maybe, but in practice it would never be necessary for a very simple reason: in real materials, the thermal Hall angle is rarely more than a few degrees. Table 1.1 lists a few selected thermal Hall angles reported in the literature. In all of these materials, the thermal Hall conductivity is the result of some kind of (quasi-)particle excitation. In the next section, we will discuss the thermal Hall conductivity of electrons in metals. However, the last two entries in the table list thermal Hall conductivities which are the result of excitations which carry spin but not charge. It is this kind of experiment where measurements of the thermal Hall effect have particular scientific value, since such quasiparticles cannot be directly observed using electrical transport methods. Such a measurement will be the subject of chapter 3.

Material	$\tan\theta_H$	Reference
Bi	0.2	[3]
InSb	0.02	[4]
HgSe	0.03	[5]
$YBa_2Cu_3O_{6.63}$	0.12	[6]
$Lu_2V_2O_7$	2×10^{-3}	[7]
$Tb_2Ti_2O_7$	5×10^{-3}	[8]

Table 1.1: Thermal Hall angles, reported as $\tan\theta_H$, for various materials. Naturally, the specific value is a function of applied field and overall temperature, only the largest reported angle is reproduced here.

1.2 Origin of the Thermal Hall Conductivity in Metals

The thermal Hall effect in metals has been observed experimental fact for more than a century. In historical literature, it is known as the Righi-Leduc effect, named after the Italian and French (respectively) physicists who discovered it [9]. In elementary terms, it can be understood as the corollary of two basic phenomena in solid state physics: the Wiedemann-Franz law, and the (electronic) Hall effect. The Wiedemann-Franz law refers to the experimental observation, reproducible in theoretical models such as the classical Drude model, that the ratio between the thermal and electrical conductivities of a metal is more or less proportional to the temperature:

$$\frac{\kappa}{\sigma} = LT, L \approx 2.22 \times 10^{-8}\ \mathrm{W\Omega/K^2}$$

where L is sometimes called the Lorenz constant. Typically κ and σ are assumed to be scalars, but within the semiclassical theory of conduction in metals, we can rigorously derive a relation in terms of the conductivity tensors while also producing a reasonably accurate value for L. I will summarize the derivation given in chapter 13 of Ashcroft and Mermin here [10].

Take for example a region of a solid small enough that we can assume it has uniform temperature. Assuming that the only thing carrying heat and entropy in to or out of this region is the electrons, we can use the basic thermodynamic identity in the grand canonical

ensemble ($TdS = dU - \mu dN$, where U is the total energy, N is the number of electrons, and μ is the chemical potential) to express the heat current $\mathbf{j}^q$ in terms of the energy and number currents ($\mathbf{j}^{\mathcal{E}}$ and $\mathbf{j}^n$, respectively):

$$\mathbf{j}^q = T\mathbf{j}^s = \mathbf{j}^{\mathcal{E}} - \mu\mathbf{j}^n$$

The currents on the right hand side can be expressed in terms of an integral over the Brillouin zone:

$$\begin{pmatrix}\mathbf{j}^{\mathcal{E}}\\ \mathbf{j}^n\end{pmatrix} = \sum_n \int \frac{d\mathbf{k}}{4\pi^3}\begin{pmatrix}\mathcal{E}_n(\mathbf{k})\\ 1\end{pmatrix}\mathbf{v}_n(\mathbf{k})g_n(\mathbf{k})$$

Where n indexes the bands, $\mathcal{E}_n$ is the band structure, $\mathbf{v}_n$ is the electron velocity, and g_n is the electron distribution function. The heat current can be derived in a straightforward way from these two expressions:

$$\mathbf{j}^q = \sum_n \int \frac{d\mathbf{k}}{4\pi^3}[\mathcal{E}_n(\mathbf{k}) - \mu]\mathbf{v}_n(\mathbf{k})g_n(\mathbf{k})$$

Now we consider the modification of g in the case where a uniform electric field $\mathbf{E}$, uniform magnetic field H, and temperature gradient $-\nabla T$:

$$g(\mathbf{k}) = g^0(\mathbf{k}) - \tau(\mathcal{E}(\mathbf{k}))\left(-\frac{\partial f}{\partial \mathcal{E}}\right)\overline{\mathbf{v}}(\mathbf{k})\left[-e\mathcal{E} + \frac{\mathcal{E}(\mathbf{k}) - \mu}{T}(-\nabla T)\right]$$

where f is the Fermi-Dirac distribution, τ is the relaxation time,

$$\mathcal{E} = \mathbf{E} + \frac{\nabla\mu}{e}$$

and

$$\overline{\mathbf{v}}_n(\mathbf{k}) = \int_{-\infty}^{0} \frac{dt}{\tau_n(\mathbf{k})} e^{t/\tau_n(\mathbf{k}}\mathbf{v}_n(\mathbf{k}(t))$$

is the velocity of the electron averaged over its entire history weighted exponentially by the relaxation time. This is necessary due to the presence of a magnetic field, required in

order to observe the thermal Hall effect. We will now use this new distribution function to construct the heat and electrical currents. The electrical conductivity is given by

$$\sigma^{(n)}(\mathcal{E}) = e^2 \int \frac{d\mathbf{k}}{4\pi^3} \tau_n(\mathcal{E}_n(\mathbf{k})) \mathbf{v}_n(\mathbf{k}) \overline{\mathbf{v}}_n(\mathbf{k}) \left(-\frac{\partial f}{\partial \mathcal{E}} \right)_{\mathcal{E}=\mathcal{E}_n(\mathbf{k})}$$

Define the quantities

$$\begin{aligned}
\mathcal{L}^{(\alpha)} &= \int d\mathcal{E} (\mathcal{E} - \mu)^\alpha \sigma(\mathcal{E}) \\
\mathbf{L}^{11} &= \mathcal{L}^{(0)} \\
\mathbf{L}^{21} &= T\mathbf{L}^{12} = -\frac{1}{e}\mathcal{L}^{(1)} \\
\mathbf{L}^{22} &= \frac{1}{e^2 T}\mathcal{L}^{(2)}
\end{aligned}$$

the current densities can be written straightforwardly as

$$\begin{aligned}
\mathbf{j} &= \mathbf{L}^{11}\mathcal{E} + \mathbf{L}^{12}(-\nabla T) \\
\mathbf{j}^q &= \mathbf{L}^{21}\mathcal{E} + \mathbf{L}^{22}(-\nabla T)
\end{aligned}$$

Now, we will use some assumptions valid for metals to make these integrals more tractable. The derivative of the Fermi distribution $\partial f / \partial \mathcal{E}$ is only has significant weight in a region centered on the Fermi energy $\mathcal{E}_F$ with width $k_B T$. Thus, we can use the Sommerfeld expansion to see that

$$\begin{aligned}
\mathbf{L}^{11} &= \sigma(\mathcal{E}_F) = \sigma \\
\mathbf{L}^{21} &= T\mathbf{L}^{12} = -\frac{\pi^2}{3e}(k_B T)^2 \left. \frac{\partial \sigma}{\partial \mathcal{E}} \right|_{\mathcal{E}=\mathcal{E}_F} \\
\mathbf{L}^{22} &= \frac{\pi^2}{3}\frac{k_B^2 T}{e^2}\sigma
\end{aligned}$$

We can now use these relations to get the thermal conductivity in terms of the electrical

conductivity. First, we impose the condition that the no electric current is flowing, which implies that

$$\mathcal{E} = -(\mathbf{L}^{11})^{-1}\mathbf{L}^{12}(-\nabla T)$$

Plugging this into the equation for the heat current, we get that

$$\mathbf{j}^q = \kappa(-\nabla T) \text{ where } \kappa = \mathbf{L}^{22} - \mathbf{L}^{21}(\mathbf{L}^{11})^{-1}\mathbf{L}^{12}$$

Using the fact that $\partial\sigma/\partial\mathcal{E}$ taken at $\mathcal{E} = \mathcal{E}_F$ is of order $\sigma/\mathcal{E}_F$, we can see that the second term in the above expression is dominated by the first by a factor of $(\mathcal{E}_F/k_BT)^2$, and so to leading order only the first term matters. Thus, from the expression for $\mathbf{L}^{22}$, we can see that

$$\kappa = \frac{\pi^2}{3}\left(\frac{k_B}{e}\right)^2 T\sigma$$

which is the Wiedemann-Franz law, now cast as a relation between the tensors κ and σ, in the presence of a magnetic field.

This should make some intuitive sense. After all, if the electrons can transmit heat, they should still do so when their orbits have been modified by the presence of a magnetic field. It is worth reiterating some of the assumptions present in this analysis. First of all, we have assumed that we are working with a metal, where thermal conductivity will be dominated by the electrons. We should not necessarily expect this behavior to hold for a semiconductor, for example. One might still expect that even if the Wiedemann-Franz law does not hold in general for a non-metal, the thermal Hall conductivity should not be affected by the phonon contribution to the thermal conductivity, as phonons don't carry spin and so should not couple to a magnetic field. However, there have been a few observations lately of the thermal Hall effect of phonons, which has been explained in terms of different materials as an effect of the Berry curvature of the phonon bands [11] or skew scattering of phonons off of magnetic impurities [12]. Even if we restrict to non-magnetic

metals there are examples of deviations from the Wiedemann-Franz behavior. Potassium, an alkali metal which should in principle have simple metallic behavior has been observed to have a thermal Hall conductivity which deviates from the Wiedemann-Franz law by up to 50% in magnetic fields up to 9T [13] [14] [15]. While the Wiedemann-Franz law captures relationship between the Hall effect and the thermal Hall effect to lowest order, it is important to view it more as a general empirical guide rather than an iron-clad law. Other effects can become important in specific materials, even metals.

Measurements of the thermal Hall effect in metals are often not reported as the thermal Hall angle θ_H, but instead as the thermal Hall coefficient R_{TH}, defined as

$$R_{\mathrm{TH}} = \frac{1}{B_z}\frac{dT_y/dy}{dT_x/dx} = \frac{1}{B_z}\frac{\kappa_{xy}}{\kappa_{xx}} = \frac{\tan\theta_H}{B_z}$$

This quantity has units of inverse Teslas, which suggests that it should be related somehow to mobility. Using the Wiedemann-Franz law derived above, we can show that it is exactly the Hall mobility:

$$R_{TH} = \frac{1}{B_z}\frac{\kappa_{xy}}{\kappa_{xx}} = \frac{1}{B_z}\frac{\sigma_{xy}}{\sigma_{xx}} = \sigma_{xx}R_H = \mu_H$$

where R_H is the standard Hall coefficient. (Parenthetically, it is this relation which generalizes to the thermal Hall effect in semiconductors:

$$R_{TH} \approx \frac{\kappa_{\mathrm{el}}}{\kappa_{\mathrm{tot}}}\mu_H$$

where κ_{el} and κ_{tot} are the electron/hole and total thermal conductivities, respectively [16].) While the caveats involving the applicability of the Wiedemann-Franz law above still apply, we should expect that materials which with high mobilities should also have large thermal Hall coefficients.

1.3 The Thermal Hall Conductivity in Bismuth

This brings us finally to the specific case of Bismuth. Figure 1.4 shows its crystal structure. Bismuth is a semi-metal, by which we mean a material which has both negatively charged (electrons) and positively charged (holes) carriers. Figure 1.5 show how these Fermi pockets are arranged in k-space, with one large hole pockets and three smaller electron pockets. It should be noted that the above analysis of the Wiedemann-Franz law did not make any assumptions about the charge of the carriers involved, and so it can be applied to the case of bismuth. Bismuth is characteristic of semi-metals in that it has a low carrier density ($4.1 \times 10^{17}/\text{cm}^3$ for electrons, $3.4 \times 10^{17}/\text{cm}^3$ for holes [17]) and a high mobility (4300 cm^2/Vs for electrons, 1500 cm^2/Vs for holes, measured in a thin film [18], and as high as 85,600,000 cm^2/Vs for electrons and 37,000,000 cm^2/Vs for holes in pure crystals [19]). We should thus expect that bismuth should display a large thermal Hall coefficient.

It is worth thinking about how the presence of two carriers will affect the Hall coefficient, as it will have direct consequences for the thermal Hall coefficient. In a simple model, we can imagine that the two carriers act as two separate conductive channels in parallel with each other. The channels each have resistivity tensors of the form

$$\rho_{\mathbf{e}} = \begin{pmatrix} \rho_e & -R_e H \\ R_e H & \rho_e \end{pmatrix} \quad \rho_{\mathbf{h}} = \begin{pmatrix} \rho_h & -R_h H \\ R_h H & \rho_h \end{pmatrix}$$

where ρ is the longitudinal resistivity of the channel, R is its Hall coefficient, and H is the applied magnetic field. Note that since the electrons and holes have differing sign, so do R_e and R_h. Since these channels are in parallel with each other, the total resistivity is given by

$$\rho = \left({\rho_{\mathbf{e}}}^{-1} + {\rho_{\mathbf{h}}}^{-1}\right)^{-1}$$

Figure 1.4: Crystal structure of bismuth. One unit cell is displayed along the c axis, and two along the a and b axes. The c axis is denoted the trigonal axis, and the a axis is denoted as the bisectrix. The direction perpendicular to both of these is called the binary axis (this is not the b axis, which forms a 120° angle with the a axis). Image generated with Jmol [20].

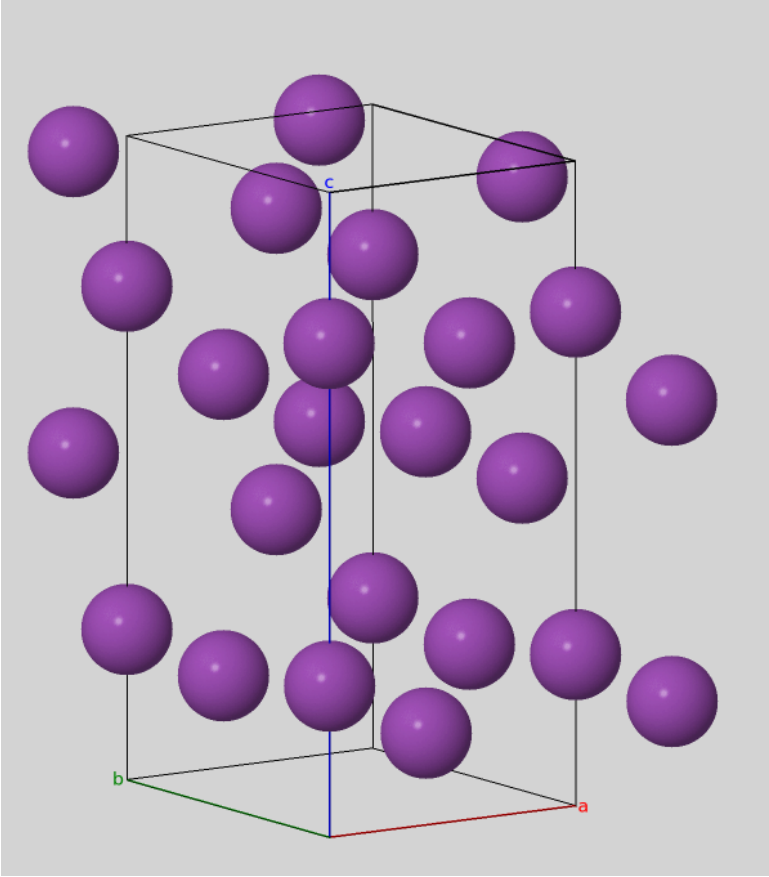

Figure 1.5: Fermi pockets in bismuth. The hole pocket is an ellipsoid with the long axis aligned with the trigonal axis. The three electron pockets are three ellipsoids, one with its long axis aligned with the bisectrix axis, and the other two distributed 120° either way around the trigonal axis. The electron pockets are canted by 6° degrees out of the bisectrix-binary plane. Image taken from [21].

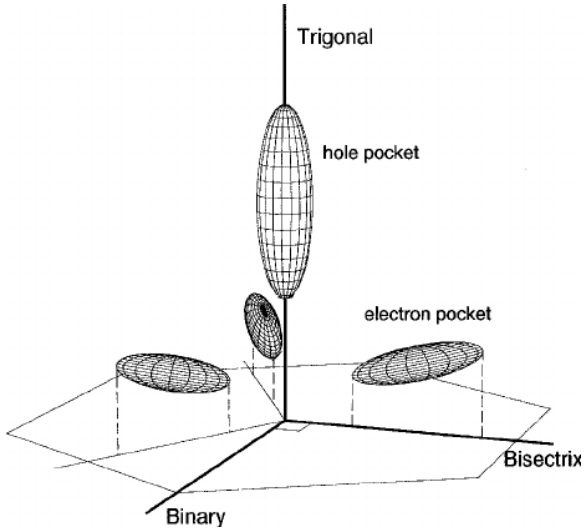

This results in a total resistivity tensor given by

$$\rho = \begin{pmatrix} \rho & -RH \\ RH & \rho \end{pmatrix}$$

where

$$\rho = \frac{\rho_e \rho_h (\rho_e + \rho_h) + (\rho_e R_h^2 + \rho_h R_e^2) H^2}{(\rho_e + \rho_h)^2 + (R_e + R_h)^2 H^2}$$

$$R = \frac{R_e \rho_h^2 + R_h \rho_e^2 + R_e R_h (R_e + R_h) H^2}{(\rho_e + \rho_h)^2 + (R_e + R_h)^2 H^2}$$

Both the longitudinal resistivity and Hall coefficient depend explicitly on the applied field H, unless $R_e = -R_h$. Since the Hall coefficient is inversely proportional to the carrier density, and bismuth has different densities for electrons and holes (see above), we can see that this is not the case for bismuth. In practice, this means the resistivity and Hall

Figure 1.6: Hall conductivity in bismuth, measured at 10K in our Janis cryostat. Notice the two linear regimes, one at low field and one at high field, consistent with the two carrier model.

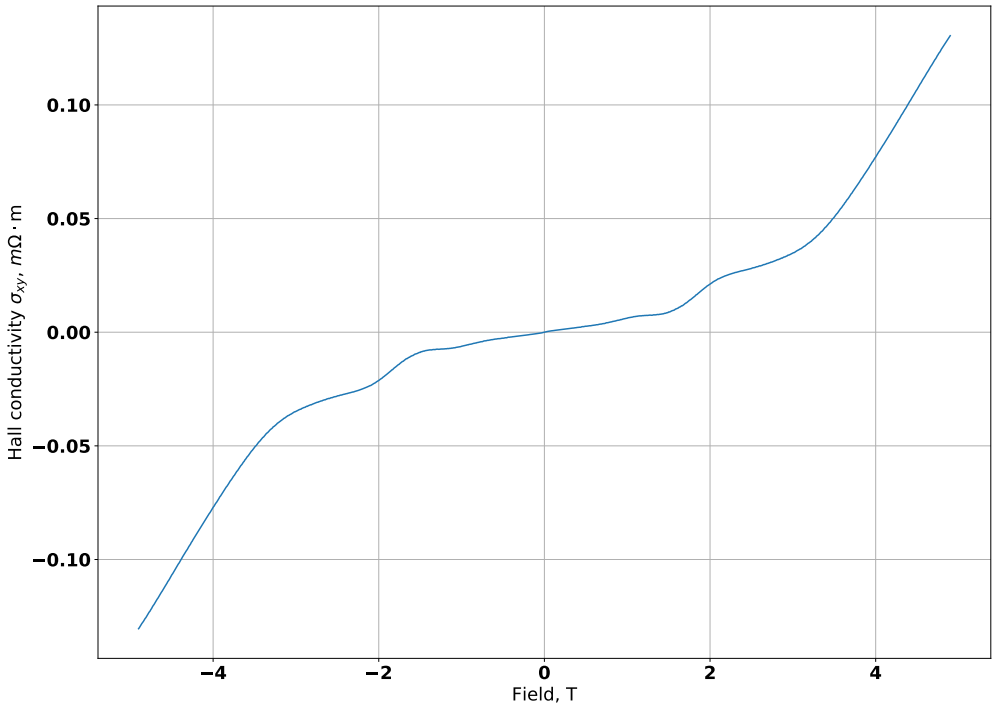

coefficient basically have two regimes, a low field regime where

$$\rho = \frac{\rho_e \rho_h}{(\rho_e + \rho_h)} \quad R = \frac{R_e \rho_h^2 + R_h \rho_e^2}{(\rho_e + \rho_h)^2}$$

and a high field regime where

$$\rho = \frac{\rho_e R_h^2 + \rho_h R_e^2}{(R_e + R_h)^2} \quad R = \frac{R_e R_h}{R_e + R_h}$$

Figure 1.6 is a plot of experimental data which shows this behavior: two linear regimes, one at high field, and one at low field.

What does this imply for the thermal Hall conductivity? Well, from the Wiedemann-

Franz law, we can see that the thermal Hall coefficient is given by

$$R_{\mathrm{TH}} = \sigma R_{\mathrm{H}} = \frac{R}{\rho}$$

as shown above. Rearranging terms and applying the Wiedemann-Franz law again, we get:

$$R_{\mathrm{TH}} = \frac{1}{H}\frac{\kappa_{xy}}{\kappa_{xx}} = \frac{1}{H}\frac{\kappa_{xy}}{LT\sigma}$$

$$\Rightarrow \kappa_{xy} = \frac{R}{\rho^2} HLT$$

where L is the Wiedemann-Franz constant and T is the temperature. Thus κ_{xy} will be a function of the applied magnetic field H just as R and ρ are. If we take the low and high field regimes, however, κ_{xy} should be more or less linear with field. Taking the low field expression for R and ρ gives us

$$\kappa_{xy,\mathrm{LOW}} = \frac{R_e\rho_h^2 + R_h\rho_e^2}{\rho_e^2\rho_h^2} HLT$$

So for small fields, κ_{xy} should be linear in the applied field. In the high-field limit, the expression becomes

$$\kappa_{xy,\mathrm{HIGH}} = \frac{R_e R_h (R_e + R_h)^3}{(\rho_e R_h^2 + \rho_h R_e^2)^2} HLT$$

At first glance, this looks qualitatively similar to the low field expression, linearly proportional to the applied field. However, remember that R_e and R_h have different signs, but are of the same order of magnitude. This implies that their sum should be small. In this expression, we take that small sum and cube it, making it even smaller. In the denominator, we take a linear combination of the squares of R_e and R_h (which are both positive now) and square them again. This indicates, at least qualitatively, that the high field coefficient should be much smaller than the low field coefficient.

How well do these predictions bear out in practice? Surprisingly, measurements of the

Figure 1.7: Thermal Hall conductivity in Bismuth, measured up to 3 T measured by [3]. Note that in all the traces down to 75K, the low field dependence is linear, and in the lower temperature curves we can see the high field thermal Hall conductivity go to zero.

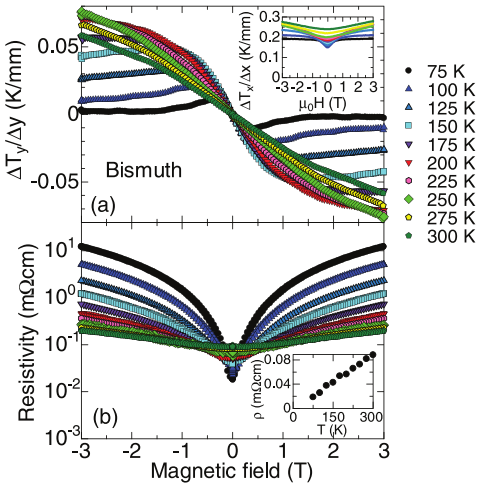

Figure 1.8: Temperature dependence of the thermal Hall coefficient in bismuth up to 3 T and 300K, taken from [3]. The dependence is not strictly linear with temperature, and follows more or less the temperature dependence of the Hall mobility μ_H.

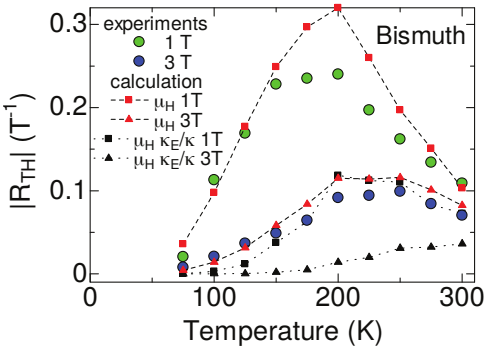

thermal Hall effect in bismuth have only been carried out in high magnetic fields relatively recently, by Kobayashi et al. in 2012 [3]. In that work, measurements of the thermal Hall coefficient were performed in fields up to 3T and temperatures from room temperature down to 75K. Figure 1.7 reproduces their results in measuring the transverse temperature gradient. We can see that for all the traces, the low field dependence is linear, with the slope decreasing at higher field. In some of the lower temperature traces, we can also see the thermal Hall conductivity tend towards zero at higher field. This would seem to reproduce the qualitative features discussed above. Additionally, figure 1.8 from the same paper shows the temperature dependence of the thermal Hall coefficient R_{TH}. Although I did not remark on it above, the basic analysis would indicate that the thermal Hall coefficient should increase linearly with temperature. The experimental data shows this is clearly not the case. Instead, the data shows that the thermal Hall coefficient generally follows the temperature dependence of the Hall mobility μ_H. This is not surprising, as they should be directly related.

One possible objection to the prediction that the thermal Hall coefficient should be effectively zero at high field might be that since it is not exactly zero, with a sufficiently large field one should be able to see a non-zero thermal Hall conductivity once again. This presupposes that the simple two-carrier model described above is applicable for arbitrarily large applied fields. The validity of this assumption is contradicted by the physics of Landau quantization in metals, i.e. the quantization of the circular path of a charged particle in a magnetic field. This effect is responsible for the oscillations seen in many observables (such as resistivity and magnetic susceptibility) in strong magnetic fields [22]. As the field gets stronger, the Landau levels get farther apart in energy and more degenerate, until all the carriers are collected in the lowest level. This is known as the quantum limit. This has the effect of gapping out the carriers, and so we would expect that they would no longer participate in the thermal Hall effect. The field at which this happens is proportional to the cross-sectional area of the Fermi surface perpendicular to the applied field [22], and since bismuth has small Fermi pockets we should expect this to happen at relatively low fields. The field at which this happens depends strongly on the angle due to the elongated Fermi pockets, but is less than 8T for all angles [23]. This will ultimately suppress the thermal Hall coefficient at these fields. Making measurements of the thermal Hall effect at these fields presents some experimental challenges, however. Before we can discuss those difficulties, we must discuss the experimental setup for making any thermal Hall effect measurement.

1.4 Performing Thermal Hall Effect Measurements

Now that we have discussed the origin of the thermal Hall effect in metals, we must now discuss how one makes the measurement. Figure 1.9 shows a schematic of the measurement. The sample is attached to a cold finger, typically by way of a thermally conductive sample holder (made of oxygen-free copper, in our case). This controls the overall tem-

Figure 1.9: Schematic of a thermal Hall effect measurement. The magnetic field is applied out of the plane of the page. Both the longitudinal (ΔT_x) and transverse (ΔT_y) temperature gradients are measured. If necessary, the measurement can be carried out with two thermometers, and the gradients disentangled by (anti-)symmetrizing the measured gradient with respect to the applied field.

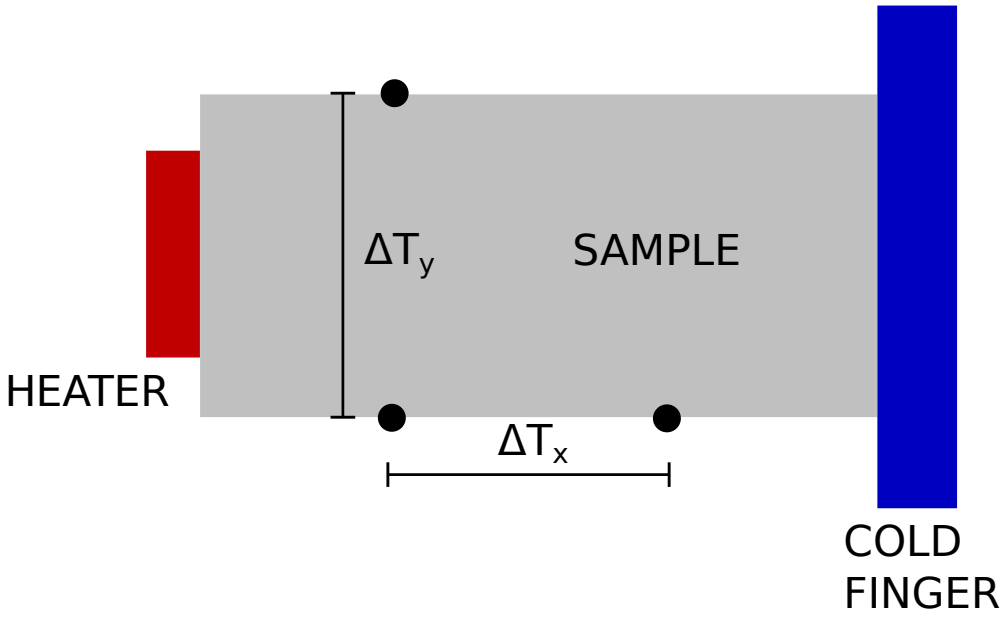

perature of the sample. On the other end of the sample, a small resistive heater is attached using thermally conductive paste. This setup mirrors the boundary conditions of the finite element calculations presented above: one side (the cold finger) is held at a fixed temperature, the opposite (the heater) has a prescribed amount of heat energy applied, and the two perpendicular boundaries are (ideally) assumed to be insulating. Experimentally, this means performing the measurement in vacuum.

In order to measure the thermal Hall conductivity, we should ideally place three thermometers on the edge of the sample. This allows us to measure two temperature gradients: the longitudinal (along the direction pointing from the heater to the cold finger, denoted

ΔT_x) and the transverse (perpendicular to the longitudinal gradient, denoted ΔT_y). If the thermometers are small enough relative to the sample, they can be mounted directly to the sample with a thermally conductive paste, similar to the heater. Alternatively, the thermometers can be mounted separately and thermally linked to the sample with gold wire. We can use this information along with the applied power P to determine the terms of the thermal conductivity tensor by writing Fourier's law as

$$\begin{pmatrix} j_x \\ j_y \end{pmatrix} = \begin{pmatrix} -P/(t \cdot w) \\ 0 \end{pmatrix} = \begin{pmatrix} \kappa_{xx} & \kappa_{xy} \\ -\kappa_{xy} & \kappa_{yy} \end{pmatrix} \begin{pmatrix} -\Delta T_x/l \\ -\Delta T_y/w \end{pmatrix}$$

where l is the length between the two longitudinal thermometers, t is the thickness of the sample, and w is the width of the sample (i.e. $t \cdot w$ is the cross sectional area of the sample perpendicular to its length). The assumption that $\kappa_{yx} = -\kappa_{xy}$ is taken from a relation due to Onsager (note that these are not the Onsager reciprocal relations of statistical mechanics, for details on where this relation comes from see problem 6f of chapter 13 of Ashcroft and Mermin [10]). If we further assume that the heat conduction is isotropic, that is $\kappa_{xx} = \kappa_{yy}$, we are left with two equations in two unknowns, κ_{xx} and κ_{xy}:

$$\begin{aligned} P/(t \cdot w) &= \kappa_{xx}\Delta T_x/l + \kappa_{xy}\Delta T_y/w \\ 0 &= \kappa_{xy}\Delta T_x/l - \kappa_{xx}\Delta T_y/w \end{aligned}$$

The second line gives the relation

$$\kappa_{xy}\Delta T_x w = \kappa_{xy}\Delta T_y l \Rightarrow \kappa_{xy} = \kappa_{xx}\frac{\Delta T_y l}{\Delta T_x w}$$

substituting this result into the first equation gives

$$P \cdot l = \kappa_{xx}\left(\Delta T_x w t - \frac{\Delta T_y^2 l^2 t}{\Delta T_x w}\right) \approx \kappa_{xx}\Delta T_x w t$$

For the last step, we are making use of the fact that the thermal Hall angle is generally small, so ΔT_x is much larger than ΔT_y. Now we can use these relations to get the terms of the conductivity tensor in terms of known variables:

$$\kappa_{xx} = \frac{Pl}{\Delta T_x w t} \quad \kappa_{xy} = \frac{P \Delta T_y l^2}{\Delta T_x^2 w^2 t}$$

These are the relations use to determine the thermal Hall conductivities in the experiments described in the coming chapters.

As stated above, ideally one would use at least three thermometers to measure the transverse and longitudinal thermal gradients. However, each thermometer allows a small amount of heat to escape the sample, which contradicts the ideal case where the boundary is perfectly insulating. We can minimize the amount of heat lost this way by only using two thermometers, with an offset in both the x and y directions. This poses the problem of how the ΔT_x and ΔT_y can be disambiguated. In the case of a thermal Hall effect measurement taken at a constant temperature in a sweeping magnetic field, the Onsager transport relation mentioned above implies that the κ_{xx} and κ_{xy} have different symmetry with respect to the field:

$$\kappa_{xx}(H) = \kappa_{xx}(-H) \quad \kappa_{xy}(H) = -\kappa_{xy}(-H)$$

By inspection we can see that this implies that $\Delta T_x(H)$ is even in H, and $\Delta T_y(H)$ is odd. Thus, the two temperature gradients can be disambiguated by taking the measurement by performing the measurement in both positive and negative field, and extracting the proper gradients by (anti-)symmetrizing the gradient measured between the two thermometers.

Based on the previous discussion, one might think that the best way to conduct a thermal conductivity measurement would be to simply run the heater with a constant power and measure the thermal gradients as a function of the relevant experimental variable (e.g. magnetic field for a thermal Hall effect measurement). However, if the overall temperature of the sample were to drift, or if there is any temperature gradient in the sample when there

Figure 1.10: Raw temperature gradient data, in this case a longitudinal temperature gradient measured using a pair of thermocouples on a bismuth sample. The raw data is in blue, and the extracted envelopes are in red and green.

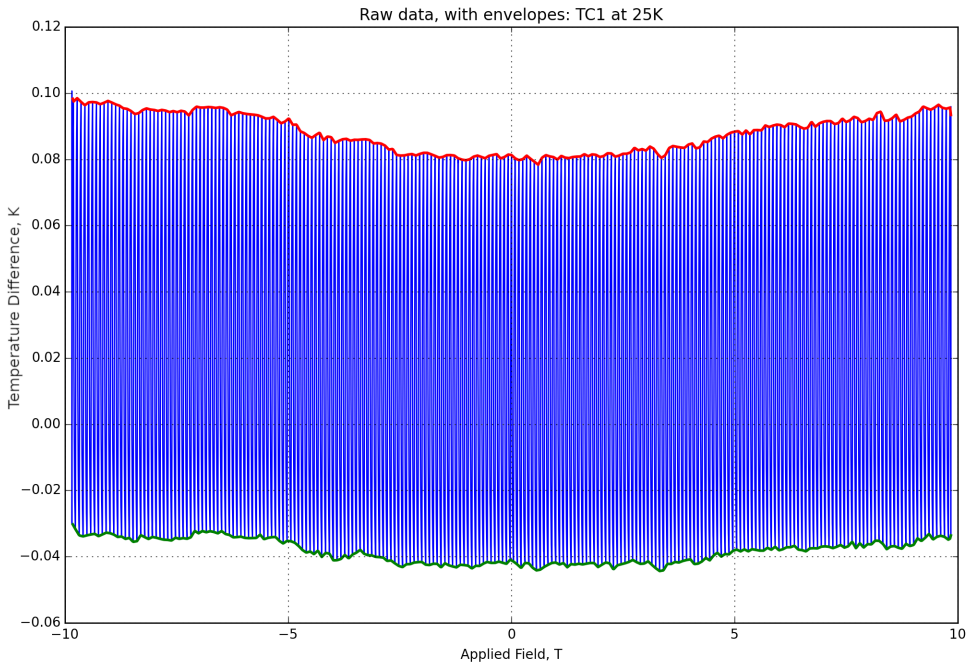

is no heat applied, this will appear as a spurious signal in the thermal conductivities. This can be corrected by pulsing the heater on and off over the course of the measurement rather than keeping it constant. In many cases, a square wave is used: the heater is turned on for some time, and then turned off for some time. The period must be long enough that the sample reaches equilibrium during each on-cycle and off-cycle. This allows the overall background drift to be subtracted away from the measurement. This method is certainly viable, but my preference is to use a sine wave excitation on the heater instead. This has the advantage of never bringing the sample out of equilibrium as long as a low enough frequency is chosen. If we denote the current through the heater as $i(t) = i_0 \sin \omega t$, the power coming out of the heater will be

$$P(t) = I^2 R = i_0^2 R \sin^2 \omega t = i_0^2 R \frac{1 - cos(2\omega t)}{2}$$

i.e. it will have twice the frequency of the excitation current. The temperature of each thermometer, or alternatively the difference in temperature between any pair of thermometers, will have the general form

$$T_n(t) = A(t) \sin^2 \omega t + D(t)$$

where $A(t)$ is the difference between the temperature with the heater on and with the heater off, and $D(t)$ is the overall drift. There are two conditions to ensure that ω is sufficiently small: A should not change with ω, and $P(t)$ should have the same phase as $T_n(t)$. The problem of finding the temperature gradients thus rests on extracting $A(t)$. This amounts to the problem of demodulating an AM signal.

One simple method for accomplishing this is by simply using a peak detection function. Figure 1.10 shows some raw temperature gradient data from the experiments on bismuth which will be described later in this work. The blue curve shows the raw data, still mixed with the "carrier". One attractive feature of the sine wave excitation is it produces well

defined peaks suited for automatic peak detection. Taking the maxima and minima, we can interpolate between them to get the upper and lower envelopes $E_{\text{upper}}(t)$ and E_{lower}. The amplitude and drift can be expressed straightforwardly as

$$A(t) = E_{\text{upper}}(t) - E_{\text{lower}}(t) \quad D(t) = \frac{E_{\text{upper}}(t) - E_{\text{lower}}(t)}{2}$$

This method is simple to implement, and has the advantage that we do not need any phase information from the heater excitation to determine the gradients. It does however require that we are able to unambiguously detect the peaks.

There is another method which exploits the similarity of this problem to that of demodulating an AM radio signal, known as a "product detector". First, we expand the raw signal using the double angle identity:

$$T_n(t) = A(t)\sin^2 \omega t + D(t) = A(t)\frac{1 - \cos 2\omega t}{2} + D(t)$$

As long as $A(t)$ and $D(t)$ are varying slowly compared to the "carrier frequency" 2ω, we can use a high pass filter to isolate the $\cos 2\omega t$ term, leaving us with

$$T_n(t) = \frac{A(t)}{2}\cos 2\omega t$$

Next, we multiply this by $\cos 2\omega t$. This requires us to have proper phase information about the excitation current. Doing this gives

$$\frac{A(t)}{2}\cos 2\omega t \cos 2\omega t = \frac{A(t)}{2}\left(\frac{1}{2} + \frac{1}{2}\cos 4\omega t\right)$$

Now, once we low pass filter this signal, we end up with $A(t)/4$. There are variations of this method which involve multiplying by a higher order power of the "carrier" which result in a higher frequency signal which needs to be filtered away. This method does need

us to preserve phase information about the excitation current, but does not require any peak detection.

There is one significant experimental detail which has been elided over in this analysis: what kind of thermometers can be used, and what advantages and disadvantages these have. This is not a trivial detail: to make thermal Hall effect measurements, we require thermometers which are both sensitive to millikelvin temperature gradients while not being affected by a magnetic field. We have found that commercially available thermometers have not been able to keep up with our requirements in this respect. In the next chapter, I will describe the research project I undertook to develop thermometers which better satisfied these requirements, as well as the thermal Hall effect measurements on bismuth I made to benchmark these new thermometers.

CHAPTER 2

Strontium Titanate Microthermometers

2.1 Thermometry

Temperature, in its most general form, is a consequence of the "zeroth" law of thermodynamics: If two bodies A and B are in thermodynamic equilibrium, and B is in thermodynamic equilibrium with a third body C, then A and C are in thermodynamic equilibrium with each other as well. Thus, the quality of being in thermodynamic equilibrium is an equivalence relation, and we can define a temperature scale by assigning a numerical value to each of its equivalence classes. If we take care to assign this quantity such that one with a higher temperature will transfer heat to one with a lower temperature when they are brought in contact (a corollary of the second law of thermodynamics) as well as presupposing the existence of an absolute lowest temperature (the third law), we will arrive at an experimentally useful temperature scale. Within the formalism of statistical mechanics, we can construct such a temperature scale within the microcanonical ensemble as function of the total energy E and information about the states of the system:

$$\frac{1}{T} = \frac{dS}{dE} = \frac{d}{dE} k \log W$$

where $W(E)dE$ is the number of states with energy between E and $E + dE$ and k is Boltzmann's constant. This function, however, can only be computed explicitly for the simplest physical systems. In practice, if we want to study the flow of heat through a

system by measuring temperature, we must find some other observable we can measure as a proxy.

In principle, we might want to find some system whose thermodynamic equation of state depends on temperature and other quantities which are all independent of temperature. Such a system is referred to as a primary thermometer. For a simple example of such a thermometer, consider the equation of state of an ideal gas:

$$PV = NkT$$

If we take a sample of an ideal gas with a known number of molecules N in a known volume V, we can determine the temperature T by measuring its pressure P. Other examples of primary thermometers include measurements of the speed of sound in a gas, measurements of the Johnson-Nyquist noise in an electrical circuit, or measurements of blackbody radiation [24]. These methods of measuring temperature are very useful for accurately setting a temperature scale, but they have some serious drawbacks as thermometers for use in other experiments. Most of them require sensitive measurements of multiple physical observables, as well as bulky and complicated experimental apparatus. If one wanted to determine the thermal conductivity of a small crystal by measuring a temperature gradient across its length, it would not be feasible to connect the crystal to two independent samples of an ideal gas and measure their pressures. Thus, the temperature standard set by these methods must be transferred to a more convenient thermometer.

Such a device is known as a secondary thermometer. In this case, we measure some observable as a function of temperature, which we determine from some known standard. This can be a primary thermometer or another secondary thermometer which has already been calibrated to sufficient accuracy. In experimental condensed matter physics, by far the most common types of secondary thermometers used are resistance thermometers and thermocouples. Resistance thermometers simply measure the resistance of some mate-

rial as a proxy for temperature, either a metal such as platinum (resistance increasing with higher temperature, or "positive temperature coefficient") or a semiconductor, such as zirconium–oxynitride (known by its trademarked name Cernox) or ruthenium oxide (resistance decreasing with higher temperature, or "negative temperature coefficient"). Such thermometers are convenient since they can be made compact, they are commercially available, and there are well–established protocols and instrumentation for measuring resistance. There are a wide variety of resistance thermometers that suit different temperature ranges and experimental conditions. Thermocouples, which measure the temperature dependant thermopower between two metals with differing carrier concentrations, can be even more compact and are especially useful for making differential measurements. However, they require measurements of DC voltages in the microvolt range, and their sensitivity is reduced at low temperature. In any case, both of these methods allow us to measure temperature without considering the microscopic details of the system, only how accurately it has been calibrated.

There are some experimental details which must be considered when using a resistance thermometer. Many important experimental techniques in condensed matter physics involve applying an intense magnetic field (up to 45T for the current state-of-the-art DC magnets) to a sample of interest. Resistance thermometers generally exhibit magnetoresistance, the changing of their resistivity in a magnetic field. The most commonly used resistance thermometers are selected to have as small a magnetoresistance as possible, but even Cernox thermometers display a change of resistance of a few percent in magnetic fields up to 14T. If one is not measuring any direct thermal property of a sample and can safely assume that the sample is well thermalized with the cold finger, one can simply mount a thermometer outside the region of intense magnetic field. However, if you are measuring some thermal property of a material (such as heat capacity or thermal conductivity), there is no getting around calibrating the thermometer as a function of temperature and magnetic field (see figure 2.1). For resistive thermometers such as Cernox or ruthe-

nium oxide, the magnetoresistance can vary quite a bit from thermometer to thermometer, as they can have slightly different doping levels. Additionally, Cernox thermometers can have orientation dependent resistance changes on the order of 0.05% to 0.7% depending on the field at 4.2K [25]. For many experiments this is more than sufficient, but the thermal Hall measurements discussed in this thesis require precision to the level of millikelvin. Thus, when using such thermometers for thermal Hall measurements, the best practice is to calibrate them in situ. Even still, it has been reported that spurious temperature gradients antisymmetric with the magnetic field (and thus easily conflated with a thermal Hall signal) can occur even with pairs of Cernox thermometers cut from the same wafer at temperatures below 1K, for reasons which are not completely understood [26]. Thus, it is imperative to be extremely careful when making sensitive thermal measurements with resistive thermometers in this regime.

Regardless, there is a great deal of scientific value in thermal measurements performed in strong magnetic fields. Heat capacity provides a generic method for identifying phase transitions, and thermal transport is sensitive to excitations in a solid which do not carry charge and thus can't be studied with electrical transport methods. Thus, it is our goal to develop new methods for accurately and precisely measuring temperature in the presence of intense magnetic fields. The scientific potential of these methods and the experimental techniques they make possible will be underscored in the next section. For more information about thermometry and its application in experimental condensed matter physics, chapter 5 of [24] is an invaluable reference.

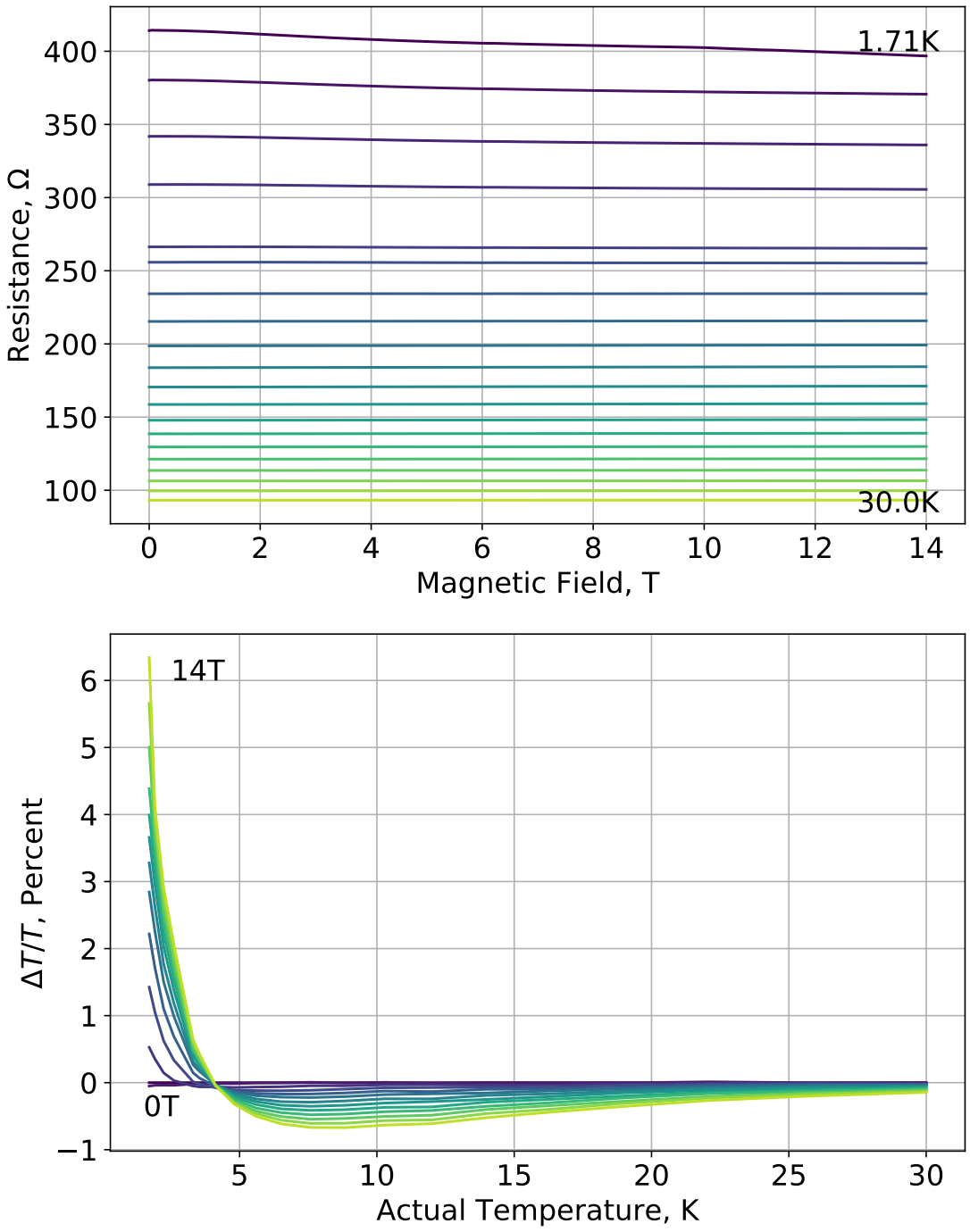

Figure 2.1: Example Cernox Field Calibration. Top: Magnetoresistance of a Cernox thermometer. Bottom: Field calibration curves for the same thermometer. $(T_{\text{apparent}} - T_{\text{actual}})/T_{\text{actual}}$ is plotted versus the actual temperature.

2.2 Quantum Criticality in Strontium Titanate

With the goal of identifying a system with some observable quantity which is sensitive to temperature but not magnetic field in mind, we turn to the theory of quantum critical ferroelectricity in strontium titanate ($SrTiO_3$). Strontium titanate is well known as a paraelectric, a material where an applied electric field $\mathbf{E}$ generates a polarization density, or electric dipole moment per unit volume $\mathbf{P}$:

$$\mathbf{P} = \epsilon_0 \chi_e \mathbf{E}$$

where ϵ_0 is the permittivity of free space and χ_e is the electric susceptibility. Note that the electric susceptibility is a unitless quantity, the fundamental constant ϵ_0 converts the units between $\mathbf{E}$ and $\mathbf{P}$. Strontium titanate (abbreviated STO) has been known to have a large electric susceptibility of 330 at room temperature that rapidly increases as the temperature is lowered [27]. This indicates that it might be useful for making a capacitive thermometer, as for a parallel plate capacitor, the capacitance is given by

$$C = \frac{\epsilon A}{d} = \frac{\epsilon_0 (1 + \chi_e) A}{d}$$

where A is the area of the plates, d is the distance between them, and $\epsilon = \epsilon_0(1 + \chi_e)$ is the permittivity of the medium between the plates. However, it is worth discussing what the origin of this large electric susceptibility in STO. The electric susceptibility is intimately connected with the optical phonons of a crystal, since it is these phonons which describe displacements of the ions in the unit cell relative to each other and can thus produce a net electric dipole in an ionic crystal [10]. It is not immediately obvious why these should depend so strongly on temperature, however.

One significant hint comes from the fact that some crystals with the same perovskite structure as strontium titanate, such as barium titanate and lead titanate, are ferroelectrics,

i.e. materials which maintain a spontaneous polarization density without the application of an electric field [28]. This is analogous to the spontaneous magnetic dipole moment present in ferromagnets such as iron. These materials are so called displacive ferroelectrics, where the net dipole moment is the result of a displacement in the lattice. This corresponds to having an optical phonon with zero frequency. Above the Curie temperature T_c, these materials are paraelectrics similar to strontium titanate, with dielectric susceptibilities that are proportional to $(T - T_c)^{-1}$. In qualitative terms, this results from a temperature dependent gap opening up in the optical phonon spectrum, from an optical phonon with zero frequency below T_c to a "soft" optical phonon above T_c [29]. This would result in a material which has a strongly varying dielectric susceptibility with temperature, but in any event strontium titanate does not have a spontaneous electric dipole moment. Additionally, as will be seen in measurements described below, the temperature dependence of strontium titanate does not go as $\chi_e \sim 1/T$, but $\chi_e \sim 1/T^2$! This kind of rapid increase of a susceptibility is generally indicative of a phase transition, but none is observed in strontium titanate.

Instead of a normal phase transition, the rapidly increasing electric susceptibility is due to a quantum phase transition. Sometimes referred to as a "phase transition at zero temperature", a quantum phase transition occurs when the ground state of a system's Hamiltonian has a sharp kink or discontinuity at a function of some parameter [31], for example g. This can occur, for example, if there are two states of a given Hamiltonian, $|\psi_1\rangle$ and $|\psi_2\rangle$, one of which is ground state when g is larger than some critical value g_c, the other of which is the ground state is smaller than g_c. Although the energy of each of these states should be a smooth function of g, the ground state energy will have a kink where their energies cross at g_c. Although this discontinuity occurs at zero temperature, and so can't be reached directly, it can have a large effect on the physics of the system at finite temperature. This is due to the fact that in addition to the diverging correlation length ξ^x observed close to classical phase transitions, quantum phase transitions result in a diverging correlation time ξ_t as well. Quantum critical scaling will be observed when the temperature is sufficiently

Figure 2.2: Phase diagram of quantum critical ferroelectricity, reproduced from [30]. On the x axis, the tuning parameter is derived from the Debye wavevector Λ and parameters from the electric polarization equation of state a and c. On the y axis, the temperature is normalized by the Debye temperature θ. Note the position of Strontium Titanate outside the ferroelectric regime.

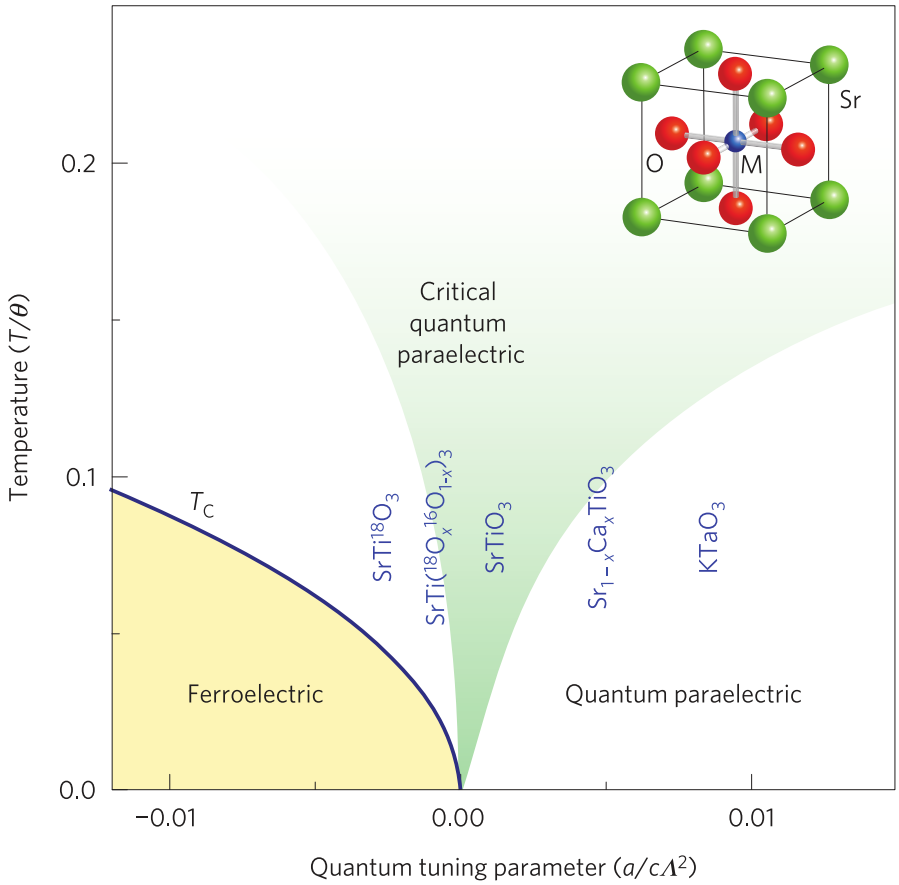

low, i.e. that $k_b T < \hbar \xi_t^{-1}$. In the case of strontium titanate, the quantum phase transition is between a ground state of the lattice with an optical phonon with zero frequency (and thus ferroelectricity) and one without. The critical fluctuations in time are responsible for the different scaling behavior of the susceptibility between the quantum and classical phase transition. Figure 2.2 shows the quantum critical phase diagram of the perovskite lattice, with strontium titanate labeled. The tuning parameter is listed as $a/c\Lambda^2$, where Λ is the Debye wavevector, and a and c are parameters for the electric polarization density equation of state [30]

$$\epsilon_0 E = aP + bP^3 - c\nabla^2 P$$

Assuming that b is positive and E is zero, this equation will only have one solution $P = 0$ when a is positive (i.e. no spontaneous polarization), and two more solutions $P = \pm P_0$ when a is negative (i.e. spontaneous polarization). Thus, when the tuning parameter is positive, we will have a paraelectric, and when it is negative, a ferroelectric state. The region where quantum critical effects are important is shaded green. We can see that strontium titanate is just above but very close to the quantum critical point. This explains its diverging electric susceptibility.

To explore the possibility of using this property of strontium titanate for making thermometers, some STO wafer was acquired and cut into a small piece, 3.86 mm long by 3.25 mm wide by 0.1 mm thick. Each side of this wafer was metallized with gold in our Denton evaporator. This sample was then placed in the variable temperature insert probe of our Janis wet cryostat. The capacitance was measured using our Andeen-Hagerling 2700A capacitance bridge while sweeping temperature at a constant rate from 50 K to 2 K. An excitation of 5 V was used to measure the capacitance. The dielectric susceptibility can be computed from the capacitance and the geometric information about the device using the standard parallel plate capacitor formula from above. The results of this experiment are shown in figure 2.3, plotted as $1/\epsilon \approx 1/\epsilon_0 \chi_e$ versus T^2. This makes the divergence of the susceptibility in the quantum critical regime clear as a linear trend. At the lowest tempera-

Figure 2.3: Top: Dielectric constant of Strontium Titanate as a function of temperature, plotted as $1/\epsilon$ vs T^2 to show the linear trend. Bottom: Low temperature plot of $1/\epsilon$, showing that ϵ reaches a maximum at $T = 3.29$K. This data was taken using the VTI probe in our Janis cryostat, but reproduces the results of [30].

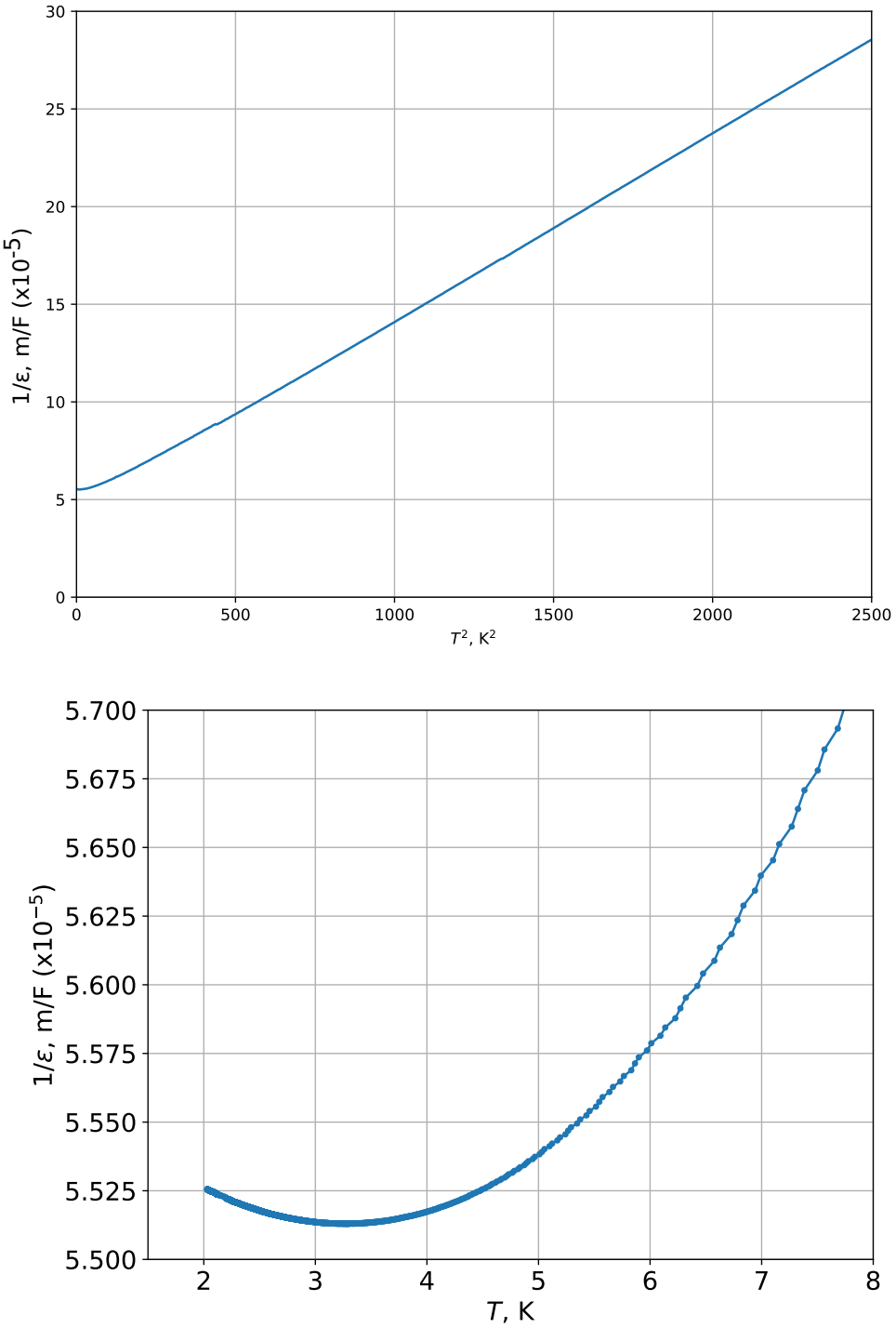

tures, however, this increase stops, reaching a maximum at 3.29 K. Here, strontium titanate is in the "quantum paraelectric" regime, where the gap in the optical phonon dispersion is relatively large but the temperature is small compared to the Debye temperature θ [29]. In this regime the electric susceptibility stops increasing, as the quantum critical point is no longer having a strong effect. Since the susceptibility is no longer changing much with temperature, a thermometer made with strontium titanate would not be sensitive in this regime. To illustrate this point, the effective sensitivity of the device is plotted in figure 2.4 as the quantity $\frac{1}{C}\frac{dC}{dT}$, where C is the capacitance of the device. This gives a measure of the sensitivity relative to the overall magnitude of the capacitance. The magnitude of the dimensionless sensitivity peaks at a value of 0.057 K^{-1} around 24 K, becoming zero at 3.29 K as discussed above. As a point of comparison, commercial Cernox thermometers have a dimensionless sensitivity ($\frac{1}{R}\frac{dR}{dT}$ in this case) around 1 K^{-1}, while ruthenium oxide thermometers have values around 0.3 K^{-1} [32], meaning that the capacitive thermometers are less sensitive by up to an order of magnitude and a half. However, the temperature controllers used to read these thermometers can measure resistance to one part in 100,000, whereas the capacitance bridge can measure capacitance to one part in 10,000,000. Thus, in real terms, they have comparable sensitivities.

As a point of comparison, figure 2.5 shows a similar experiment with a capacitor made with a different material, Potassium Tantalate ($KTaO_3$). Looking at the phase diagram in figure 2.2, we can see it is farther away from the quantum critical point, into the quantum paraelectric regime. For this experiment, a 2.26 mm wide by 3.48 mm long by 0.1 mm thick piece of material was metallized into a capacitor. The data is plotted with the same $1/\epsilon$ vs T^2 axes as the STO data. By comparing the scale to that in figure 2.3, we can see that the divergence of the dielectric susceptibility is not nearly as strong, and the dependence not nearly as linear. The quantum paraelectric regime is entered at a much higher temperature, and the susceptibility reaches its maximum at a temperature of 4.31 K. Thus, we can see that we must have a material in the quantum critical regime in order to make a

Figure 2.4: Sensitivity of the Strontium Titanate device under test, plotted as the "dimensionless" quantity $\frac{1}{C}\frac{dC}{dT}$.

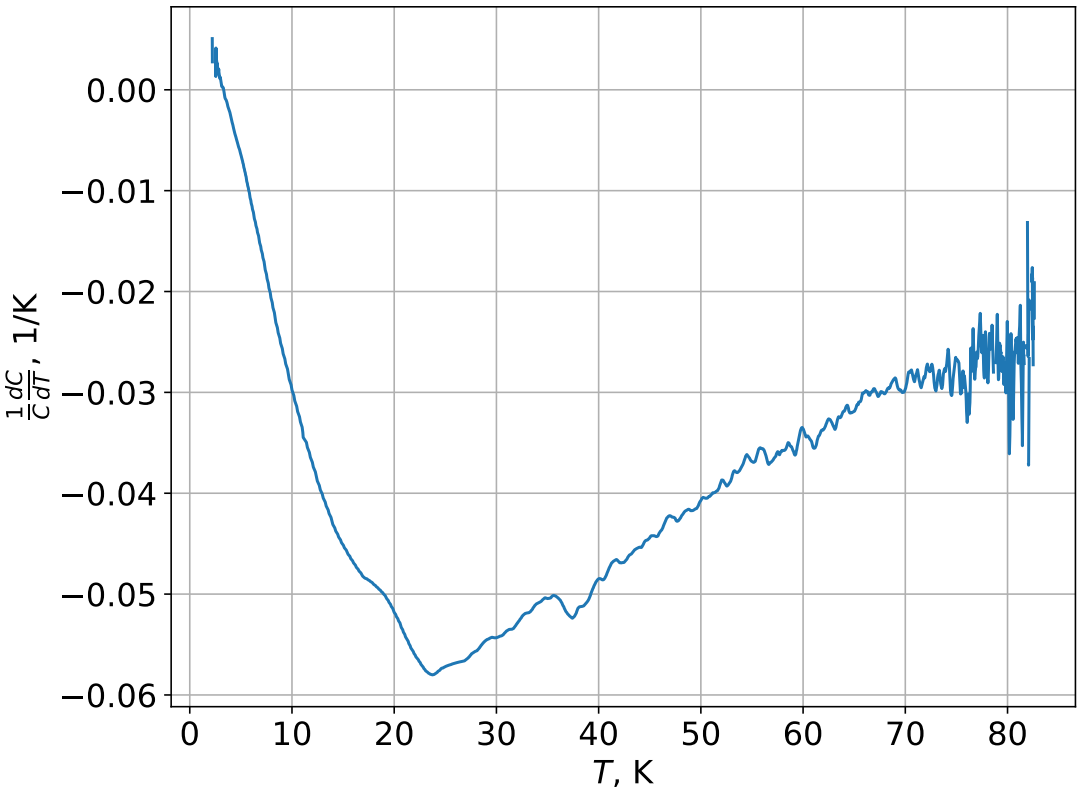

Figure 2.5: Top: Dielectric constant of Potassium Tantalate ($KTaO_3$), another paraelectric material considered as a candidate for making capacitive thermometers. The linear trend when plotted as $1/\epsilon$ vs T^2 is not as apparent as for $SrTiO_3$, and the overall change is not nearly as large. Bottom: Low temperature plot of $1/\epsilon$, as in figure 2.3. The dielectric susceptibility reaches a maximum at $T = 4.31$K, higher than that in $SrTiO_3$. As before, this data was taken using the VTI probe in our Janis cryostat, but reproduces the results of [30].

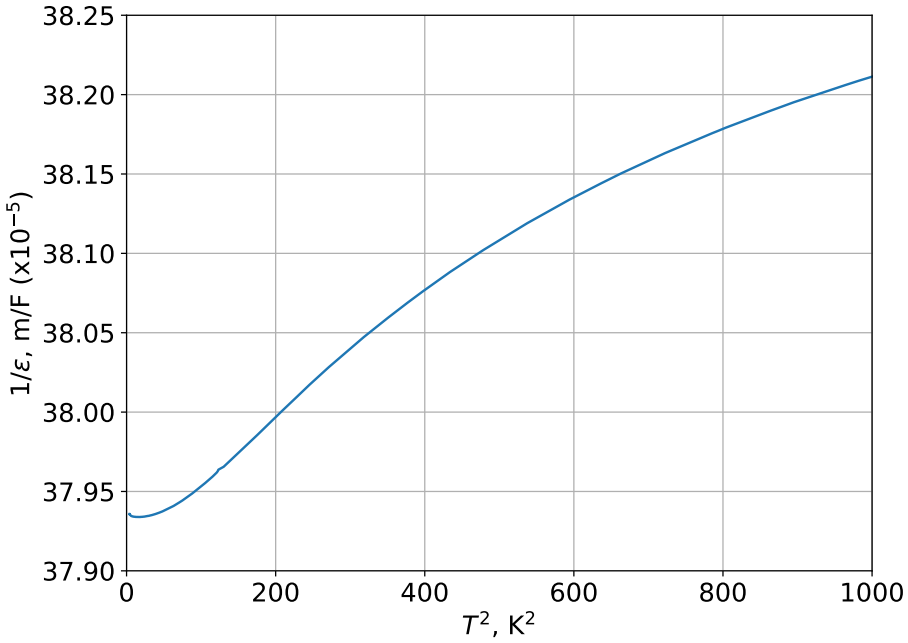

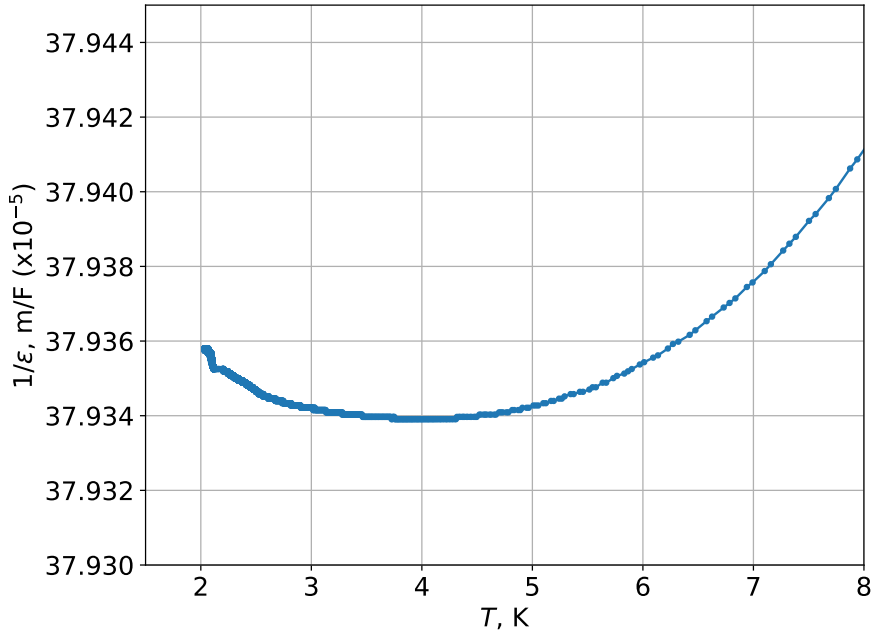

good thermometer. In the next chapter, the process of making thermometers out of these devices will be discussed.

2.3 Strontium Titanate Thermometers

In order to make a thermometer out of $SrTiO_3$, we take a small, thin (0.1 mm) sample of the material (purchased from the MTI corporation)[33] and evaporate gold contacts on to either face. These contacts form a parallel-plate capacitor, and by measuring the change in the capacitance we measure the dielectric constant and by proxy the temperature. Figure 2.6 shows a pair of assembled thermometers. The thermometers are approximately 0.5 mm long, 0.5 mm wide, and 0.3mm thick, and the electrical leads are a pair of 25 μm diameter phosphor bronze wires. Figure 2.7 shows an example calibration curve for a $SrTiO_3$ thermometer. Both the capacitance and sensitivity of the thermometer are shown from 4 K up to room temperature. The magnitude of the sensitivity increases (note the sign, increasing dielectric constant corresponds to decreasing temperature) up to about 25 K before decreasing and reaching a maximum value below 4 K. The particulars depend somewhat on the individual thermometer, notably, some do not reach a maximum value at all above 1.5 K, the lowest temperature at which we calibrated the thermometers used in this experiment. We believe this to be due to variance in our process for making the thermometers, in particular the amount of heat they are exposed to when the leads are attached and the resin surrounding the wafer is cured. Because of this, they must be calibrated *in situ* for each experiment. However, the general trend is the same, with the sensitivity being greatest around 20 to 40 K. Using our capacitance bridges (an Andeen-Hagerling 2700A digital bridge and a General Radio 1615-A analog bridge), we can reliably measure a change in capacitance of about 1×10^{-5} pF. This corresponds to change in temperature of 0.1 mK. Other measurements [8] using resistive thermometers quote a resolution of 0.2 - 0.4 mK. This is after extensive field calibration of the thermometers, a time-consuming

Figure 2.6: A pair of STO thermometers, used to make thermal measurements. The background is a piece of graph paper with 1mm divisions, the thermometers themselves are approximately 0.5 mm long, 0.5 mm wide, and 0.3 mm thick.

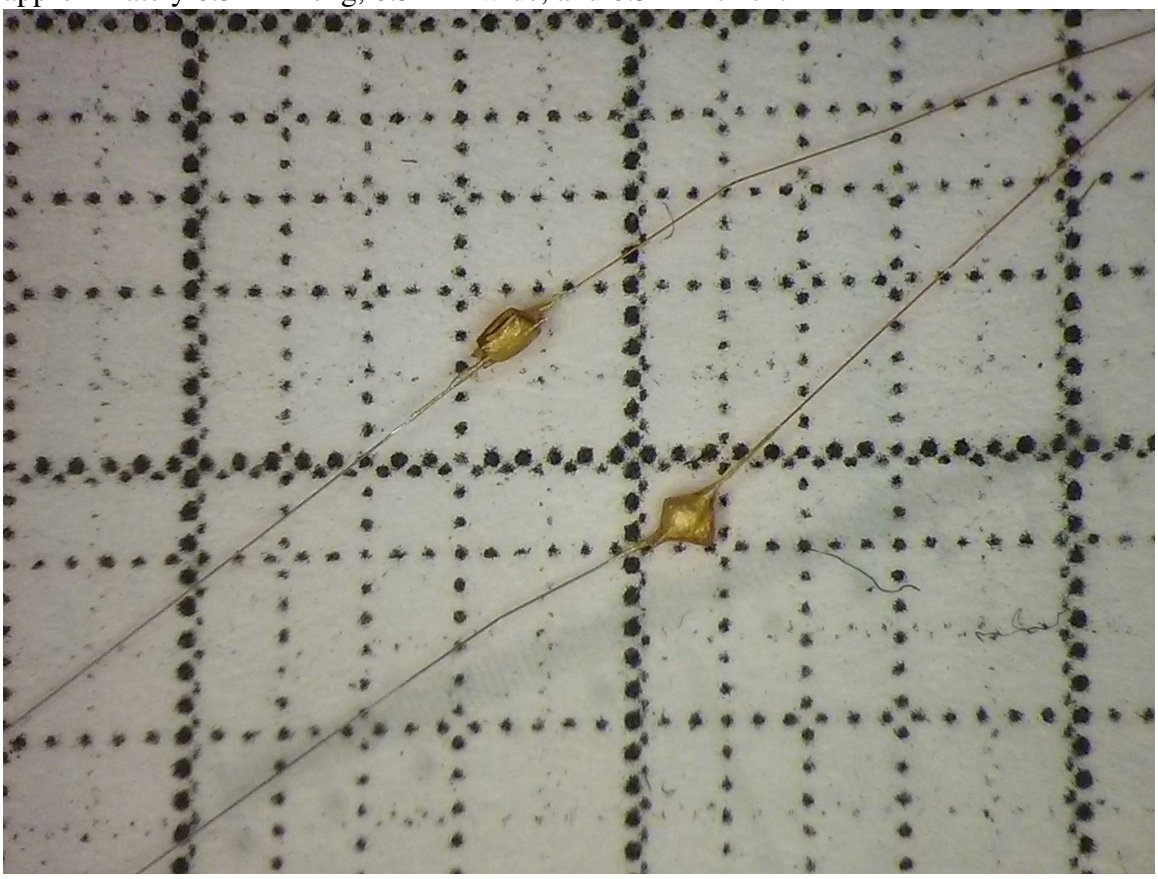

Figure 2.7: An example calibration curve for an STO thermometer, showing both the capacitance (solid) and sensitivity (dashed) as a function of temperature. The capacitance begins to saturate at low temperature, with the sensitivity peaking around 25K.

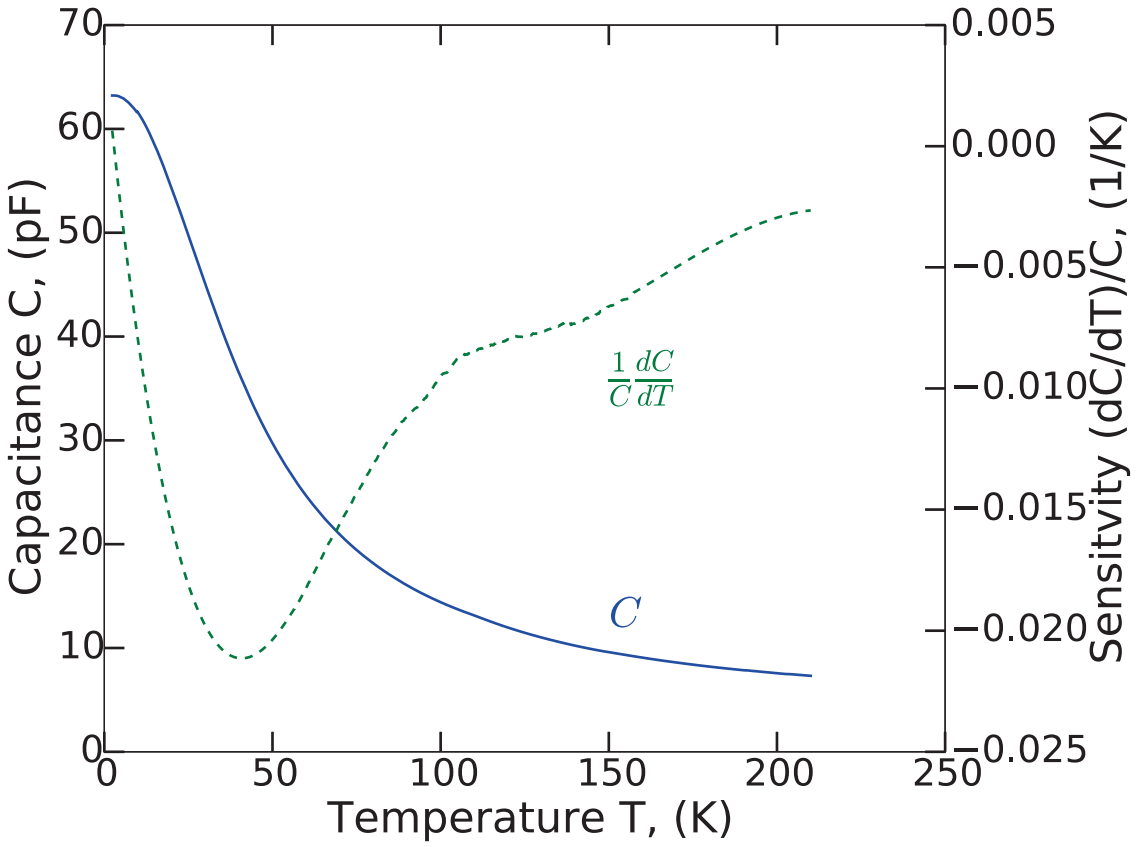

Figure 2.8: A test of the response of an STO thermometer with a capacitance of 65 pf to an applied magnetic field, taken at 4.2K. The field starts at zero, scans to 10T (blue), then to -10T (green), and then back to zero (red). The relative change in the capacitance $(C - C_0)/C_0$ remains less than 3×10^{-4}, corresponding to change of about 20 femtofarads. This change in capacitance is possibly due to the shifting of the leads to the capacitor plates due to the field, rather than anything intrinsic to STO.

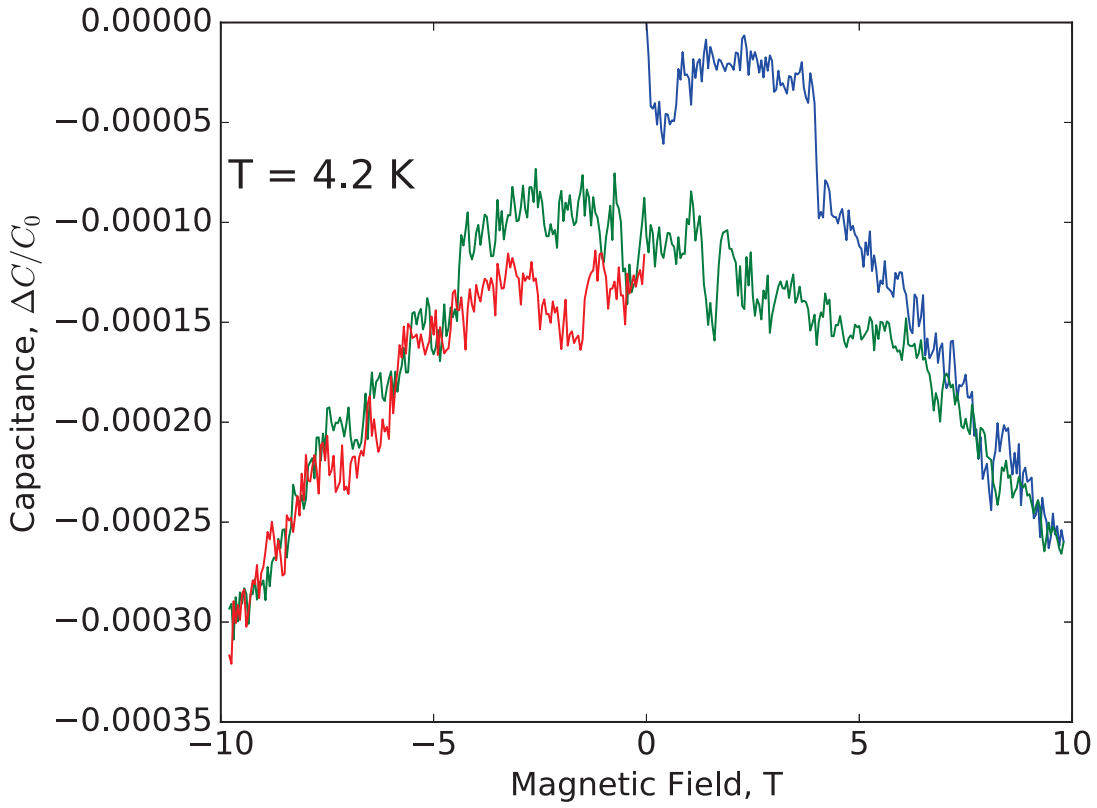

process which these thermometers eliminate.

Of course, in order to perform well for making thermal Hall effect measurements, these thermometers must not be sensitive to an applied magnetic field. Figure 2.8 shows the relative change in capacitance $(C - C_0)/C_0$ of a sample thermometer measured under a magnetic field from -10 T to 10 T. The magnitude of the change in capacitance remains less than 3×10^{-4}, a few parts in ten thousand, below 10 T at 2 K. Compare this to resistive thermometers, which may have magnetoresistance of a few percent or greater in this temperature range[34, 35]. We are not sure what the nature of this small field dependence is, as the dielectric constant should be independent of applied magnetic field. However, at

least some of the change may be related to the slight shifting of the thermometer leads as the field is swept.

Another issue concerning the suitability of these thermometers for measuring the thermal Hall effect, particularly relevant at low temperature, is the heating caused by the thermometers themselves. As the temperature decreases and the dielectric constant increases, the dissipative losses from the capacitor increase as well. These increase to about 60 nW at low temperature. For our current experiment, which applies 1 mW of power across the sample, this is not a concern. In general, however, this is not insignificant. 60 nW corresponds to an excitation of 1 V. Decreasing the excitation will quadratically decrease the heating power, however this comes at the cost of the sensitivity of the device. This at least gives us some room to adjust the parameters to fit the particular experiment. As our process for assembling the thermometers improves, we should be able to mitigate this source of heat by reducing resistive loss across the capacitor. Despite the difficulty with the thermometer heating, the fact that the thermometers are insensitive to magnetic field at low temperature makes them good candidates for making a variety of thermal measurements.

Furthermore, the heat loss through the thermometer leads are negligible compared with the sample's thermal conductance. Each thermometer has a pair of 25 μm diameter phosphor bronze leads, with a thermal conductivity of 69.9 $\mathrm{W/m \cdot K}$ at room temperature given by the manufacturer (California Fine Wire Co) [36]. On the other hand, bismuth (on which we have performed thermal Hall effect measurements described in the next section) has a thermal conductivity of 7.87 $\mathrm{W/m \cdot K}$ at room temperature [24]. Given the dimensions of our sample and the fact that there are two thermometers with four leads total, this results in a thermal conductance of 1.6 $\mathrm{mW/K}$ through the sample compared to 0.027 $\mathrm{mW/K}$ through the leads, almost 60 times smaller. Since the thermal conductivity of bismuth goes up below room temperature [37], while that of phosphor bronze goes down [24], the quality will only improve at the measurement temperatures.

2.4 Measuring the Thermal Hall Effect in Bismuth

As mentioned previously, measurements of the thermal Hall effect on crystalline bismuth have been carried out by W. Kobayashi *et al.*[3] down to 75 K and magnetic fields up to ± 3 T (see figure 1.7). Using our thermometers, we sought to extend this measurement to lower temperatures and higher fields. A resistive heater was mounted on a single crystal of bismuth metal, in order to generate a temperature gradient. A pair of $SrTiO_3$ thermometers were mounted in order to measure the transverse temperature gradient. The thermometers were glued to the surface of the sample and then coated in Type 120 silicone thermal joint compound to ensure good thermal contact with the sample. Similar to the measurement performed by Kobayashi et.al., the heat current was applied along the bisectrix, the transverse gradient was measured across the binary axis, and the magnetic field applied parallel to the trigonal axis. An example set of temperature gradient data is shown in Figure 2.9. As shown in the figure, there is a significant amount of pickup from the thermal conductivity in the measured transverse thermal gradient. This can be eliminated by antisymmetrizing the thermal gradient with respect to the applied magnetic field. Two pairs of thermocouples were mounted as well, one longitudinal and one transverse, in order to independently measure the temperature gradients *in situ*. A comparison between the gradient measured with the thermocouples and the capacitive thermometers is shown in figure 2.10. At high temperature, the transverse thermal gradient can be measured with both the thermocouples and the STO thermometers, although the thermocouples are more sensitive. This manifests as more noise in the measured STO gradient. However, at low temperatures, the STO thermometers can detect a small thermal gradient when the thermocouples detect no signal. An additional resistive thermometer was mounted nearby to calibrate the $SrTiO_3$ thermometers in zero field. The heater was repeatedly turned on and off, and the gradients in each direction measured. Simultaneously, the applied magnetic field was swept between -10 T and 10 T. This allowed us to measure the field dependence of the thermal Hall coefficient.

Similar to what was measured before[3], the thermal Hall conductivity is strongly non-

Figure 2.9: (Panel a): Transverse temperature difference as a function of applied magnetic field from -10 T to 10 T, taken at 130 K and measured using a pair of STO thermometers. The signal is composed of an symmetric part and an antisymmetric part. (Panel b): Antisymmetric (solid) and symmetric (dashed) parts of the transverse temperature difference. The antisymmetric part is the thermal Hall signal. Notice the difference in scales for the two curves.

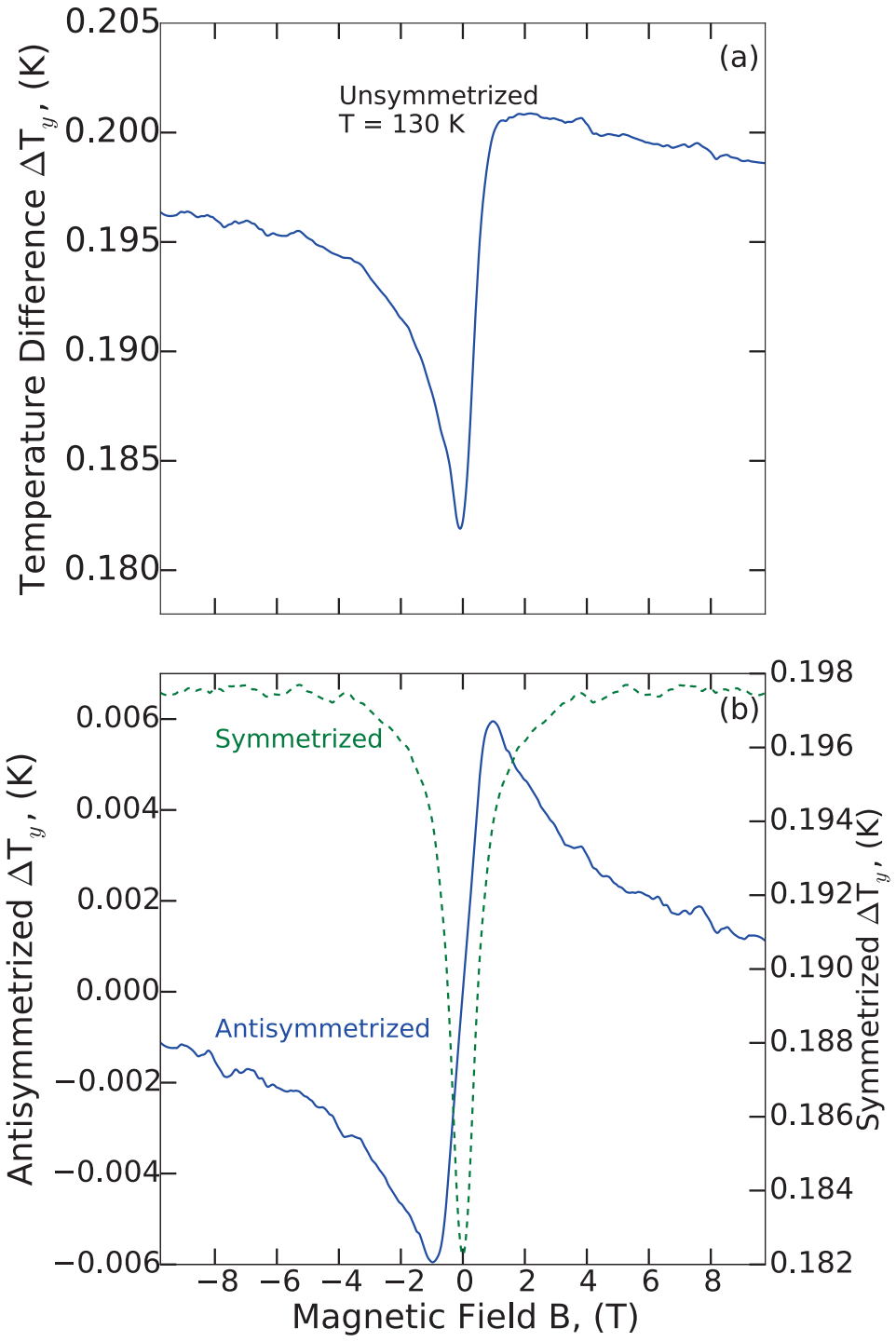

Figure 2.10: Transverse temperature differences across a bismuth crystal measured with both STO thermometers (orange) and thermocouples (blue), up to 10T and antisymmetrized to isolate the thermal Hall signal. Top: Temperature difference at 110K. At this temperature, the signal is large enough that the thermocouples have no trouble detecting it. The STO thermometers are not so sensitive in this range, and so they have more noise. Bottom: Temperature difference at 30 K. While the thermocouples are not able to detect anything, the STO thermometers are still able to detect a temperature difference of about 0.5 mK.

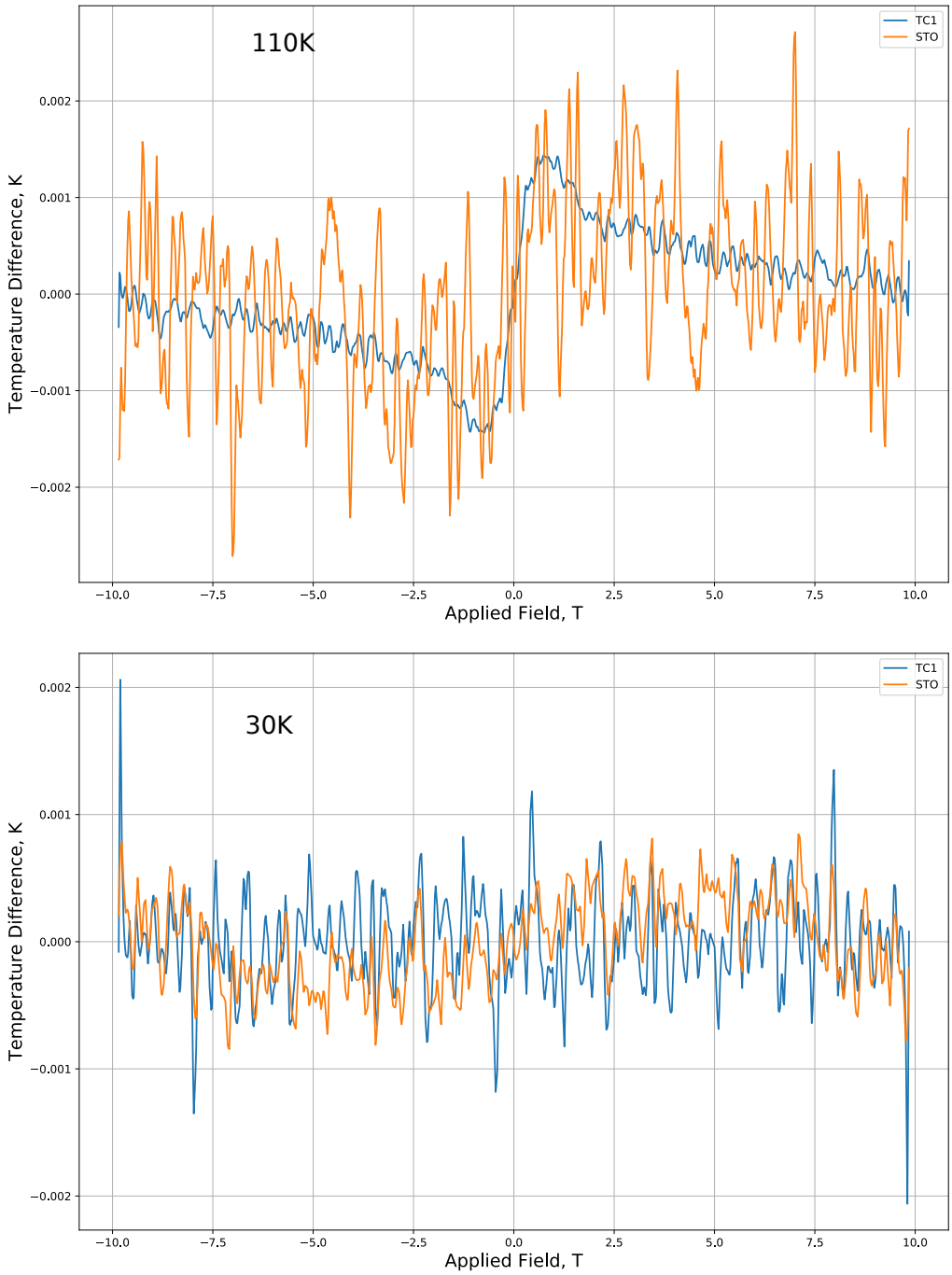

Figure 2.11: Thermal Hall conductivity, computed from the transverse temperature difference measured using the STO thermometers from -10 T to 10 T. Curves for a few temperatures between 90K and 175K (Panel a) and between 40K and 80K (Panel 6). The signal appears to get smaller at lower temperature, disappearing at 60K.

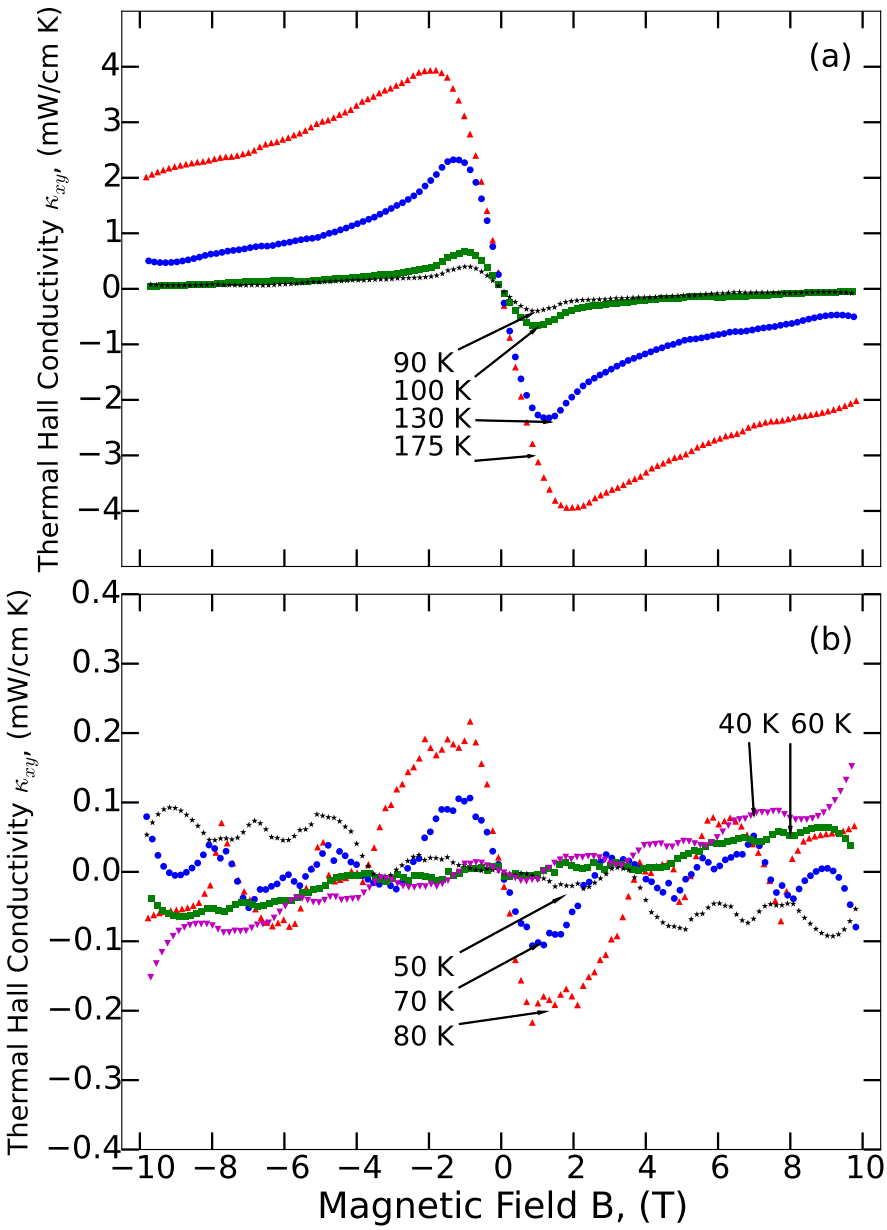

linear, reaching a maximum below 2 Tesla and decaying down to zero at high field, as shown in Figure 2.11. One might suspect that the dropoff at high field is a result of the quantum limit, where all the carriers are contained in the lowest Landau level and gapped out, effectively making the material an insulator and suppressing the thermal Hall conductivity. Since the quantum limit for bismuth is around 8T for this orientation [23], and the thermal Hall conductivity starts to decay around 2T, this explanation does not make sense. Instead, this is a result of the physics described in section 1.3. At high fields, the thermal Hall coefficient is proportional to the cube of the sum of the two (electrical) Hall coefficients, which have similar magnitude but opposite sign. Thus, the magnitude of the thermal Hall conductivity drops off significantly at high field. It is also largest at high temperature, becoming imperceptible below 50 K, where our thermometers are most sensitive. This is also consistent with the two-band picture presented in section 1.3. As a result, we are confident that this is not an artifact of the capacitive thermometers. The qualitative features of the thermal Hall conductivity are consistent with what is expected from the two-band picture. Thus we can see that the STO thermometers are able to make sensitive measurements, detecting changes in temperature below 1 mK in magnetic fields up to 10 T. Additionally, the fact that they are relatively simple to produce makes them applicable to a wide variety of measurements and samples. One remaining challenge is our ability to push these measurements to lower temperature, suitable for use at helium-3 or dilution refrigerator temperatures, where traditional methods of thermometry are even more fraught[34, 35]. One promising line of study involved isotopically substituting ^{18}O into the strontium titanate wafers, which has been shown[30] to drive them closer to the ferroelectric quantum phase transition and thus continue the divergence of their dielectric constant to lower and lower temperature. In the next chapter, we will discuss our attempts to develop thermometers based on this principle. In any event, as this measurement has shown, this method of thermometry holds great promise for enabling the thermal properties of materials in intense magnetic fields.

In conclusion, miniature capacitive thermometers based on the paraelectric material $SrTiO_3$ have been applied to measure the thermal Hall effect in crystalline bismuth. A strong nonlinear thermal Hall effect is observed in the intermediate temperature range. The miniature $SrTiO_3$ thermometers show very little magnetic field dependence – less than a factor of 3×10^{-4} up to magnetic field 10 T. They are also quite sensitive, resolving the temperature difference as little as 0.1 mK.

2.5 Annealing Strontium Titanate in Oxygen-18

Having established the viability of using strontium titanate microthermometers to measure temperature, we now seek to improve their low temperature sensitivity. In the next chapter, we will discuss thermal measurements on a frustrated quantum magnet system. These systems are of great theoretical and experimental interest, but they often require measurements at very low temperatures, even below that of liquid helium. Since strontium titanate is deep in the quantum paraelectric phase at these temperatures, we can't use unmodified STO microthermometers in this range. However, experiments have shown [30] that strontium titanate can be pushed past the quantum critical point by substituting the oxygen in its lattice by isotopically pure oxygen-18. As noted in the phase diagram in figure 2.2, completely ^{18}O enriched STO is a ferroelectric, and partially enriched STO falls somewhere in the middle. Our goal, then, is to push our STO thermometer chips as close as possible to the quantum critical point without going over it. This will result in the quantum critical regime persisting to lower and lower temperature, allowing for the $1/T^2$ dependence of the dielectric susceptibility to continue to lower temperature.

In order to accomplish this, we have constructed a system for annealing chips of strontium titanate in an oxygen-18 environment. Figure 2.12 shows a schematic of its construction. It is composed of a tube furnace connected to an oxygen 18 supply tank obtained from the Sigma-Aldrich corporation [38]. Since oxygen-18 is a stable isotope, it can be saved

Figure 2.12: Schematic of the annealing system used to produce oxygen-18 enriched strontium titanate wafers. The circles labeled "P" are pressure gauges, and the circles with crosses are valves. Oxygen-18 is supplied from a gas cylinder, and can be stored in the cold trap for reuse.

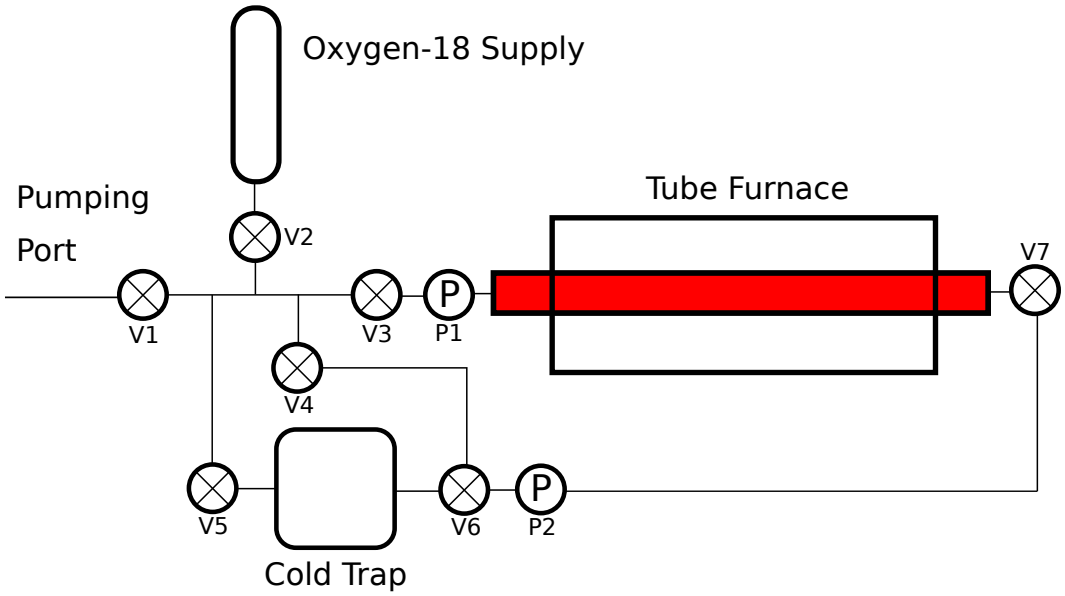

Sample #	Initial Mass	Final Mass	^{18}O Enrichment	Annealing Conditions
1	13.62 mg	13.77 mg	33 %	3 days at 980 °C, 0.87 atm
2	14.78 mg	14.50 mg	-57 %	as above
3	15.71 mg	15.97 mg	50 %	7 days at 1000 °C, 0.95 atm, then 5 days at 800 °C in vacuum
4	16.77 mg	16.67 mg	18 %	7 days at 1050 °C, 0.80 atm
5	16.51 mg	16.85 mg	62 %	as above
6	16.40 mg	16.83 mg	78 %	as above

Table 2.1: Annealing conditions for the various STO thermometers chips, along with the ^{18}O enrichment measured from the mass change.

and reused long term. Thus, a cold trap is also connected to reuse the expensive isotopically pure gas. The system also has a pumping port for annealing the chips in vacuum, if desired. Thus, we can control the gas environment in order to experiment with the annealing conditions. Table 2.1 shows the annealing conditions for six samples of strontium titanate chips, cut from 0.5 mm thick wafers. The percentage of oxygen-18 incorporated into the samples is calculated by measuring the change in their mass. Using the standard atomic weights for strontium, titanium, and oxygen, the atomic mass of standard strontium titanate is 183.484 amu. If all the oxygen has been totally replaced with oxygen-18, the atomic mass should be 189.484 amu, an increase of 3.27%. By normalizing the observed increase in mass to this percentage, we can determine the approximate oxygen-18 enrichment.

Looking at table 2.1, however, it appears that the enrichment percentage is not very consistent. Samples annealed under the same conditions appear to have differing enrichment percentages. One sample, number 2, appears to have even lost mass. This is especially concerning, as oxygen-deficient strontium titanate has been observed to become metallic [39]. There are several reasons the samples may have different observed masses. One is that we are simply not measuring the mass accurately. For a 15 mg sample, a 3.27% mass increase corresponds to a change in the mass of 450 μg. This is on the edge of what is possible to measure with an analytical balance, and such measurements can be affected by difference in electrostatic conditions. Since the measurements must be taken several days apart by ne-

cessity, it is difficult to control these conditions precisely. Secondly, even for the samples which are observed to gain mass, it is difficult to determine if the oxygen-18 has been uniformly distributed within the bulk of the sample. All of the samples are relatively thin, each being approximately 5 mm by 5 mm by 0.5 mm. This should facilitate an even distribution of oxygen-18. It is difficult to determine for sure if this is the case, however. One potential method to get a more even distribution is to anneal the samples in vacuum after they have been annealed in the oxygen-18. This runs the risk of creating oxygen-deficient samples, which as metals would make poor capacitive thermometers. Determining the optimal annealing conditions is an ongoing project. Each annealing run can last a week or more, so getting it correct will take more time. However, we can discuss the results on the devices we have tried.

Thermometers we made out of the STO chips in the same manner as the unannealed devices described above. The capacitance of these were measured using the AH2700A digital capacitance bridge on the dipstick probe in a helium dewar. This probe allows us to make quick measurements down to liquid helium temperatures, which is important for testing many devices quickly. The results for this experiment are shown in figure 2.13. Chips from sample 3 through 6 were used for these experiments. Curves for the cool down from room temperature to 4 K as well as the warm up back to room temperature are plotted on top of one another. As shown in the figure, these curves to not line up with one another for any of the four devices tested. There appears to be some hysteresis, where the cool down curve is slightly larger than the warm up curve between 10 K and 120 K. This plot also shows the sensitivity of the devices, plotted in the same $\frac{1}{C}\frac{dC}{dT}$ units as for the unannealed thermometers. In general, it appears that rather than having one minimum as for the unannealed devices, there are two, at approximately 80 K and 120 K. This may be an indication that part of the sample is more enriched that others. The only one which does does not display this behavior is sample 3, which was annealed for a time in vacuum (see table 2.1). This one has a flatter minimum, possibly indicating a more uniform

Figure 2.13: Top: Reproducibility tests for several annealed STO capacitor devices, measured in a liquid helium dewar using a dipstick probe. The Oxygen-18 enrichment percentage is listed in table 2.1. Note the offset between the cool down and warm up traces for each device. Bottom: Sensitivities for the same four devices. Although the capacitance varies between devices and cool down/warm up, the sensitivity is roughly the same for each.

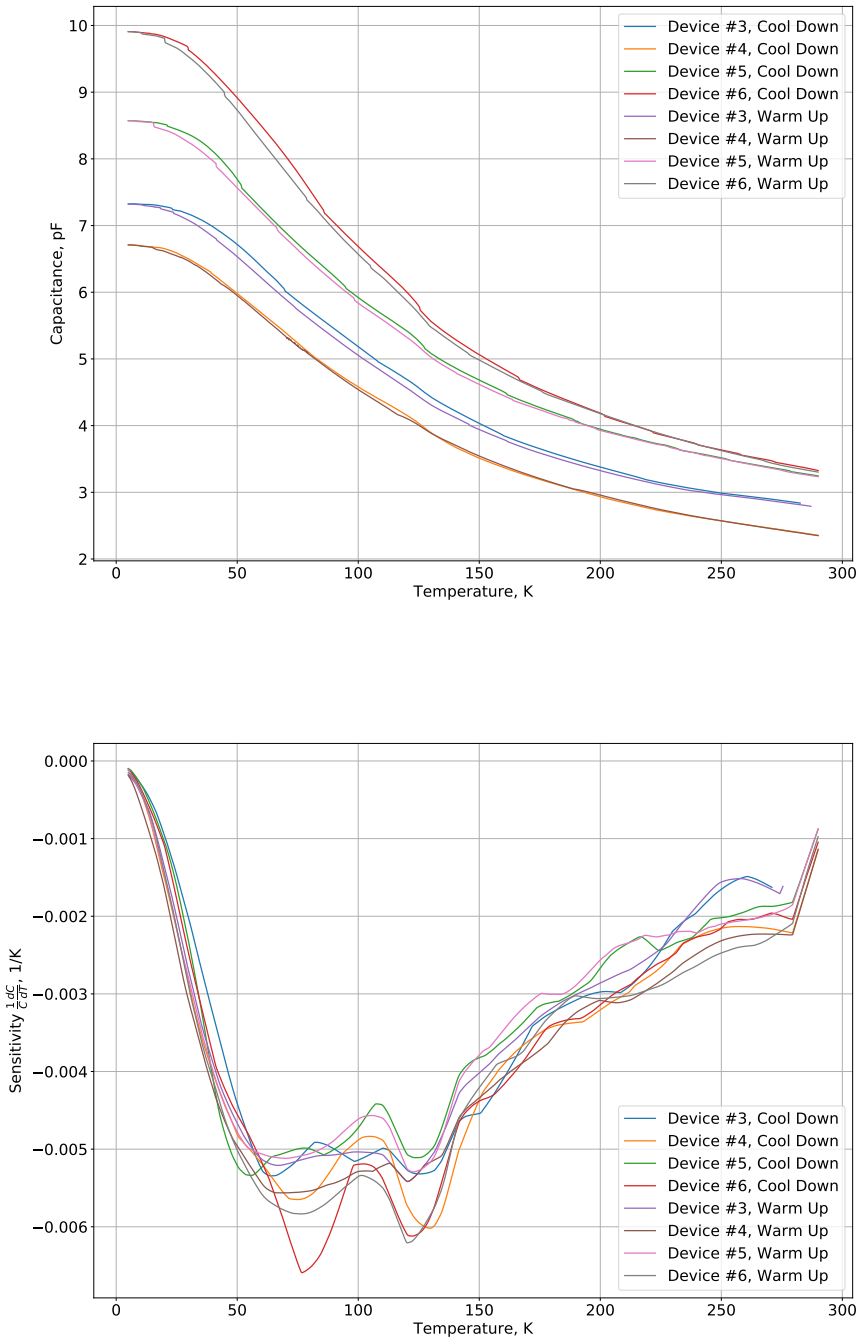

distribution of oxygen-18 in the lattice. Otherwise, at low temperature, the curves appear to collapse onto one another below 50 K. It does not appear that they are getting significantly more sensitive at low temperature, which could also indicate that most of the bulk is not significantly enriched.

Figure 2.14 shows some additional data on the dissipation of the thermometer devices. This is a plot of $\tan\delta$, where δ is the deviation of the impedance phase angle from from $-\pi/2$, as would be expected for a pure capacitor. If we model the device as a capacitor with capacitance C_p in parallel with a resistor with large resistance R_p, the dissipation is given by [40]

$$\tan\delta = \frac{1}{\omega C_p R_p}$$

where ω is the excitation frequency. Thus, this gives a measurement of how well the device can be modeled as a pure capacitor that is independent of the magnitude of the capacitance. As we can see, the dissipation does not increase for any of the devices tested. This serves as a good indication that we are not depleting a significant amount of oxygen and turning the chips metallic.

There are two additional tests we have run on some of these thermometers. First of all, we wish to preclude the possibility that the devices have been pushed into the classical ferroelectric regime. Although the dielectric susceptibility will still diverge below the Curie temperature T_c, this would still present a hard limit on the temperature range in which the devices are useable. Furthermore, once the strontium titanate has been pushed past the quantum critical point, T_c is predicted to increase as the square root of the quantum tuning parameter $a/c\Lambda^2$, very rapidly increasing the Curie temperature [29] (see figure 2.2). The bottom panel of figure 2.14 shows a measurement of the heat capacity of sample 6, with the highest apparent enrichment. These were carried out using the Dynacool PPMS heat capacity option. If there is indeed a phase transition to a ferroelectric state, this should be visible as an anomaly. However, the behavior is consistent with a simple insulating behavior predicted by the Debye model. This casts further doubt that the enrichment is as high

Figure 2.14: Top: Dissipation of the STO thermometer devices, plotted as the tangent of the impedance angle $\tan\delta$. Low dissipation indicated capacitive impedance. None of the samples appear to be metallic. Bottom: Heat capacity measurement of a strontium titanate wafer (blue dots), measured using the Quantum Design PPMS. The measurement does not show any power law behavior indicative of a phase transition, and so it has not been doped into the ferroelectric regime. The cubic fit (orange line) is indicative of simple insulating behavior.

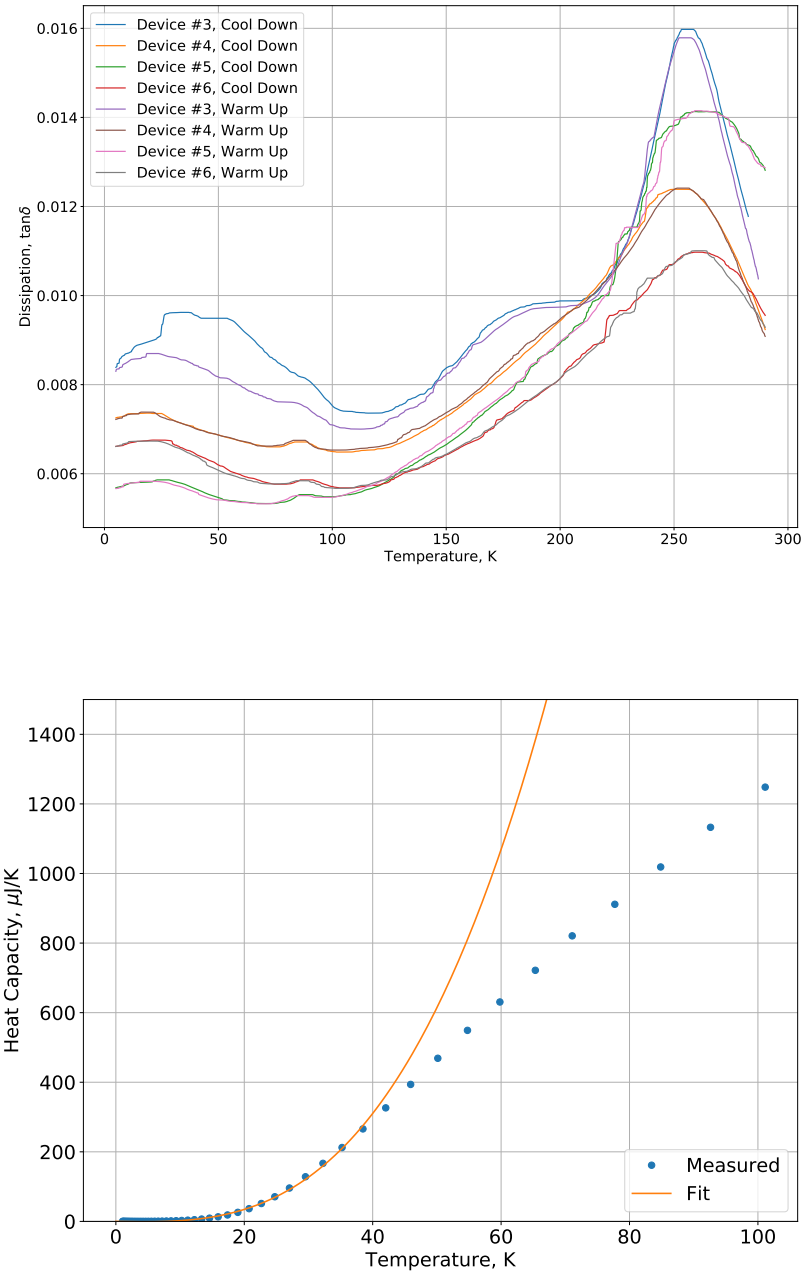

Figure 2.15: Relative change in capacitance of an annealed STO thermometer in an applied magnetic field, measured up to 14 Tesla in the Quantum Design PPMS at 1.5 K. The initial capacitance is about 35 pF. The improved sample mounting in the PPMS eliminates the background from the flexing of the wires, and the trace is mostly independent of the applied field.

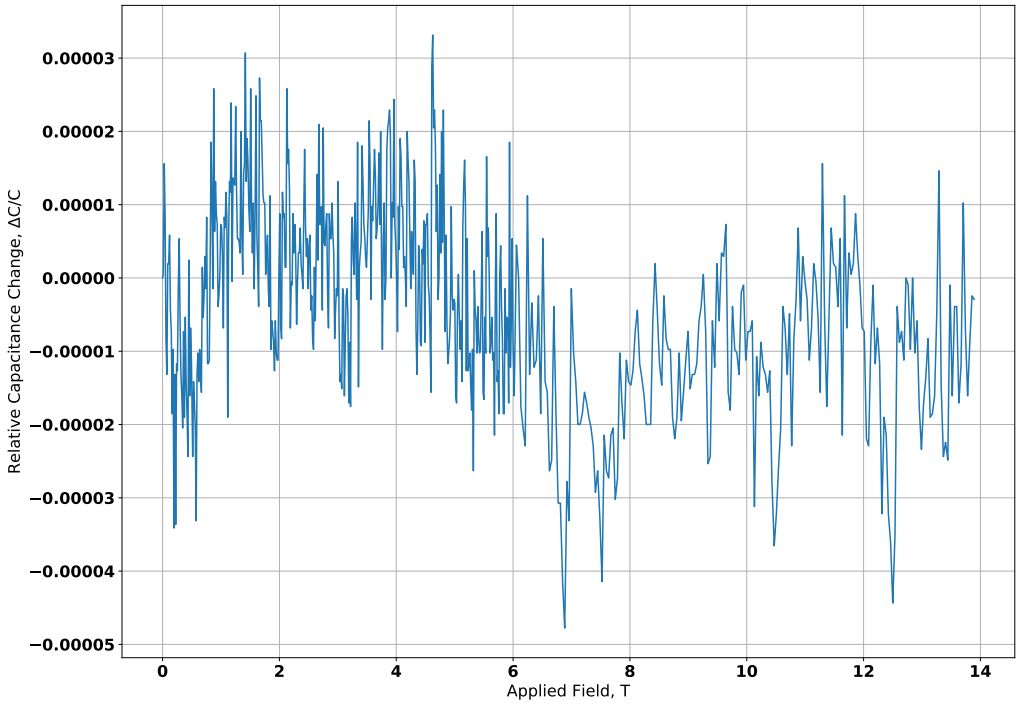

as we have determined from the mass. Finally, figure 2.15 shows the field dependence of the measured capacitance for sample 3. This was also measured using the Dynacool PPMS He-3 probe, which has been modified to add a pair of coaxial cables suitable for making capacitance measurements. This probe eliminates much of the issue we had with wire flexing when making a similar measurement in the VTI with the Janis cryostat, and we can see that there is very little field dependence. This at least indicates that there are no multiferroic effects introduced by the oxygen-18 annealing, which would make the thermometers unsuitable for their intended purpose replacing resistive thermometers at low temperature.

There is much we are still trying to understand about the process for making these thermometer devices. As mentioned above, the pace of iteration on what we have learned is slowed significantly by the long annealing time required. Much more precision in how we are able to control the oxygen-18 enrichment of strontium titanate is clearly required. However, the tools are in place for this research to continue. The most interesting states of matter can be found at the lowest temperatures. In the next chapter, we will motivate this research into low-temperature thermometry by describing thermal measurements conducted at on a frustrated magnet system.

CHAPTER 3

Thermal Measurements of Strontium Copper Borate

3.1 The Shastry-Sutherland Model

For the above portion of this work, we have mostly talked about thermal measurements of metals. This is a subject which has been studied for many decades at the point. In recent years, there has developed an interest in making thermal measurements on a class of magnetic materials whose properties derive from the geometry of their lattice structures: frustrated magnets. Consider a square lattice of spin-1/2 sites, with antiferromagnetic coupling, i.e. with a Hamiltonian given by

$$H = J \sum_{\text{n.n.}} s_i \cdot s_j$$

where the sum is over pairs of nearest-neighbor sites, and J is positive. Each s_i can take the value 1 or -1, or alternatively spin up or spin down. We will say that a particular bond between two sites is "satisfied" if the sites take values which minimize the energy, which in this case implies they have opposite spins. In the case of a square lattice, we can minimize the total energy by simply fixing one of the sites (e.g. $s_i = 1$), fixing its neighbors with the opposite spin, and repeating this process until every spin is determined. This process will determine the spin at each site unambiguously (up to our initial choice for the first site).

Figure 3.1: A simple example of frustration in a spin system. If the spins (gray circles) are antiferromagnetically coupled, all of the bonds cannot be satisfied simultaneously. Thus, this arrangement of spins has no unique ground state.

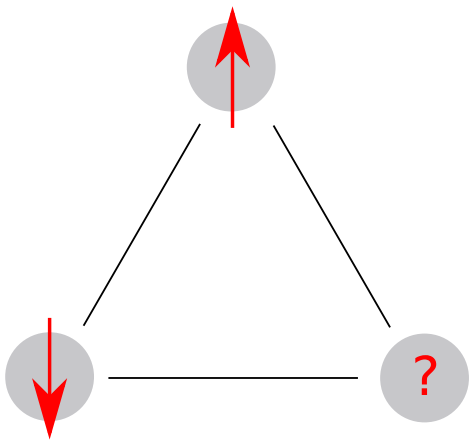

This process does not always work for a general lattice, however. For a simple example, apply the above spin Hamiltonian to the triangle of sites depicted in figure 3.1. Say we fix the top spin to be up. We can satisfy the bond with the site on the lower left by making it down. But what about the site on the lower right? If we make it spin down, the bond with the spin on the lower left won't be satisfied. If we make it spin up, then the bond with the top spin won't be satisfied. Indeed, for the $2^3 = 8$ possible arrangements of spins on this triangle, six of them have energy $-J$ (the other two, which have all the spins in the same direction, have energy $3J$). This is the essence of frustration: the geometry of the lattice interferes with the formation of long range order.

There has been a great deal of theoretical and experimental research conducted on materials with this sort of frustration. There are many examples of materials with lattice structures involving triangular or tetrahedral elements, and frustration in such materials has the potential to create quite exotic magnetic phases. Since these materials are generally

insulators, but may have magnetic excitations that don't carry charge such as magnons, thermal measurements such as the thermal Hall effect are an important tool for studying these phases experimentally. One example are so called spin ices in pyrochlore systems such as $Lu_2V_2O_7$ [7] and $Tb_2Ti_2O_7$ [8]. The pyrochlore lattice is made up of a series of interconnected tetrahedra. The term spin ice derives from the nonzero entropy in these systems due to the frustration which is analogous to a well known structural frustration in water ice [41]. Both of these materials have relatively large thermal Hall effects considering they are insulators. Another class of materials of great interest are quantum spin liquids [42]. In these materials, frustration prevents the formation of any magnetic ordering at low temperature, resulting in a state with many exotic properties, such as fractional excitations and long range quantum entanglement. Due to the potential for such an exotic phase of matter, there has been intense experimental investigation of spin liquid candidates. Many of these are kagome antiferromagnets, for example herbertsmithite ($ZnCu_3(OH)_6Cl_2$) [43]. "Kagome" refers to the crystal structure of these materials which resembles a particular type of Japanese basket. There has been theoretical [44] and experimental [45] investigation of the thermal Hall effect of these materials. Thermal Hall measurements of spin liquid candidates with hexagonal lattice structures have been performed as well [46]. The field of quantum spin liquids is quite active and bears much more discussion than I have presented here, but suffice it to say there is much the thermal Hall effect techniques presented in this work have to offer in experimental studies of these fascinating materials.

The above discussion might lead one to believe that frustration can only occur in materials with lattices based on triangles or tetrahedra. Certainly most of the compounds of experimental interest are, but one can introduce frustration to a square lattice by adding interactions across the diagonals. There are potentially many different ways of doing this, but the one we will be interested in is depicted in figure 3.2. This model is known as the Shastry-Sutherland model [47]. In it, each spin is paired across a diagonal with exactly one

Figure 3.2: Schematic of the Shastry-Sutherland lattice. Each red circle has spin 1/2. The nearest-neighbor coupling J is represented by the solid lines, and the intra-dimer coupling J_D is represented by the dashed line. Each spin is in exactly one dimer.

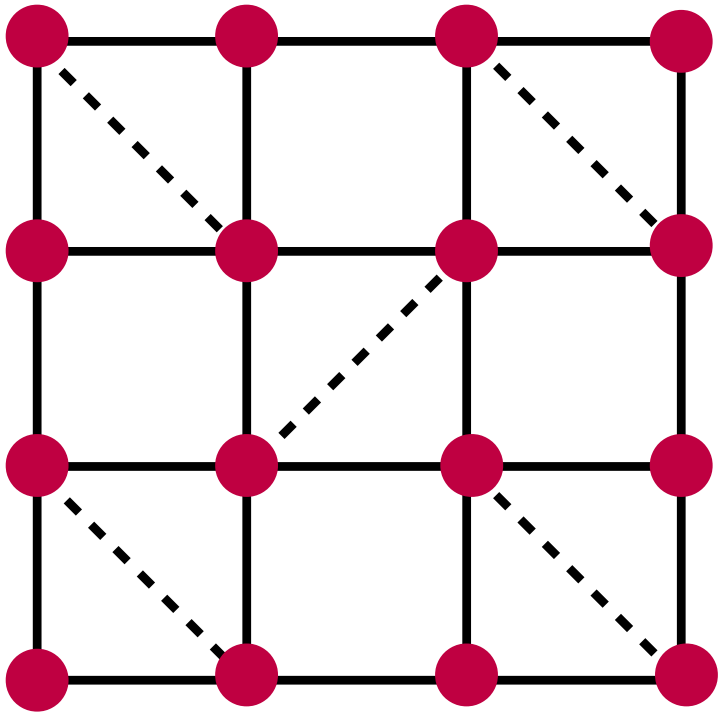

other spin. The spin Hamiltonian is given by

$$H = J \sum_{\text{n.n.}} s_i \cdot s_j + J_D \sum_{\text{diag}} s_i \cdot s_j$$

where the coupling J is between nearest neighbors on the square lattice (solid in the figure) and J_D is between the diagonals (dashed in the figure). The ground state of this Hamiltonian of course depends on the relative values of J and J_D, but there are two cases we can consider intuitively. If J is much stronger than J_D, we effectively have the square lattice antiferromagnet again. The more interesting case is when J_D dominates over J: each pair of spins connected by a diagonal hybridizes to form a singlet state give by

$$|s\rangle = \frac{1}{\sqrt{2}}(|\uparrow\downarrow\rangle - |\downarrow\uparrow\rangle)$$

with the full ground state being a direct product of these singlets. The odd parity of the singlet state with respect to exchange of the spins in each dimer actually ensures that the J term does not contribute to the energy at all [48].

Each individual dimer also has excited states given by the three triplets:

$$\begin{aligned} |t_1\rangle &= |\uparrow\uparrow\rangle \\ |t_0\rangle &= \frac{1}{\sqrt{2}}(|\uparrow\downarrow\rangle + |\downarrow\uparrow\rangle) \\ |t_{-1}\rangle &= |\downarrow\downarrow\rangle \end{aligned}$$

These triplets all have even parity with respect to exchange of the spins within the dimers, so one might expect that they would have strong dispersion. Actually, the triplets are highly localized, and this is a result of the frustration in the lattice [47]. Specifically, each spin in a dimer is connected to each of its neighboring spins in a triangle formed with two J couplings and one J_D coupling. Thus despite the strong interactions between the dimers, the triplet states are completely dispersionless in this model.

Figure 3.3: (a): Crystal structure of Strontium Copper Borate, with the c axis out of the page. The copper atoms (copper colored) make up the Shastry-Sutherland lattice. The strontium atoms (green) are set back into the page by half a unit cell. Image generated using Jmol [20]. (b) through (d): Diagram demonstrating the equivalence of the crystal structure of SCBO to the Shastry-Sutherland lattice. To go from the SCBO lattice to the Shastry Sutherland lattice, we elongate the distance between the dimer pairs until the diamond shape containing them has been turned into a square. Reproduced from [47].

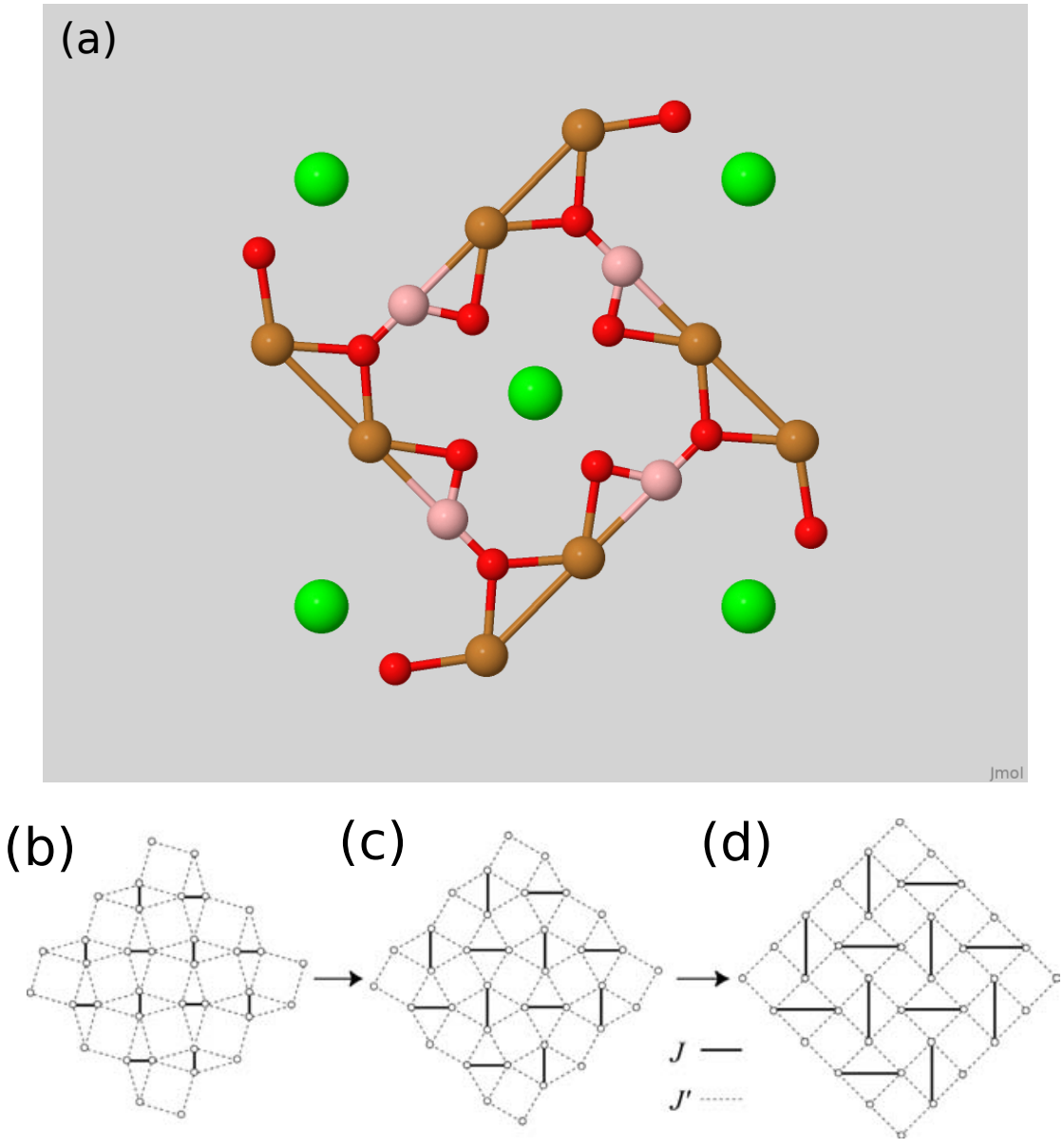

Figure 3.4: Magnetic moment of a Strontium Copper Borate sample, taken at 1 T. The behavior is indicative of the triplon spin gap.

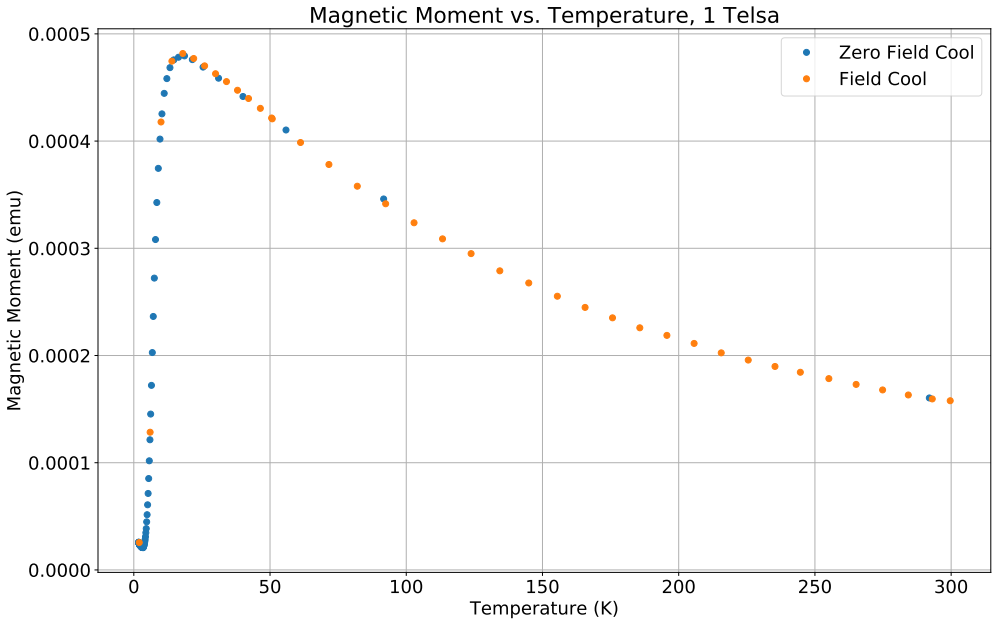

Fascinating as this model is, it is not of much experimental interest unless it can be realized as an actual material. There are some clear difficulties with this in principle, particularly if we are interesting in the dimer ground state. Monte Carlo simulations have shown that in order to get this phase, we must have $J/J_D < 0.7$, i.e. the intradimer coupling must be stronger than the interdimer coupling by a few tens of percent [48]. If the lattice looked like that depicted in figure 3.2, each atom would need to be more strongly coupled to an atom diagonal from it than from it's nearest neighbor! There is, it turns out, one material which can be modeled by the Shastry-Sutherland Hamiltonian, and that is $SrCu_2(BO_3)_2$ (Strontium Copper Borate, commonly abbreviated SCBO). Figure 3.3 shows its crystal structure, which at first glance bares little resemblance to the Shastry-Sutherland lattice. It is, however topologically equivalent: the squares in the Shastry-Sutherland lattice have been turned into diamond shapes, with the short axis corresponding to the dimer pair. Thus, the intradimer coupling J_D can plausibly be stronger than the interdimer coupling J.

What experimental evidence exists that the ground state of SCBO looks like the direct product of singlets described above? One simple way of checking is by measuring the magnetic susceptibility. Figure 3.4 shows the magnetic moment of a sample of SCBO as a function of temperature with an applied field of 1 T, measured using the Vibrating Sample Magnetometer in our Dynacool PPMS system. At high temperatures, the dependence looks qualitatively like Curie-Weiss $1/T$ behavior. However, the magnetic moment drops precipitously at low temperature, indicating the opening of a spin gap. This is consistent with what was described above: The singlet states contribute no net magnetic moment, but the $|t_1\rangle$ and $|t_{-1}\rangle$ triplet excited states do. At low temperatures, these excitations are frozen out. Work by others has used this data to fit for the coupling constants, finding $J/J_D = 0.635$ and $J = 85$K [49]. This puts SCBO barely into the dimer phase, and corresponds to a spin gap of 35 K. Additionally, by measuring the sample in both field-cooled and zero-field-cooled configuration, we can see there is no hysteresis indicating the formation of some other magnetic ordering. Thus we are confident the samples of SCBO actually have a ground state similar to that described above.

In the discussion of the Shastry-Sutherland model above, it was noted that the frustration of the lattice resulted in the triplet states being totally dispersionless. Perhaps this makes sense for a toy model, but in an actual material one would expect some second order effect to introduce some dispersion. This is indeed the case in SCBO, and these mobile triplet states are termed "triplons". The next section will discuss these lower order effects, and the significant implications they have for thermal measurements in SCBO.

3.2 Strontium Copper Borate as a Bosonic Topological Insulator

In order to induce dispersion in the triplon modes in SCBO, we must have an interaction which is not suppressed by the lattice frustration. The simplest way of doing this is by

introducing a so-called Dzyaloshinsky-Moriya (abbreviated DM) interaction:

$$H_{\mathrm{DM}} = \sum_{\mathrm{n.n.}} \mathbf{D} \cdot (s_i \times s_j)$$

The strength of this interaction is characterized by the vector $\mathbf{D}$. This interaction can act both between pairs of spins in a dimer and between the dimers themselves. This results in a full Hamiltonian (including an applied magnetic field h_z):

$$H = J_D \sum_{\mathrm{n.n.}} s_i \cdot s_j + J \sum_{\mathrm{n.n.n}} s_i \cdot s_j + \sum_{\mathrm{n.n.}} \mathbf{D}_D \cdot (s_i \times s_j) + \sum_{\mathrm{n.n.n.}} \mathbf{D} \cdot (s_i \times s_j) - g_z h_z \sum_i s_i^z$$

In this Hamiltonian, "nearest neighbor" refers to the coupling between two spins in the same dimer, and "next nearest neighbor" refers to the coupling between dimers. This is correct when referring to the lattice structure of SCBO, but is the opposite for the Shastry-Sutherland model (see figure 3.3 and the Shastry-Sutherland Hamiltonian from above, where the "nearest neighbors" are along the square lattice, and not within the dimers, as they are in SCBO). The symmetry of the lattice under exchange within the dimers $\mathbf{D}_D$ means that only one component can be nonzero, whereas the interdimer coupling $\mathbf{D}$ can have all three components [50]. Figure 3.5 shows these bands imaged using neutron scattering. The top row shows the experimental data, and the bottom row shows theoretical computations of the bands with the coupling strengths determined using the data. Contrary to the prediction from the Shastry-Sutherland model without the DM interaction, the triplons do not have a totally flat dispersion, and show some splitting without any applied field. The antisymmetry of the DM terms in the Hamiltonian make it compatible with the frustration in the lattice, and so allow the triplons to disperse. This is despite the fact that the DM interaction is small compared to the higher-order effects, the above work found the largest component of D was about 3% as large as J_D [50].

The signature of the DM interaction in SCBO can be observed without doing neutron scattering by performing heat capacity measurements. Figure 3.6 shows measurements

Figure 3.5: Triplon band structure, imaged by neutron scattering by [50], showing dispersion induced by the DM interaction. Experimental data in top row, theoretical calculations in the bottom row.

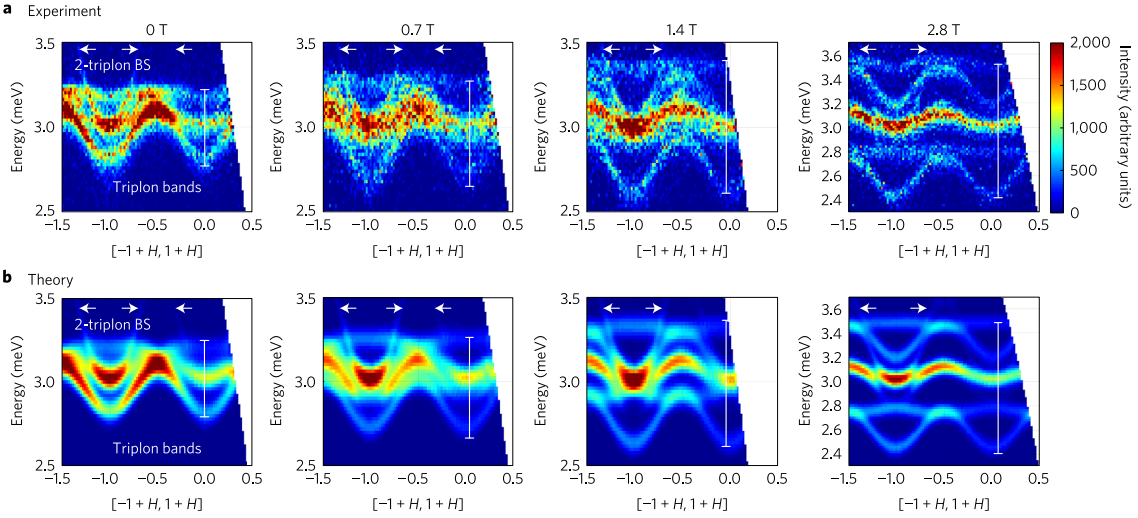

performed on our SCBO samples in our Dynacool PPMS, as well as a comparison to the work done by Jorge et al. [51] At zero field, there is an anomaly in the heat capacity at around 7.5K. This anomaly has been attributed to resonant scattering of phonons by triplet excitations with $s^z = 0$ [52]. Once a magnetic field is applied perpendicular to the Shastry-Sutherland plane, this anomaly shifts lower in temperature as the phonons scatter off triplon states with $s^z \neq 0$. However, once the field is increased to about 10 T to 14 T, a new anomaly begins to grow around 3 K. This second anomaly is due to mixing between the states with $s^z = 0$ and those with $s^z \neq 0$. This mixing is achieved through the DM terms in the Hamiltonian, which do not conserve s^z. Plots from the paper reproduced in figure 3.6 show calculations of the heat capacity for data taken in fields above 22 T where the difference is more apparent. This mixing becomes most apparent when the difference in energy between the states with $s^z = \pm 1$ is comparable to $|\mathbf{D}|$, which is why such strong fields are required to generate it. Thus, the effect of the DM interaction can be observed directly in our samples via heat capacity measurements.

There has been some theoretical work which indicates that the DM interaction has the potential to introduce a new type of physics to this system: triplon bands with nontrivial

Figure 3.6: Top: Field-dependent low temperature heat capacity measurement of Strontium Copper Borate, measured in our Dynacool PPMS system, plotted as C/T to make the presence of two anomalies more clear. Bottom: Heat Capacity plotted as C/T versus temperature, taken from [51]. The symbols are actual data, and the lines are data computed using a fit for the DM interaction. The dashed line in the lower panel is a calculation where the DM term is ignored.

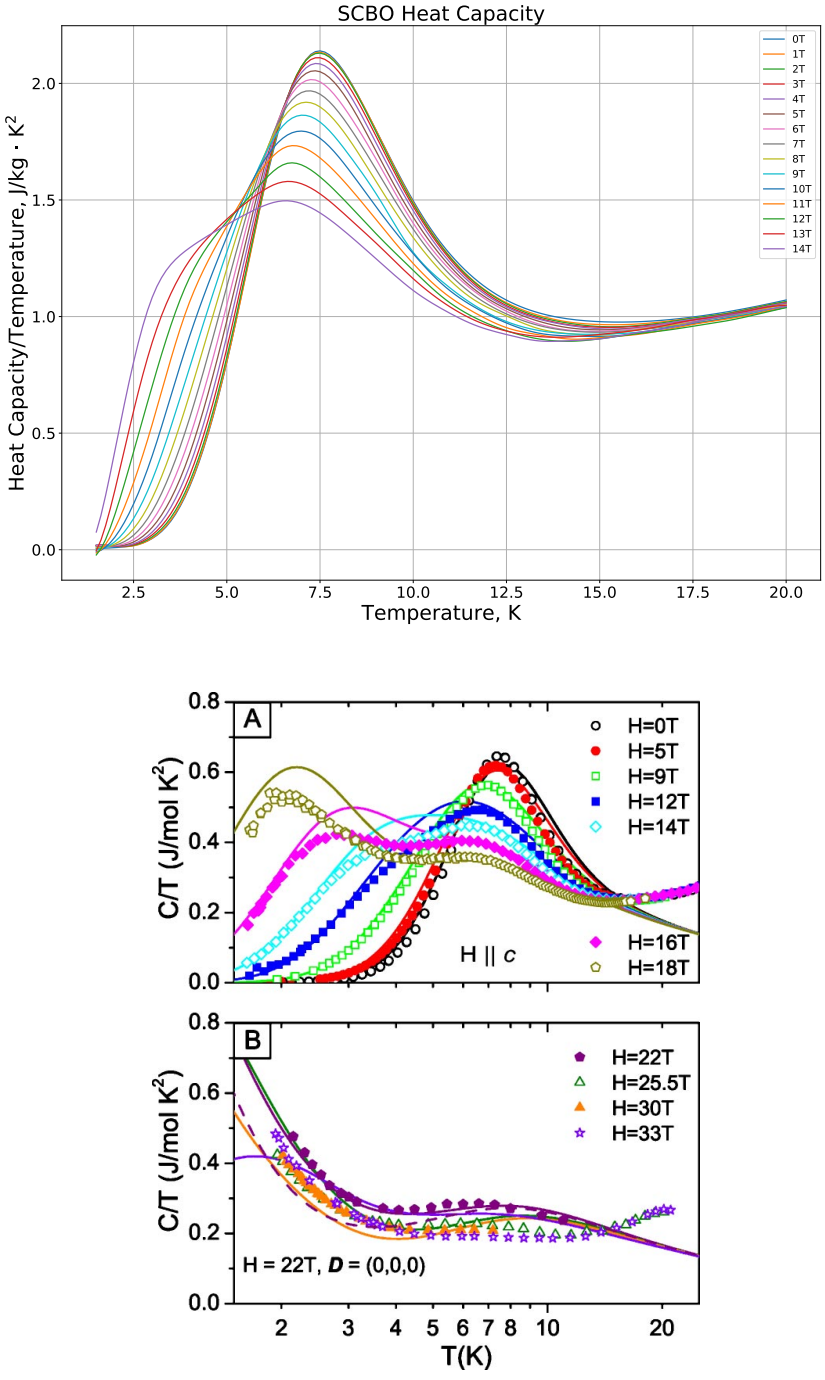

topology. The importance of band topology has recently opened up an entirely new line of research in condensed matter physics, ever since materials with topologically non-trivial bands were predicted [53] and experimentally observed [54] at the end of the first decade of the 2000s. In mathematics, "topology" refers to the study of continuous deformation of geometric objects. "Continuous deformations" can intuitively be thought of as transformations which stretch or compress an object without tearing or puncturing it. Topology is primarily concerned with the properties of such objects which are invariant under continuous deformations [55]. A commonly cited example is the number of holes in an object: a donut can be continuously molded into a coffee mug, while a sphere cannot be continuously deformed into a donut without puncturing it. Such a quantity is known as a "topological index". This particular invariant is sometimes called the "genus" of a surface by mathematicians. When the object in question is a (Reimannian) manifold (loosely, an object which looks locally enough like Euclidean space in which one can do calculus, e.g. the surface of a sphere or a torus), it is possible to compute the genus g by integrating local information on the surface, i.e. its mean Gaussian curvature K:

$$\int_M K dA = 2\pi * (2 - 2g)$$

This is a specific case of the more general Gauss-Bonnet theorem, which in general connects topological invariants to integrals over local information about curvature [56]. Thus, with this local information, we can classify these objects by whether or not they can be continuously deformed to each other.

The significance of this mathematical formalism to condensed matter physics comes through the definition of Berry curvature, which assigns a curvature to a quantum state based on how its quantum phase changes as it is adiabatically transformed into other states [57]. In much the same way that the mean Gaussian curvature can be integrated to find an invariant which classifies which manifolds can be continuously deformed into

others, the Berry curvature can be integrated to produce a topological index known as a Chern number. The Chern number thus indexes which states can be adiabatically transformed into each other in the same was as the genus. In the context of a band structure, states in the same band can be adiabatically transformed into each other, and so all states in a band have the same Chern number. Thus, we conventionally assign Chern numbers to bands. Much of the experimental research on topological bands in condensed matter physics has focused on the topology of electron bands (as opposed to magnon bands such as triplons, for example) in compounds such as bismuth selenide [54]. Here, one of the most important experimental features of electron topology can be observed: the existence of topologically protected surface states. Bismuth selenide has an insulating bulk, its band structure has a gap between two bands with different Chern numbers. However, states of electrons in vacuum outside the crystal have "trivial" topology. Thus, at the interface between the crystal and the outside, the gap must close so that the topology of the bands can be unwound. This has the result of creating conducting surface states which span the gap, even though the bulk material is an insulator. These states are "topologically protected" in the sense that they are a necessary feature of the interface between bismuth selenide and the vacuum (or some other insulator with trivial topology). If one cuts a crystal of bismuth selenide in half, the surface states will appear on the surface without having to modify it in any way. These surface states have many unique properties, such as Dirac-like dispersion and spin-momentum locking (i.e. the direction of their momentum necessarily determines their spin)[53]. Because of these properties, finding materials which host these states has been an area of intense focus for the field in general and our lab in particular [58].

With this background in mind, we can now consider what it would mean for the triplon bands in SCBO to have "nontrivial topology". Figure 3.7 reproduces several figures from a paper by Romhányi et al. which computes Chern numbers for the bands generated from the Shastry-Sutherland Hamiltonian, with the DM interaction terms and the applied magnetic field term. What they have shown is that when a magnetic field is applied, a gap opens

Figure 3.7: Figures concerning chiral edge modes in SCBO, reproduced from [59]. Panels a through e: Schematic of the triplon bands as a function of applied magnetic field perpendicular to the Shastry-Sutherland plane. At fields above zero but below the critical field h_c, the upper and lower bands have nonzero Chern number. Panels f and g: Band diagram showing the chiral edge modes in the gap between triplon bands. Panels h through j: Theoretical prediction of thermal Hall conductivity. The component from the chiral edge modes should in principle give rise to a strong thermal Hall conductivity, since it is not washed out by the phonon thermal conductivity.

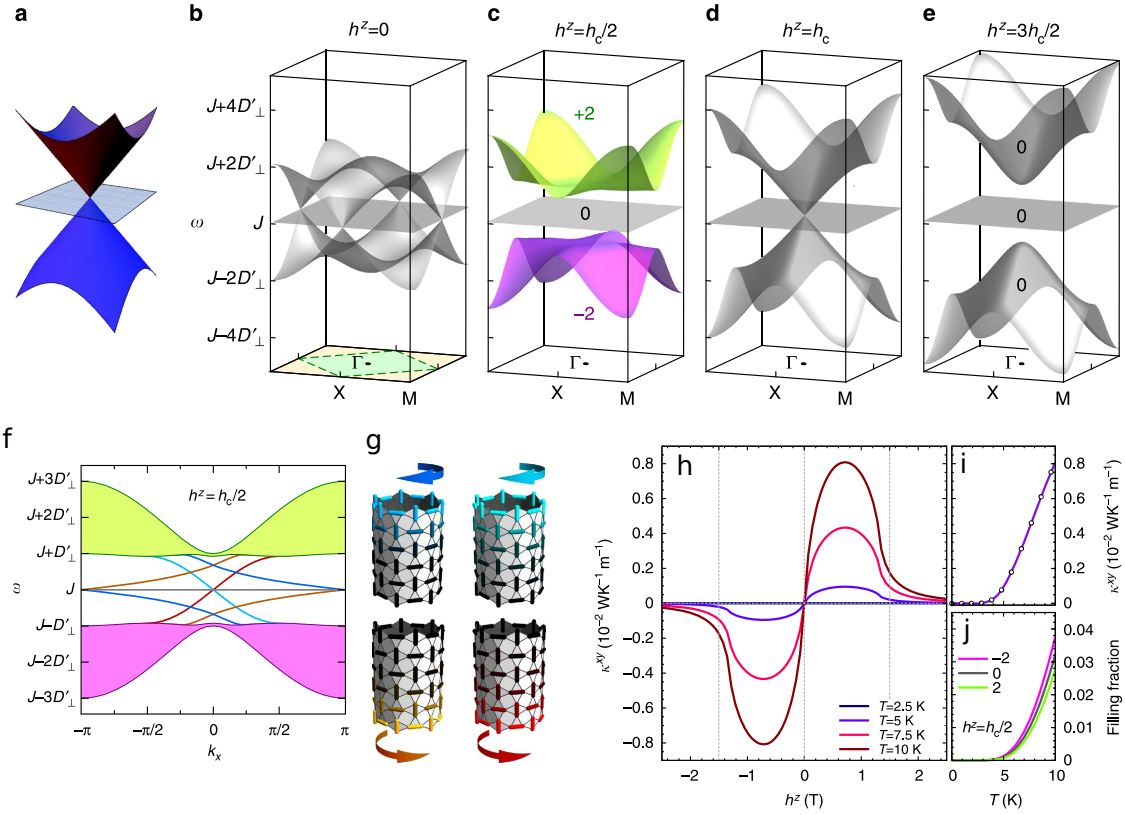

up between the upper and lower triplon bands, which have Chern numbers of 2 and -2 respectively, and the middle band which has trivial topology (Chern number 0). Then, at a critical field h_c, the gaps between the bands close again, opening up above this field to form three bands with trivial topology. As a consequence of the nontrivial topology of the triplon bands, there are 1-D edge states around the edge of the (2-D) Shastry-Sutherland planes. One important feature of these states is that they are chiral: they can only propagate around the edge of the lattice in one direction. Panel f in figure 3.7 shows these states spanning the gap between the bulk triplon bands. The energy of the bands is expressed in terms of the interdimer coupling J and the out of plane component of the interdimer DM interaction $D_\perp$. Each individual band has a group velocity which is either strictly negative or strictly positive. The observation of such an edge state would be compelling evidence for existence of topological triplon bands in SCBO.

The most experimentally relevant prediction made by these calculations, which ties it into the rest of this work, is the presence of a large thermal Hall conductivity. This is ultimately the result of the fact that wave packets in the Chern bands have net rotational motion [60], with bands of opposite Chern number rotating in opposite directions. For wave packets at the edge of the crystal, this results in unbalanced rotation and a net motion. The triplons with differing Chern numbers have energies which differ by approximately $2D_\perp$, and so those with Chern number -2 will be populated preferentially over those with Chern number 2. It should also be noted that since the triplons are bosons, and so do not form a Fermi pocket, and so will need to be thermally activated. Since the triplon bands do not carry any charge, the signature of this motion can only be found using the thermal Hall effect. Panel h of figure 3.7 shows the prediction for the thermal Hall conductivity. As the field is increased, the thermal Hall conductivity is expected to increase to a maximum at half of the critical field $h_c \approx 1.4$ T, then being reduced and heavily suppressed above h_c. Panel i of figure 3.7 shows the predicted temperature dependence of the thermal Hall conductivity at $h^z = h_c/2$, increasing dramatically above 5K. The role of the edge states is subtle: they

Figure 3.8: SCBO thermal Hall conductivity at 6K, measured in the Dynacool PPMS. There is no well defined thermal Hall effect observed. Other temperatures measured in the PPMS, as well as our Oxford dilution refrigerator, have borne the same result.

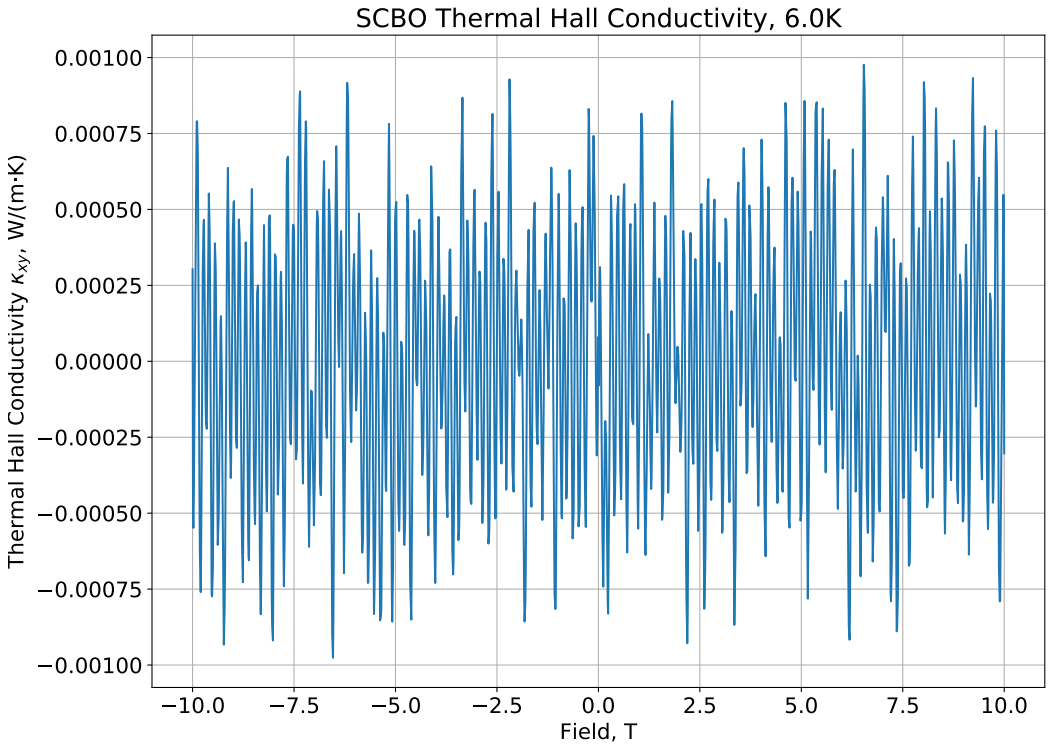

do not contribute directly to the thermal Hall conductivity since edge states of different chirality have the same energy and thus the same occupation, but they do preferentially conduct heat around the edge of the sample, thus populating bulk triplons in the bulk bands near the edge. Regardless, the predicted magnitude of the thermal Hall conductivity is quite large, comparable to that measured in the Bismuth samples discussed in the previous chapter at much higher temperature.

With this in mind, we set out to perform thermal Hall effect measurements on SCBO. Measurements were performed both using the STO capacitive thermometers described in the previous chapter and Cernox resistive thermometers. Both our Oxford dilution refrigerator and the Dynacool PPMS were used as well. After many months of attempts, no signature of the thermal Hall conductivity was found, from temperatures ranging from 0.1 K to 30K and in fields up to 8T. Figure 3.8 shows a representative thermal Hall conductivity trace consisting only of noise, two orders of magnitude below what was predicted by Romhányi et al. Measurements conducted by a group at the University of Edinburgh have corroborated this lack of apparent thermal Hall conductivity [61]. This would seem to cast doubt on the existence of topological triplon bands in SCBO. It is difficult to speculate on why this might be the case, but one potential issue stems from interlayer effects. The calculations in Romhányi et al. assume that the Shastry-Sutherland layers do not interact, but that their individual thermal Hall conductivities add together. However, there is experimental evidence that there is a coupling $J_{\mathrm{interlayer}}$ between the layers with a magnitude between 9% and 21% of the interdimer coupling [49] [62]. These interactions may be frustrated in a similar way to the interdimer coupling, but there could potentially be DM interactions between the planes as well. It is not obvious how these interactions could affect the creation of the Chern bands.

One might get the impression that the months spent trying to resolve the thermal Hall conductivity were a waste. This is far from the truth. As discussed in previous chapters, measurements of the thermal Hall conductivity necessarily require measuring the longitu-

dinal thermal conductivity as well. As it turns out, the thermal conductivity of SCBO has a rich structure below 1K. We will discuss these measurements in the next chapter.

3.3 Low Temperature Thermal Conductivity in SCBO

Although our original intention in making thermal measurements was to find the signature of the Chern bands using the thermal Hall effect, the more interesting results come from the thermal conductivity data taken at low temperatures. The data was originally taken at constant temperature as a function of applied magnetic field. Two datasets were collected: One from 6 K down to 2 K every 1 K taken using the Dynacool PPMS, and one from 1 K to 100 mK at least every 100 mK with denser curves at some particular temperature ranges, taken in our Oxford Dilution refrigerator. The sample used in the PPMS was approximately rectangular with total dimensions of 2.5 mm long by 0.85 mm wide by 0.2 mm thick. The longitudinal distance between the thermometers in the PPMS measurements was 0.75 mm. For the dilution refrigerator experiments, the sample was 3.1 mm long by 1.3 mm wide by 0.2 mm thick, with a longitudinal distance between the thermometers of 0.78 mm. The relatively small longitudinal distances were chosen since we were still trying to detect a thermal Hall signal as well as measure the thermal conductivity. The samples were oriented so that the magnetic field was applied along the c axis, i.e. perpendicular to the Shastry-Sutherland planes.

Earlier thermal conductivity measurements attempted to use STO capacitive thermometers, but since the interesting signal occurs primarily below 4 K, the unannealed thermometers were not suitable. Thus, a matched pair of bare chip Cernox thermometers was used instead. The detailed magnetoresistance of these thermometers was mapped in situ and all temperatures derived from this field calibration. For the PPMS data, a sine wave excitation of 0.1 mA and a period of 200 s was applied to the resistive heater. The relatively large excitation was once again used to give the best chance of finding a thermal Hall signal.

For the dilution fridge data, the same period was used, but the excitation used ranged from 58.57 μA at 1 K to 10 μA at 100 mK. The large range in excitations was necessary since the temperatures involved spanned an order of magnitude. Excitations were selected to ensure that the temperature difference between the thermometers was less than either 1% of the total temperature, or 10 mK if that did not provide enough sensitivity.

The thermal conductivity data found in these experiments is summarized in figure 3.9. The top panel shows the data taken in the PPMS. In this data, the application of the magnetic field appears to enhance the thermal conductivity, with the effect weakening as we cool down to 2 K. The bottom panel shows the data taken in the dilution fridge. Here, it appears that the magnetic field suppresses the thermal conductivity at 1K, but when the temperature is lowered to around 450 mK, the dependence begins to flip around. At lower temperatures, the thermal conductivity is instead enhanced by magnetic field. The same dataset is plotted in figure 3.10, this time with cuts taken at constant magnetic field as a function of temperature. Separate data runs where the temperature was ramped at a constant magnetic field were taken which reproduce the general trends of this data, however they suffer from a great deal of noise due to the massively different excitations required at each temperature. Figure 3.10 makes the "crossover" between magnetic field suppression and enhancement of the thermal conductivity at around 450 mK more clear. This crossover is not sharp in the sense that the conductivity traces do not converge to a point. This would correspond to the thermal conductivity being independent of magnetic field at some temperature, instead we see that some traces show enhancement and suppression at different values of the applied field. Not included in this plot is the data taken in the PPMS. In that dataset, we can see that the value of the thermal conductivity taken at 2K is lower than that taken at 1K in the dilution fridge. It is unclear if this is a true effect or if it is an error introduced by uncertainty in the sample geometry. Previous measurements of the thermal conductivity at higher temperatures have shown that the temperature dependence at higher temperatures is indeed not monotonic [52], but it is difficult to do an experiment in our sys-

Figure 3.9: Low Temperature thermal conductivity of Strontium Copper Borate. Each curve is taken at a constant temperature. Top: Data taken in the Dynacool PPMS, from 6 K to 2 K. The applied field enhances the thermal conductivity. Bottom: Data taken in the Oxford dilution refrigerator, from 1 K down to 100 mK. Field suppresses the thermal conductivity down to about 450 mK, at which point the dependence flips around again.

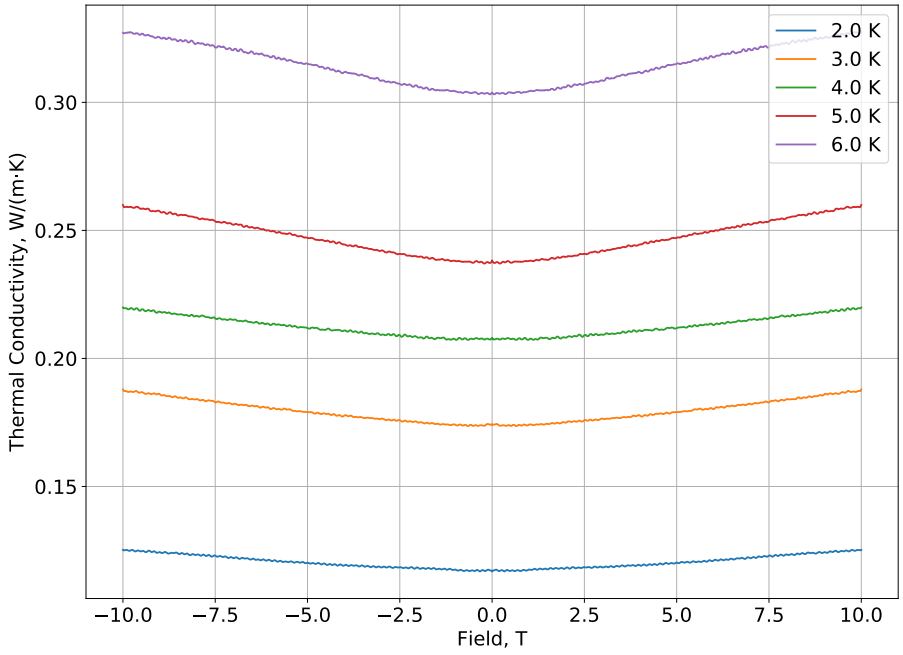

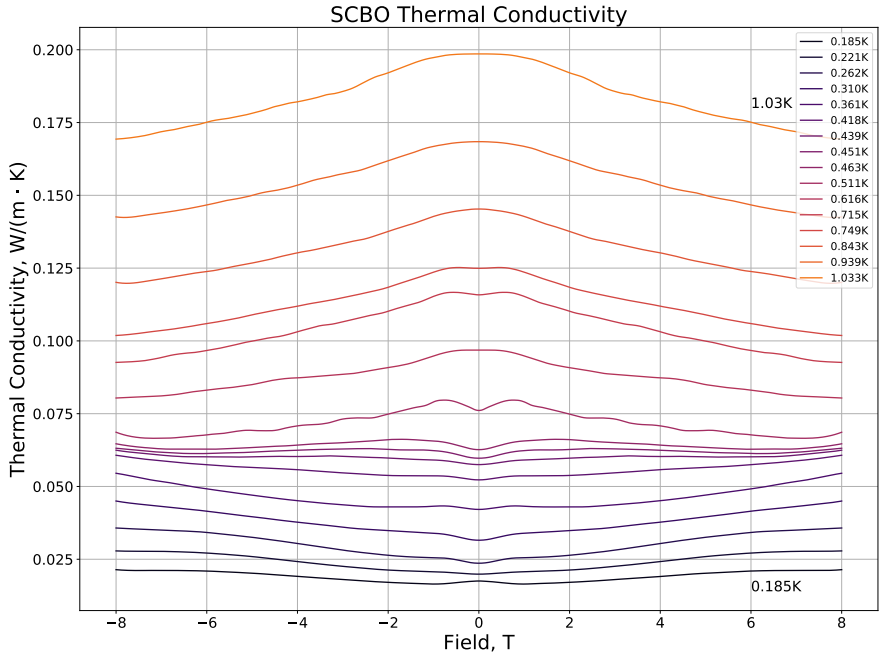

Figure 3.10: The same data set as 3.9, now plotted with temperature on the x axis instead of magnetic field. Each trace is a particular cut through the data at a constant field. The crossover between suppression and enhancement of the thermal conductivity is evident at around 450 mK.

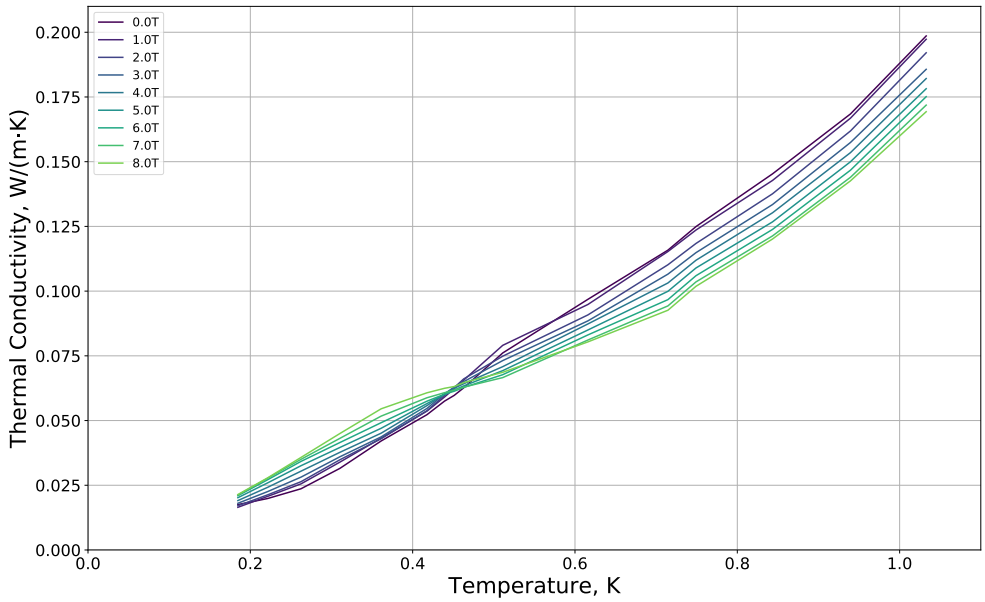

tems which would show this conclusively. The PPMS cannot stabilize temperature lower than 2 K due to the custom puck required to do the measurement, and the dilution fridge cannot control temperature in the range between 1 K and 2 K due to competition between the dilution unit and the pulse tube stage. Thus, for the remainder of this section we will focus on the dilution fridge data, which shows a clear inversion of the field dependence.

The presence of a field dependant thermal conductivity in this temperature range is very puzzling. Certainly we can imagine that the triplons should couple to a magnetic field, but since the gap between the triplons and the singlet ground state has been observed to be about 3 meV (see figure 3.5), corresponding to about 35K, we should expect that the occupation of triplons should be extremely small. In any event, since the triplons have very flat dispersion, they should not contribute much to the thermal conductivity even when they are occupied. The phonons themselves should also not couple to a magnetic field

directly. However, it has been noted in previous measurements of the thermal conductivity at higher temperature [52] as well as the heat capacity [51] were significantly influenced by resonant scattering of the phonons by the triplon states. This resonant scattering is observed to significantly suppress the thermal conductivity by damping the phonons. As discussed above, this resonant scattering is also responsible for an anomaly in the thermal conductivity around 7.5 K. This mechanism could certainly couple the thermal conductivity to the magnetic field, but it appears to do so in the wrong temperature range. The effect of this anomaly is already small at 2.5 K, but the thermal conductivity is still being affected by the field down to 200 mK. In that section we also noted that the DM interaction could mix the singlet and triplet states since it violated conservation of s^z. The signature of resonant scattering by these states was present in the heat capacity measurement at lower temperatures, but only in fields above 10 T. In the thermal conductivity measurement, it appears the bulk of the change in κ_{xx} occurs below 5 T. Heat capacity measurements at lower temperatures would certainly help to disambiguate this phenomena, but from the data presented it seems like the field scale is wrong for this to be a factor.

Although we no not have a good theoretical explanation for the changing thermal conductivity in this temperature range, we still wish to find some way to quantify the changes. Qualitatively, most of the curves appear to start at some value and then asymptotically move towards some other value at high fields, lower in some cases and higher in others. In order to structure our thinking, we have fit these curves to a function which has this qualitative form:

$$\kappa_{xx}(h) = a + \frac{c}{1 + (h/b)^2}$$

where h is the applied field, and a, b, and c are the fit parameters. These parameters have straightforward interpretations: a is the infinite field thermal conductivity, c is the difference between the zero field and infinite field conductivities (so that $\kappa_{xx}(0) = a + c$), and b is a "field scale" which characterizes the width of the transition between the zero and infinite field values. Thus, when the field is multiple times higher than this field scale,

Figure 3.11: Example fits of the Strontium Copper Borate thermal conductivity data. Above and below the crossover region, the ansatz fits quite well. In the crossover region, however, the thermal conductivity appears to have more structure than what is captured by the ansatz.

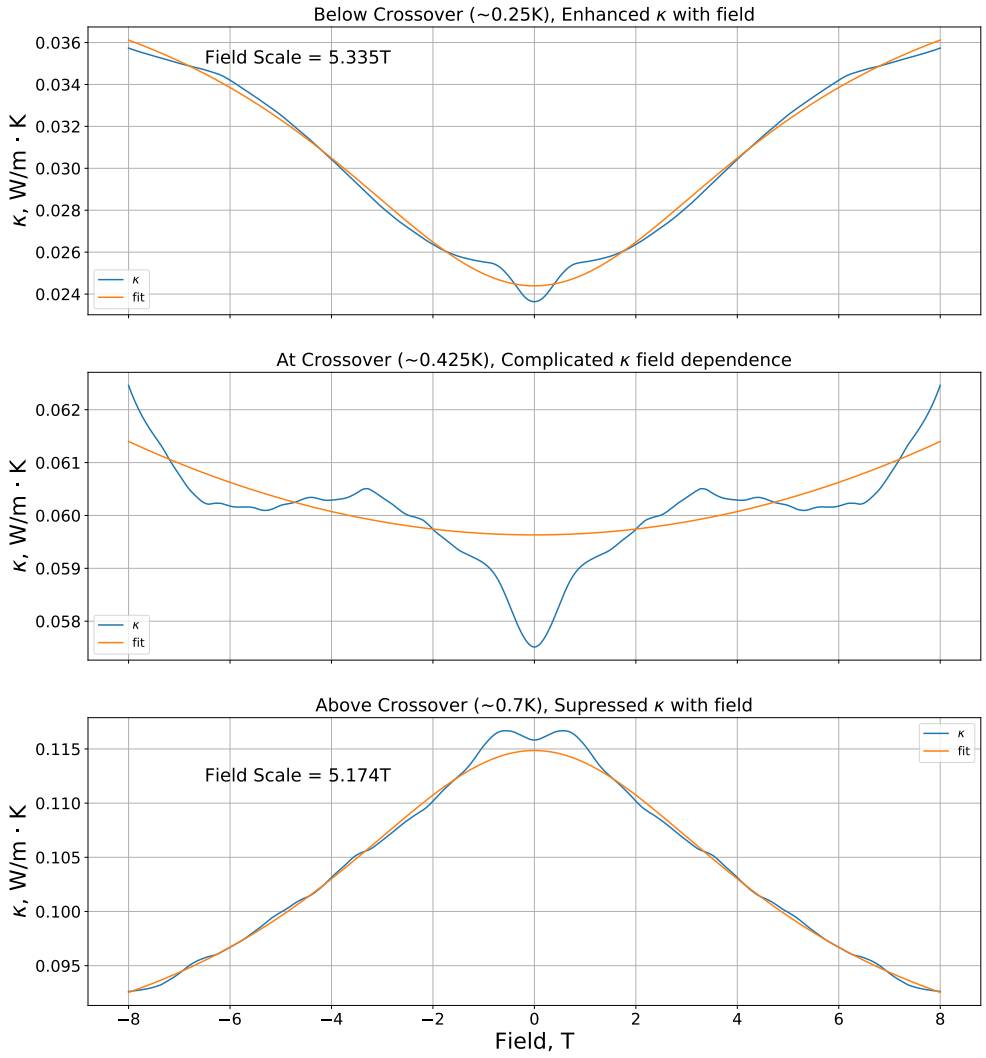

we expect the thermal conductivity to be more or less constant. Figure 3.11 shows a few example fits. For traces taken above and below the crossover region, the fit appears to work quite well, independent of the sign of c. For the traces in the transition region, however, the fits do not capture all of the structure of the thermal conductivity. The derivative of κ_{xx} with respect to the field appears to oscillate a few times, and it is unclear if it has an infinite field asymptote. A summary of the fitted parameters is shown in figure 3.12. Both plots have error bars extracted from the fits plotted in red. For the traces in the crossover region, where the fit is not adequate, the error bars are quite large. However, above and below it, they are relatively small. The top panel shows the extracted field scale. For all the plots outside the crossover, the field scale is more or less independent of temperature, with an average of 5.19 T. Since we are able to apply fields of up to 8 T in the Oxford dilution fridge, we can be confident we have enough field to capture this feature. The bottom panels shows the zero field ($a + c$) as well as the infinite field (a) thermal conductivity.

Very recently, a similar crossover effect has been observed in a layered magnet $CrCl_3$, studied for its similarity to the spin liquid candidate α-$RuCl_3$ [63]. In that material, the crossover from enhancement to suppression of the thermal conductivity in field is explained by a transition from coherent conduction by magnons to scattering of phonons by magnons being the dominant factor affecting the thermal conductivity. There is good reason to suspect resonant scattering by triplons is playing an important role at higher temperatures in SCBO, as discussed above. However, the fact that the magnetoconductivity persists down to 200 mK presents a problem for applying this explanation to SCBO. As far as scattering by the triplons are concerned, they provide a schematic model for thermal conductivity in a system with phonons scattered by magnons:

$$\kappa^{-1}(H,T) = \kappa_{\mathrm{ph}}^{-1}(T)[1 + \lambda(H,T)n_{\mathrm{mag}}(H,T)]$$

where κ is the total thermal conductivity, κ_{ph} is the field independent phonon component,

n_{mag} is the population of magnons, and λ characterizes the strength of the coupling. The quantity λn_{mag} is effectively ratio between the scattering rates of phonons between the lattice and the magnons. However, at 500 mK, based on Bose-Einstein statistics, the occupation of triplons should be less than one in ten thousand *per mole of dimers*! In order for resonant scattering to explain the thermal magnetoconductivity in this range, we would need λ to be so large as to be completely unphysical.

One other curious feature is the appearance of a very small thermal Hall conductivity at around 500 mK, shown in figure 3.13. This only occurs at this specific temperature, and it is barely visible with the sensitivity of the Cernox thermometers. At the field with the strongest κ_{xy}, the thermal Hall angle is about $\tan\theta_H = 0.013$, which is relatively large compared to the other spin systems listed in table 1.1. This is just above the temperature where the field dependence of the thermal conductivity flips over. Clearly, it is not like the thermal Hall signal predicted to arise as a result of the Chern bands, as it does not get stronger with higher temperature. It is hard to imagine this thermal Hall conductivity coming from the triplons directly, since they should be frozen out at this temperature. Instead, it appears to be specific to the crossover.

One potentially interesting question to consider is how this thermal conductivity signal might be connected to another phenomena observed in SCBO at temperatures below 1 K: the formation of spin superlattices. When large magnetic fields are applied to SCBO, the energy of the triplet states with s^z aligned with the applied field can be lowered to the point that they become populated, and arrange themselves into a lattice structure which is some multiple of the base lattice, hence the name "superlattice". The superlattices are labeled by what fraction of the total possible magnetization they have. Figure 3.14 shows the structure of the 1/8 superlattice, as well as its experimental signature in magnetic susceptibility measurements at 22T [64]. In higher fields, experiments measuring magnetostriction [65] and magnetization [66] has found evidence for 2/15, 1/4, 1/3, 2/5, and 1/2 superlattices. All of these occur at magnetic fields much higher than what we have measured, but all require

Figure 3.12: Top: Extracted field scale vs. temperature. The red lines are the error bars from the fit. Note that the field scale is more or less constant where the fit is valid. Where it is not valid, the error bars extend beyond the scale of the plot. I have kept them here to demarcate the crossover region. Bottom: Zero field (blue) and infinite field (green) thermal conductivities extracted from the fits. Once again the error bars are red.

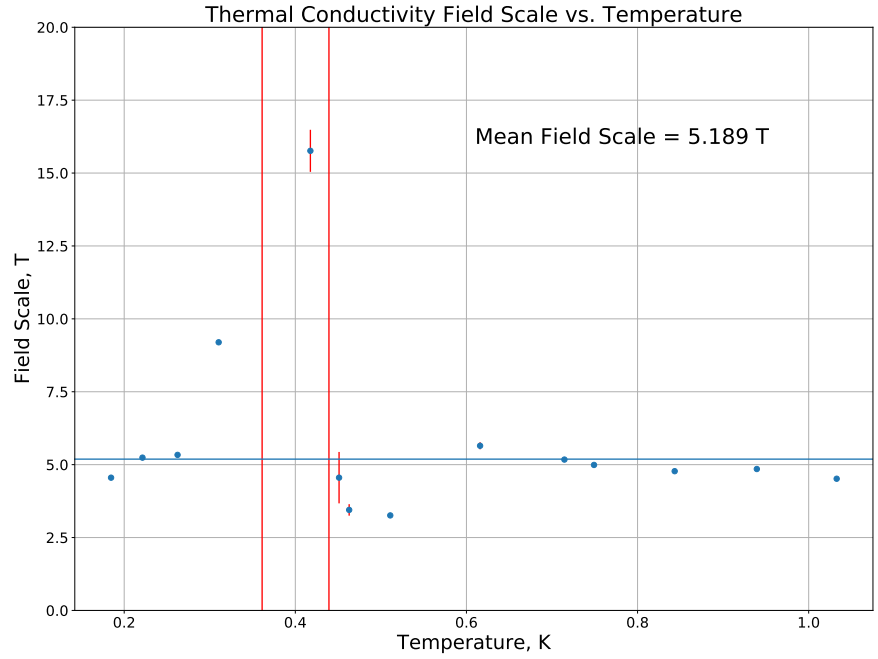

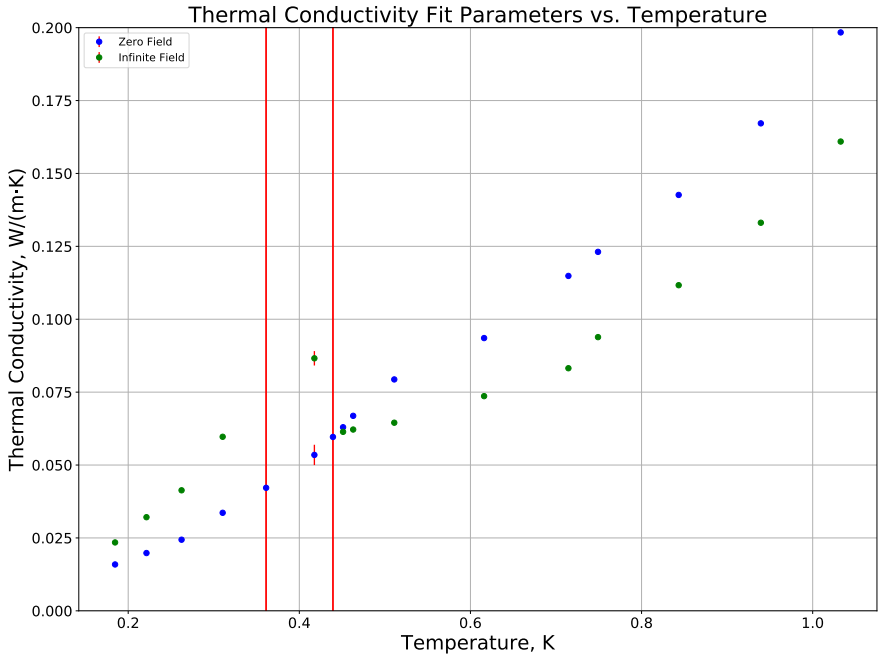

Figure 3.13: A very small thermal Hall conductivity, barely above the noise level, observed at a temperature of about 500 mK. This is just above the crossover temperature.

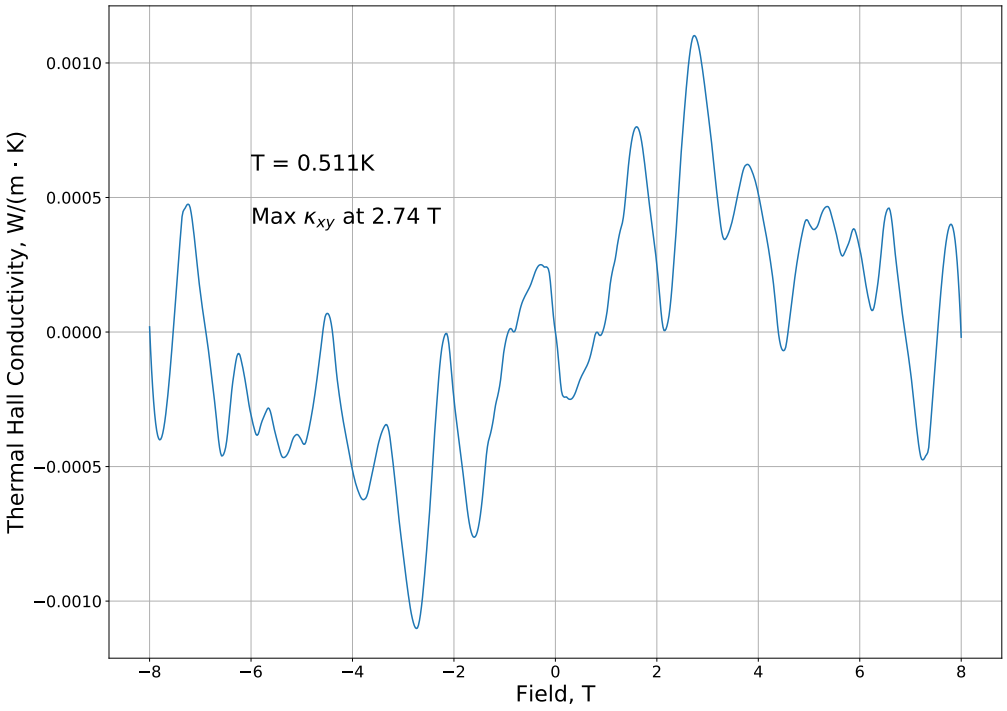

temperature below 1 K. However, when a pressure of 2.2 GPa is applied to the crystal, a new superlattice attributed to a 1/20 superlattice occurs just above 5 T. This is within the range of the thermal conductivity experiments described above, and corresponds to the field scale we observed using the ansatz fits. Clearly the 1/20 superlattice is not forming in our experiments, which were conducted in vacuum. However, we can speculate that the field dependent thermal conductivity is related somehow to this ordering, or perhaps to whatever is suppressing it at ambient pressure. The fact that the specific field dependence of κ_{xx} changes with temperature may be a sign that there are competing phases involved, perhaps other, larger superlattices. Unfortunately, it appears more measurements will need to be conducted in order to say for sure if this is the case.

Figure 3.14: Spin Superlattices in SCBO. Top: Schematic of the 1/8 superlattice observed in SCBO at ambient pressure, reproduced from [67]. The lattice has one eighth of the total possible magnetization, with an arrangement which enlarges the unit cell of the layer, hence the term "superlattice". Bottom: experimental signature of the formation of superlattices in SCBO from magnetic susceptibility measurements, reproduced from [64]. A background has been subtracted to highlight the superlattice feature. Panel a shows measurements taken at ambient pressure. The 1/8 superlattice is formed at around 22 T. Panel b shows measurements taken at 2.2 GPa. In this case, a new superlattice forms above 5 T. In both cases, the superlattices only become clearly defined below 1 K.

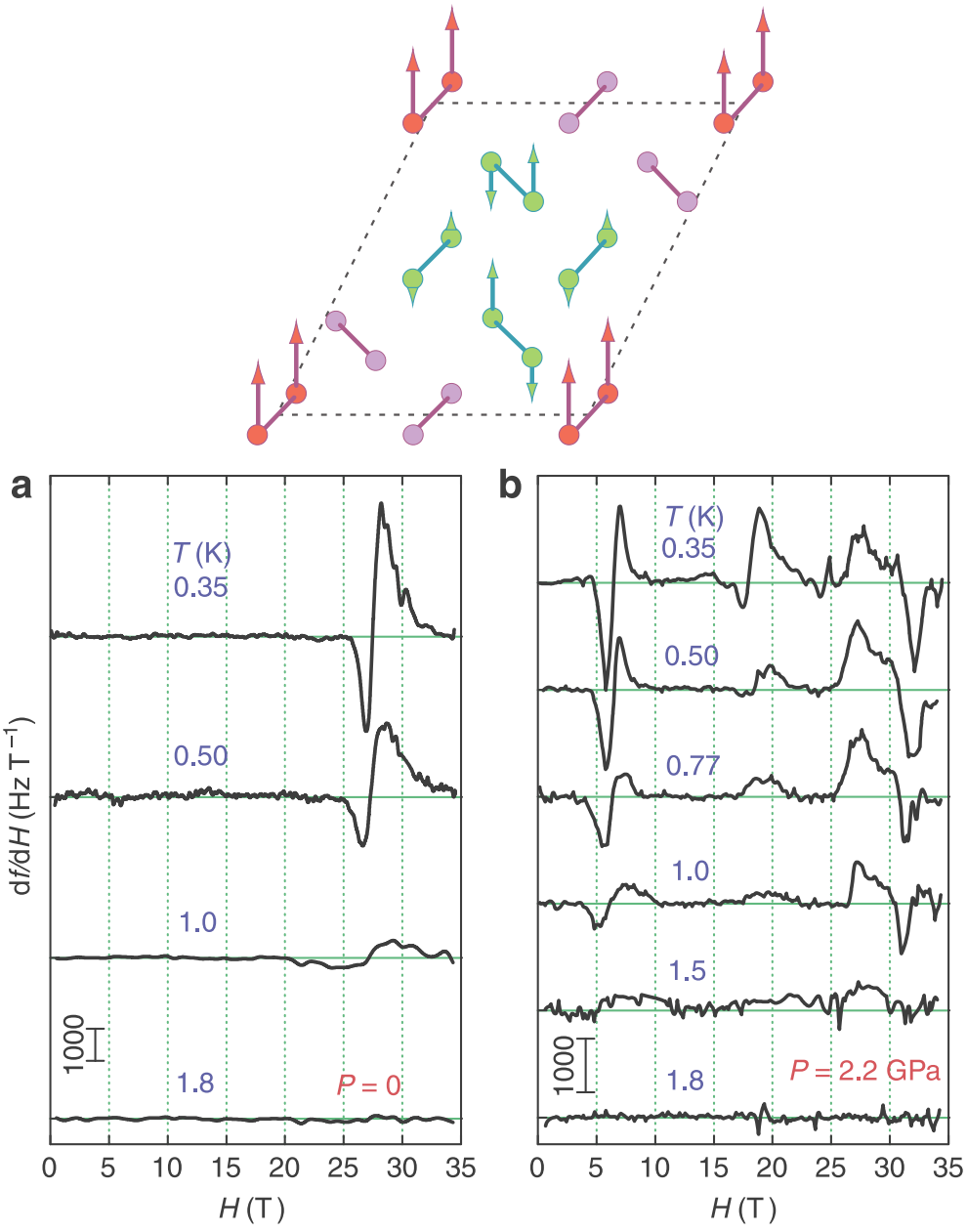

CHAPTER 4

Conclusion

Thermal measurements are an important tool for studying new materials and identifying novel physics in condensed matter systems. In a sense, they are the most general experimental methods available to a condensed matter experimentalist: any excitation in a solid will carry energy, and thus heat. This makes them particularly applicable to studying systems with novel excitations that do not carry charge. Such measurements can be quite challenging to make, however. They require accurate and precise readings of the temperature at multiple points on a crystal, which are often quite small, only a few millimeters in any direction. These thermometers must be compatible with the cryogenic environment where the measurement takes place, and may also need to be compatible with intense magnetic fields.

This is especially important when making thermal Hall effect measurements, the thermal analogue of the Hall effect. This effect is often minute, rarely more than 1% of the total thermal conductivity. It also often requires making measurements in magnetic fields of a few Tesla or more. These fields can interfere with standard methods of thermometry relying on resistive thermometers by way of their magnetoresistance. In order to eliminate the systematic issues with these devices, we have exploited the strongly temperature dependent dielectric permittivity of strontium titanate. This material is not itself a ferroelectric, but sits close to a quantum phase transition to a ferroelectric state. This causes its permittivity to increase rapidly until reaching a maximum a few Kelvin above absolute zero. By making

small capacitors using this material as a dielectric, we can use this fact to measure temperature with great precision in a way that is not systematically affected by a magnetic field. This observation on its own opens up new possibilities for making thermal Hall effect measurements in strong magnetic fields, but since the permittivity saturates below a few Kelvin, the sensitivity of these devices rapidly degrades in this range. However, it has been noted that annealing strontium titanate in an oxygen-18 atmosphere can tune the properties of this material close to this quantum critical point, even making it ferroelectric if enough is incorporated. By moving strontium titanate close to this quantum phase transition without going over, the permittivity can be made to keep increasing down to temperatures below 1 Kelvin, where the magnetoresistance issues of conventional thermometers are most severe.

In order to test these capacitive thermometers, thermal Hall effect measurements were carried out on single crystalline bismuth. Bismuth is one of the best known semimetals, a material which hosts both electrons and holes, with a relatively low carrier density but high mobility. It is also well known for having "Dirac-like" bands, with carriers that have linear dispersion similar to a relativistic particle. These properties make it an important system for benchmarking new experimental techniques in condensed matter physics. Despite being an "old material", one which has been studied experimentally for over a century, thermal Hall effect measurements had only recently been performed on it up to 3 T. With the strontium titanate microthermometers, we were able to conduct measurements up to 10 T and at temperatures down to 40 K. A large thermal Hall coefficient is measured in this system, indicative of high mobility carriers. Additionally, the overall field dependence displays a $1/H$ drop off far below the quantum limit, which can be traced to the presence of both electrons and holes. The strontium titanate microthermometers allow us to continue to observe these properties in the intense magnetic field.

Another important application of these thermometry techniques is towards making measurements of frustrated magnets. These are systems where the geometry of the lattice interferes with magnetic ordering, resulting in a variety of new magnetic phases such as spin

ices and quantum spin liquids. These systems have generated quite a bit of theoretical interest in the past decade, but they are difficult to study experimentally since they often have itinerant excitations which do not carry charge. This makes thermal transport measurements such as the thermal Hall effect all the more important for studying them. In this work we discuss our measurements on strontium copper borate, in which pairs of spin-1/2 sites are paired up in dimers with a ground state made up of a lattice of singlets. The magnetic excitations of this system are the mobile triplet states, called triplons. It has been predicted that these triplet bands could have non-trivial topology, making strontium copper borate a bosonic topological insulator, and resulting in a specific thermal Hall effect signal. Experimental measurements in this system fail to find this signal, casting doubt on this theory. However, we observe magnetic field dependent longitudinal thermal conductivity at temperatures below 1 K, where the triplet excitations should be frozen out. There may be some relation to another phenomena found in this material in this temperature range: the formation of spin superlattices, states where spins form ordered arrangements larger than the base unit cell of the material.

Of course, the work presented here opens up some new lines of research. With the feasibility of the capacitive thermometers established for temperatures above 10 K, we now seek to extend their usefulness to lower temperature by way of oxygen-18 substitution. This is regime where standard resistive thermometers have the most issue with magnetoresistance. More iteration is required to get the annealing conditions correct to make the most effective thermometers, and it constitutes its own research project. Secondly, there is the origin of the thermal magnetoconductivity in strontium copper borate. It is very puzzling how the thermal conductivity could change so strongly at such a low temperature, when the population of triplons should be exceptionally low. How, if at all, it is related to the formation of spin superlattices in the same temperature range remains an open question. This may require thermal measurements at higher fields to see if the thermal conductivity does indeed remain stable as we have assumed in our descriptive model. In the past few months,

we have taken delivery of a 14 T magnet for the Oxford dilution fridge system where the measurements on SCBO were performed. Thus, we can try to make these measurements at higher fields. However, the magnetoresistance of the thermometers will only become more of an issue in these fields. Thus, these two lines of research are intimately connected. More generally speaking, as we seek to discover new magnetic phases in frustrated magnet systems, more and more accurate thermal measurements will be required at lower and lower temperatures. This will require new advances in thermometry, to which I hope I have made a meaningful contribution through this research.

APPENDIX A

Python Source Code for Finite Element Simulations of the Thermal Hall Effect

The following Python source code uses Fenics to do the finite element computations described in chapter 1. It will output the plots in the text as pdf files.

```
from fenics import *
from mshr import *
import numpy as np
import matplotlib.pyplot as plt
import matplotlib

# Mesh
asp_ratio = 1.6
domain = Rectangle(Point(0.0, 0.0), Point(asp_ratio, 1.0))
mesh = generate_mesh(domain, 128)
V = FunctionSpace(mesh, 'P', 1)

# Dirichlet BC (Cold Finger)
u_D = Constant(0.0)

def boundary_D(x, on_boundary):
    return on_boundary and ((x[0] <= asp_ratio*x[1])
                        and (x[0] <= asp_ratio*(1-x[1])))

bc = DirichletBC(V, u_D, boundary_D)

# Neumann BC (Heater, Insulated Edges)
g = Expression(
        'x[0] >= x[1]*{0} && x[0] >= (1-x[1])*{0} ? -1 : 0'
        .format(asp_ratio), degree=1)
```

```
thetas = np.pi*np.array([-1/6, -1/12, 0, 1/12,
                         1/6, 1/4, 1/3, 5/12])
xs = np.linspace(0,1.6,161)
ys = np.linspace(0,1.0,101)

us = np.zeros((thetas.size, xs.size, ys.size))

for ii, theta_hall in enumerate(thetas):

    # Thermal Hall Conductivity
    # C = as_matrix(((1, np.tan(theta_hall)),
    #                (-np.tan(theta_hall), 1)))
    C = as_matrix(
        ((np.cos(theta_hall), np.sin(theta_hall)),
         (-np.sin(theta_hall), np.cos(theta_hall))))

    # Weak Problem
    u = TrialFunction(V)
    v = TestFunction(V)

    a = dot(C*grad(u), grad(v))*dx
    L = -g*v*ds

    # Compute solution
    u = Function(V)
    solve(a == L, u, bc)

    us[ii] = np.array([[u(x, y) for x in xs] for y in ys]).T

font = {'size'   : 16}
matplotlib.rc('font', **font)

f, axarr = plt.subplots(4,2, sharex='col',
                             sharey='row',
                             figsize=(9,12),
                             subplot_kw={'aspect':1})
theta_names = ['-$\\pi$/6', '-$\\pi$/12', '0',
       '$\\pi$/12', '$\\pi$/6', '$\\pi$/4',
               '$\\pi$/3', '5$\\pi$/12']
levels = np.linspace(0, np.max(us), 24)
for theta, u, ax in zip(theta_names, us, axarr.flatten()):
    ax.contour(xs, ys, u.T, cmap='plasma', levels=levels)
    ax.set_title('$\\theta_H$ = {}'.format(theta))

f.savefig('thall_isotherm.pdf')
```

```
font = {'size'   : 14}
matplotlib.rc('font', **font)

f, (ax1, ax2) = plt.subplots(2, 1, figsize=(9,12))

for theta, u in zip(theta_names, us):
    diff = u[:,-1] - u[:,0]
    ax1.plot(xs, diff, label=theta)

ax1.set_title('Temperature Difference Profile')
ax1.set_xlabel('$x$, arb. units')
ax1.set_ylabel('$\Delta T$, arb. units')
ax1.grid()
ax1.legend()

ax2.plot(thetas_full, us_full[:,-1,-1] - us_full[:,-1,0])

ax2.set_title('Transverse Temperature Difference')
ax2.set_xlabel('Thermal Hall Angle $\\theta_H$, radians')
ax2.set_ylabel('$\Delta T$, arb. units')
ax2.grid()

f.savefig('thall_profile.pdf')
```

APPENDIX B

Operation of the Denton Evaporator

B.1 Preparing the Chamber

1. The bell jar should have a rough vacuum when it is not in use. Make sure all the valves are closed, and then pull the lever labeled "Chamber Vent" to open the bell jar to air.

2. Once the chamber has vented, carefully lift the bell jar off the platform and place it on the nearby lab bench.

3. Check the underside of the plate to see if the aluminum foil has gold peeling off of it. If so, it will not be possible to mount the samples firmly to the plate. Unscrew the plate from the three brackets with a flathead screwdriver and replace the aluminium foil.

4. Mount your sample on the plate above the filament electrodes. Typically when making gold films for capacitive cantilevers, we stick them to a strip from a post-it note which has been fixed to a glass slide with PTFE tape. This slide can be attached to the plate with double-sided tape. Mount it directly over the gold filament (in the front of the chamber).

5. Get a tungsten filament out of the top drawer of the file cabinet next to the evaporator. Using a pair of needle-nose pliers, grip one end of the filament and twist it to separate

the three wires. With a side cutter, cut two of the wires completely off from the base of the corkscrew portion. Be careful, the cut ends of the wires will be extremely sharp. Do the same for the other end of the filament. Then, trim the remaining wire to length so that it will fit in the electrode.

6. Cut a piece of the gold wire which is $\sim$ 5 mm longer than the corkscrew section of the filament. Insert the wire into the corkscrew, and then use a pair of needle-nose pliers to bend each end of the gold wire such that it will not fall out.

7. Insert the loaded tungsten filament into the electrodes. Use a hex wrench to adjust the gap between the jaws of the electrode to get good mechanical contact.

8. Take a multimeter and check that the two electrodes are shorted together. Move the filament selector to the "Chromium" setting so that they are not connected through the power supply. Move the selector back once you have finished checking the electrode.

9. Check that the electrodes are not shorted to the filament shield. If they are, it is likely the short is near the ceramic spacer which connects the shield to the electrode. Kapton take can be used to interrupt any shorts in this area. If the spacer is cracked, replace it with a new one stored in the top drawer of the filing cabinet.

10. Check that the electrodes are not shorted to the top plate. The position of top plate can be adjusted by loosening the screws around on the brackets holding it up and repositioning it.

11. Clean the rim of the bell jar as well as its mating surface with isopropyl alcohol. Replace the bell jar.

B.2 Pumping the Chamber to Low Vacuum

1. Flip the "Main Power" switch.

2. Flip the "Mech. Pump" switch to turn on the rough pump.

3. Turn the knob under the thermocouple gauge to the "Back" setting, and flip the switch next to it to turn on the gauge. The reading will be very noisy at first but will get cleaner once the foreline pumps out. It should reach 50 millitorr in about 30 seconds.

4. Open the backing valve underneath the control console. This will rough out the diffusion pump.

5. Open the cooling water valves to the left of the evaporator. There are four valves to open in total: One each above and below the split between the evaporator and the resistive magnet on both the input and return lines. Open all four. Then, twist the knob labeled "Diff. Water" less than half a turn, so that the arrow is pointing upwards. You will not see any appreciable flow on the flow gauge.

6. Once the foreline pressure reads below 100 millitorr, turn on the diffusion pump by flipping the "Diff. Pump" switch. Wait about 30 minutes for the diffusion pump to come up to temperature. The manual recommends you adjust the flow of the cooling water so that the exit temperature is about 100° F, in practice it seems difficult to get above 80°.

7. Add liquid nitrogen to the cold trap. This is optional, but it greatly enhances the vacuum one can achieve with this system. The input funnel is on the left side of the evaporator. Once the cold trap is full, liquid nitrogen will start to bubble out of the opening visible when looking through the slit for the main valve lever. Once nitrogen has been added, be sure to add more every two to three hours if you continue running that long.

8. Make sure the bell jar is on the base plate.

9. Close the backing valve underneath the control console, and open the roughing valve. Only one of these valves should be open at any time!

10. Move the thermocouple gauge selector to the "B. Jar" position. Once the reading is below 100 to 150 millitorr, close the roughing valve and open backing valve.

11. Open the main valve by lifting the lever on the left side of the control console.

12. Move the thermocouple gauge selector back to the "Back" position. It should be at the bottom end of its range.

13. Move the discharge gauge range selector from the "Off" position to the "Zero" position. Let it warm up for a few minutes, and then adjust the zero knob until the needle reads zero.

14. Turn the nob to the "10^{-4}" range and push the "Vacuum Read" button. If the needle reads below one, switch to the next lowest range.

B.3 Evaporating

1. Turn on the thickness monitor, if you are using it.

2. Move the filament selector to the "Gold" position.

3. Make sure the pressure is in the "10^{-6}" range or lower on the discharge gauge readout.

4. Make sure the "Filament/Glow Selector" switch is in the "Filament" position.

5. Move the "Filament Adjust" knob in the center of the control console is at zero (all the way to the counter-clockwise).

6. Flip the “Filament Power” switch.

7. Slowly increase the power using the “Filament Adjust” knob. Usually for gold I start with 20 amps on the “Filament Current” meter until the filament starts to glow red, after which I slowly increase to 35 amps. For thick gold coatings I simply wait until there is visible gold on the inside of the bell jar. If you want a particular thickness, adjust the current to get your desired deposition rate. Monitor the pressure on the discharge gauge, making sure it stays below 1×10^{-5} torr. The pressure may increase initially as the filament outgasses, but should decrease after about 30 seconds. For gold, the process should take only a few minutes in total.

8. Once the desired thickness has been reached, turn the “Filament Adjust” knob all the way counter-clockwise and turn the “Filament Power” switch off.

B.4 Venting and Resetting the Chamber

1. Turn off the discharge gauge by moving the knob to the “Off” position.

2. Close the main valve by moving the lever down.

3. Open the chamber vent valve. Monitor the foreline pressure (“Back” setting below the thermocouple gauge reading) to make sure it is not increasing.

4. Remove the bell jar.

5. At this point, the chamber can be reset as described in part B.1, if you are going to do additional evaporation.

6. Once the chamber is prepared and the bell jar replaced, check that the vent levers are closed.

7. Close the backing valve and open the roughing valve.

8. Wait for the pressure on the “B. Jar” thermocouple to reach less than 100 to 150 millitorr.

9. Close the roughing valve, and open the backing valve.

10. If you will evaporate again, open the main valve again and turn on the discharge gauge again as described in part B.2.

B.5 Shutting the System Down

1. The bell jar should be roughed out at this point. If not, rough pump it as described in part B.4.

2. Close the main valve, if it is open.

3. Turn off the diffusion pump. Allow 20 minutes for it to cool down.

4. Close the backing valve.

5. Turn off the mechanical pump. Open the “M. P. Vent” lever to vent the foreline.

6. Turn off the main power.

7. Close all the valves for the diffusion pump cooling water (four on the wall, one on the center of the control console).

8. Ensure all the vacuum valves (main, backing, and roughing) are closed.

APPENDIX C

Operation of the Oxygen-18 Annealing System

C.1 Opening and Loading the Tube

1. If the tube is in vacuum, open V1 and then slowly open V3 while monitoring the pressure on P1. If air is let in too fast, the alumina spacers will be blown to the end of the tube. Afterwards, close V1 and V3.

2. If the tube still has oxygen-18 gas inside, collect the gas in the cold trap using the instructions in section C.5. The open the tube as described above.

3. Using a hex wrench, remove the flange on the right side of the tube. This side has a flexible tube to allow the flange to be moved away.

4. Use the metal hook to extract the alumina spacers and sample boats.

5. Place the new samples to be annealed in the sample boats.

6. Replace the alumina spacers and sample boats, using the metal hook. Place two spacers flush with the left edge of the furnace, then the samples, then two spacers flush with the right edge of the furnace.

7. Replace the flange on the right side of the tube. Tighten each bolt a little bit before moving to the next one in sequence, rather than tightening each one all the way down at once, to ensure a uniform seal.

Figure C.1: Strontium Titanate Annealing System

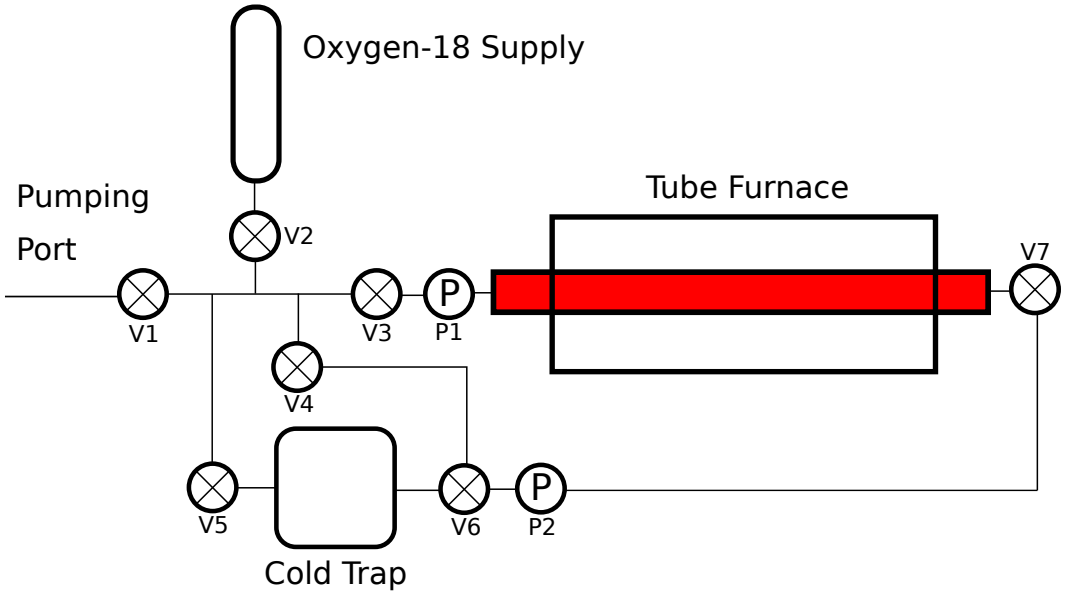

8. Connect the pump station to the pumping port with a KF-25 clamp. Turn on the rough pump only. Open V1.

9. Very slowly open V3. Monitor P1 to see when the pressure starts to drop. If the valve is opened too fast, the alumina spacers will be pulled across the tube, and the tube will need to be opened again to be reset.

10. Once V3 is completely open and P1 is at its lowest reading, turn on the turbo pump to finish evacuating the tube.

11. Once you are satisfied with the pressure reading on the pump station, close V1 and V3, shut down the pump station, and disconnect it from the pumping port.

C.2 Introducing the Oxygen-18 Gas from the Cylinder

1. Using the Gay-Lussac Law

$$\frac{P_1}{T_1} = \frac{P_2}{T_2}$$

   estimate the pressure needed in the tube at room temperature to get the desired pressure at the annealing temperature. This will underestimate the pressure at the annealing temperature since the ends of the tube will not be heated.

2. Open the valve on the oxygen-18 cylinder. The pressure in a new cylinder is relatively low, slightly above atmospheric pressure.

3. Open V2 to introduce oxygen-18 into the gas lines, then close V2.

4. Slowly open V3 to introduce oxygen-18 into the tube. As discussed above, the valve needs to be opened very carefully in order to avoid blowing away the alumina spacers. Monitor the pressure on P1.

5. If more pressure is needed, close V3, then repeat from step 3 until the desired pressure is reached.

6. Close V2, V3, and the valve on the oxygen-18 cylinder.

C.3 Introducing the Oxygen-18 Gas from the Cold Trap

1. Make sure the cold trap is warm. If it has recently had liquid nitrogen in it, wait for it to warm up.

2. As in section C.2, calculate how much gas you require in the tube.

3. Introduce oxygen-18 gas into the lines by opening V5, then closing it.

4. Slowly open V3 to introduce oxygen-18 into the tube. As discussed above, the valve needs to be opened very carefully in order to avoid blowing away the alumina spacer. Monitor the pressure on P1.

5. If more pressure is needed, close V3, the repeat from step 3 until the desired pressure is reached.

6. Close V3 and V5.

C.4 Programming the Tube Furnace

1. Turn on the furnace using the power switch, if it is not already powered on.

2. The programs consist of series of temperature setpoints C01 to CN in °C and time periods t01 to tN in minutes. The program starts at C01, and immediately starts ramping to C02 over the period of time t01. Then, it will start ramping to C03 over the period t02, and so on. Map out your desired temperature profile over time.

3. Push the "←" key to display C01. Set it to room temperature (about 20°C) using the arrow keys. Then push the "Set" key.

4. Set the desired value for t01 using the arrow keys. Then push "Set" again.

5. Set the value for C02, and continue for the remaining setpoints and periods.

6. After the final setpoint, set the next time period to -121. This will end the program, and allow the furnace to cool down to room temperature. Push "Set" one last time. "End" should display in the SV window.

7. Push "←", then cycle through your program with "Set" to check that it has been entered correctly. Continue until "End" is shown again.

8. Start the program by holding "↓" until "run" is displayed after about 2 seconds.

For example, to ramp up to 1000°C over the course of 4 hours, hold that temperature for 3 days, and then cool down to room temperature without temperature control,

1. Set C01 to 20
2. Set t01 to 240
3. Set C02 to 1000
4. Set t02 to 4320
5. Set C03 to 1000
6. Set t03 to -121

The maximum any time period can be is 9999 minutes, or slightly less than 7 days. To anneal for a longer time period, split the time up into multiple periods. For example, to anneal at 1000°C for 10 days,

1. Set C01 to 20
2. Set t01 to 240
3. Set C02 to 1000
4. Set t02 to 7200
5. Set C03 to 1000
6. Set t03 to 7200
7. Set C04 to 1000
8. set t04 to -121

C.5 Collecting the Oxygen-18 Gas

1. Optionally, set the tube furnace to 200°C in order to collect the gas more efficiently.

2. Using a funnel, load liquid nitrogen into the cold trap through the port in the top. Pour the nitrogen slowly, leaving time for the funnel to cool down. Be very careful not to splash any on the quartz tube, especially if it is hot.

3. Open V6. Check that the pressure on P2 is lower than P1.

4. Very slowly open V7, once again being careful not to disturb the alumina spacers. Wait until the pressure at P1 and P2 has equalized.

5. Close V6 and V7.

BIBLIOGRAPHY

[1] Hans Petter Langtangen and Anders Logg. *Solving PDEs in Python*. Springer, 2017.

[2] Y. S. Eo, K. Sun, Ç. Kurdak, D.-J. Kim, and Z. Fisk. Inverted resistance measurements as a method for characterizing the bulk and surface conductivities of three-dimensional topological insulators. *Phys. Rev. Applied*, 9:044006, Apr 2018.

[3] W. Kobayashi, Y. Koizumi, and Y. Moritomo. Large thermal hall coefficient in bismuth. *Applied Physics Letters*, 100(1):011903, 2012.

[4] Herbert Mette. Righi-leduc effect in insb between 25°c and 300°c. *Zeitschrift für Physik*, 176(4):329–335, Dec 1963.

[5] Charles R. Whitsett. Righi-leduc effect in mercuric selenide. *Journal of Applied Physics*, 32(10):2257–2260, 1961.

[6] K. Krishana, N. P. Ong, Y. Zhang, Z. A. Xu, R. Gagnon, and L. Taillefer. Quasiparticle thermal hall angle and magnetoconductance in $\mathrm{YBa_2Cu_3}O_x$. *Phys. Rev. Lett.*, 82:5108–5111, Jun 1999.

[7] Y. Onose, T. Ideue, H. Katsura, Y. Shiomi, N. Nagaosa, and Y. Tokura. Observation of the magnon hall effect. *Science*, 329(5989):297–299, 2010.

[8] Max Hirschberger, Jason W. Krizan, R. J. Cava, and N. P. Ong. Large thermal hall conductivity of neutral spin excitations in a frustrated quantum magnet. *Science*, 348(6230):106–109, 2015.

[9] P. W. Bridgman. The connections between the four transverse galvanomagnetic and thermomagnetic phenomena. *Phys. Rev.*, 24:644–651, Dec 1924.

[10] Neil Ashcroft and David Mermin. *Solid State Physics*. Brooks/Cole, 1976.

[11] Lifa Zhang, Jie Ren, Jian-Sheng Wang, and Baowen Li. The phonon hall effect: theory and application. *Journal of Physics: Condensed Matter*, 23(30):305402, 2011.

[12] Michiyasu Mori, Alexander Spencer-Smith, Oleg P. Sushkov, and Sadamichi Maekawa. Origin of the phonon hall effect in rare-earth garnets. *Phys. Rev. Lett.*, 113:265901, Dec 2014.

[13] Peter J. Tausch and R. S. Newrock. High-field righi-leduc effect and lattice thermal conductivity of potassium. *Phys. Rev. B*, 16:5381–5389, Dec 1977.

[14] R. Fletcher and J. L. Opsal. Comment on "high-field righi-leduc effect and lattice thermal conductivity of potassium". *Phys. Rev. B*, 20:2555–2555, Sep 1979.

[15] P. J. Tausch and R. S. Newrock. Reply to "comment on 'high-field righi-leduc effect and lattice thermal conductivity of potassium"'. *Phys. Rev. B*, 20:2556–2557, Sep 1979.

[16] E. H. Putley. *Hall Effect and Related Phenomena*. Butterworths, 1960.

[17] A. L. Jain and S. H. Koenig. Electrons and holes in bismuth. *Phys. Rev.*, 127:442–446, Jul 1962.

[18] Ralph Rosenbaum and Jean Galibert. Hall coefficient measurements at high perpendicular magnetic fields in polycrystalline bismuth films. *Physica B: Condensed Matter*, 346-347:287 – 290, 2004. Proceedings of the 7th International Symposium on Research in High Magnetic Fields.

[19] C. F. Gallo, B. S. Chandrasekhar, and P. H. Sutter. Transport properties of bismuth single crystals. *Journal of Applied Physics*, 34(1):144–152, 1963.

[20] Jmol: an open-source java viewer for chemical structures in 3d. http://jmol.sourceforge.net, 2019.

[21] Fair Yang, Kai Liu, Kimin Hong, D H. Reich, Peter Searson, Chia-Ling Chien, Yamin Leprince-Wang, Kui Yu-Zhang, and Ke Han. Shubnikov–de haas oscillations in electrodeposited single-crystal bismuth films. *Physical Review B*, 61, 01 2001.

[22] D. Shoenberg. *Magnetic oscillations in metals*. Cambridge University Press, 1984.

[23] Lu Li, J. G. Checkelsky, Y. S. Hor, C. Uher, A. F. Hebard, R. J. Cava, and N. P. Ong. Phase transitions of dirac electrons in bismuth. *Science*, 321(5888):547–550, 2008.

[24] Jack Ekin. *Experimental Techniques for Low-Temperature Measurement: Cryostat Design, Material Properties and Superconductor Critical-Current Testing*. Oxford University Press, 10 2006.

[25] B. L. Brandt, D. W. Liu, and L. G. Rubin. Low temperature thermometry in high magnetic fields. vii. cernox™ sensors to 32 t. *Review of Scientific Instruments*, 70(1):104–110, 1999.

[26] Hirschberger. Max. *Quasiparticle Excitations with Berry Curvature in Insulating Magnets and Weyl Semimetals*. PhD thesis, Princeton University, 2017.

[27] R. C. Neville, B. Hoeneisen, and C. A. Mead. Permittivity of strontium titanate. *Journal of Applied Physics*, 43(5):2124–2131, 1972.

[28] F. Jona and G. Shirane. *Ferroelectric Crystals*. Pergamon, 1962.

[29] S. E. Rowley. *Quantum Phase Transitions in Ferroelectrics*. PhD thesis, cambridge University, 2010.

[30] S. E. Rowley, L. J. Spalek, R. P. Smith, M. P. M. Dean, M. Itoh, J. F. Scott, G. G. Lonzarich, and S. S. Saxena. Ferroelectric quantum criticality. *Nature Physics*, 10:367 EP –, Mar 2014. Article.

[31] Piers Coleman and Andrew J. Schofield. Quantum criticality. *Nature*, 433(7023):226–229, 2005.

[32] Lake shore cryotronics, inc. http://www.lakeshore.com/, 2019. Accessed: 2019-9-9.

[33] MTI Corporation. http://mtixtl.com/, 2016. Accessed: 2016-5-31.

[34] G Heine and W Lang. Magnetoresistance of the new ceramic "cernox" thermometer from 4.2k to 300k in magnetic fields up to 13t. *Cryogenics*, 38(4):377 – 379, 1998.

[35] R.G Goodrich, Donavan Hall, Eric Palm, and Tim Murphy. Magnetoresistance below 1k and temperature cycling of ruthenium oxide–bismuth ruthenate cryogenic thermometers. *Cryogenics*, 38(2):221 – 225, 1998.

[36] California Fine Wire Company. http://www.calfinewire.com/, 2016. Accessed: 2016-5-31.

[37] G. K. White and S. B. Woods. The thermal and electrical resistivity of bismuth and antimony at low temperatures. *The Philosophical Magazine: A Journal of Theoretical Experimental and Applied Physics*, 3(28):342–359, 1958.

[38] Sigma-Aldrich Oxygen-$^{18}O_2$. https://www.sigmaaldrich.com/catalog/product/aldrich/602892?lang=en&region=US, 2016. Accessed: 2016-8-25.

[39] Ilaria Pallecchi, Giuseppe Grassano, Daniele Marré, Luca Pellegrino, Marina Putti, and Antonio Sergio Siri. Srtio3-based metal–insulator–semiconductor heterostructures. *Applied Physics Letters*, 78(15):2244–2246, 2001.

[40] *AH2700A 50Hz - 20 kHz Ultra-Precision Capacitance Bridge Operation and Maintenance Model*. Andeen-Hagerling, 2003.

[41] W. F. Giauque and J. W. Stout. The entropy of water and the third law of thermodynamics. the heat capacity of ice from 15 to 273°k. *Journal of the American Chemical Society*, 58(7):1144–1150, Jul 1936.

[42] P.W. Anderson. Resonating valence bonds: A new kind of insulator? *Materials Research Bulletin*, 8(2):153 – 160, 1973.

[43] Tomoya Asaba, Tian-Heng Han, B. J. Lawson, F. Yu, C. Tinsman, Z. Xiang, G. Li, Young S. Lee, and Lu Li. High-field magnetic ground state in $s = \frac{1}{2}$ kagome lattice antiferromagnet $\mathrm{zncu_3(OH)_6cl_2}$. *Phys. Rev. B*, 90:064417, Aug 2014.

[44] S. A. Owerre. Topological thermal hall effect in frustrated kagome antiferromagnets. *Phys. Rev. B*, 95:014422, Jan 2017.

[45] Hayato Doki, Masatoshi Akazawa, Hyun-Yong Lee, Jung Hoon Han, Kaori Sugii, Masaaki Shimozawa, Naoki Kawashima, Migaku Oda, Hiroyuki Yoshida, and Minoru Yamashita. Spin thermal hall conductivity of a kagome antiferromagnet. *Phys. Rev. Lett.*, 121:097203, Aug 2018.

[46] Y. Kasahara, K. Sugii, T. Ohnishi, M. Shimozawa, M. Yamashita, N. Kurita, H. Tanaka, J. Nasu, Y. Motome, T. Shibauchi, and Y. Matsuda. Unusual thermal hall effect in a kitaev spin liquid candidate $\alpha-\mathrm{rucl_3}$. *Phys. Rev. Lett.*, 120:217205, May 2018.

[47] Hiroshi Kageyama. *An Experimental Realization of the Shastry-Sutherland Model*, pages 611–651. Springer Berlin Heidelberg, Berlin, Heidelberg, 2005.

[48] Shin Miyahara and Kazuo Ueda. Exact dimer ground state of the two dimensional heisenberg spin system $\mathrm{srcu_2(bo_3)_2}$. *Phys. Rev. Lett.*, 82:3701–3704, May 1999.

[49] Shin Miyahara and Kazuo Ueda. *J. Phys. Soc. Jpn. (Suppl.)*, page 72, 2000.

[50] P. A. McClarty, F. Krüger, T. Guidi, S. F. Parker, K. Refson, A. W. Parker, D. Prabhakaran, and R. Coldea. Topological triplon modes and bound states in a shastry-sutherland magnet. *Nature Physics*, 13:736 EP –, May 2017.

[51] Guillermo Jorge, Raivo Stern, M Jaime, Neil Harrison, J Bonča, Samir El Shawish, Cristian Batista, Hanna Dabkowska, and B D. Gaulin. Crystal symmetry and high-magnetic-field specific heat of srcu2(bo3)(2). *Phys. Rev. B*, 71, 03 2005.

[52] M. Hofmann, T. Lorenz, G. S. Uhrig, H. Kierspel, O. Zabara, A. Freimuth, H. Kageyama, and Y. Ueda. Strong damping of phononic heat current by magnetic excitations in $\mathrm{srcu_2(bo_3)_2}$. *Phys. Rev. Lett.*, 87:047202, Jul 2001.

[53] Liang Fu, C. L. Kane, and E. J. Mele. Topological insulators in three dimensions. *Phys. Rev. Lett.*, 98:106803, Mar 2007.

[54] D. Hsieh, D. Qian, L. Wray, Y. Xia, Y. S. Hor, R. J. Cava, and M. Z. Hasan. A topological dirac insulator in a quantum spin hall phase. *Nature*, 452:970 EP –, Apr 2008.

[55] James R. Munkres. *Topology*. Prentice-Hall, 2000.

[56] John M. Lee. *Riemannian Manifolds: An Introduction to Curvature*. Springer, 1997.

[57] Michael Victor Berry. Quantal phase factors accompanying adiabatic changes. *Proceedings of the Royal Society of London. A. Mathematical and Physical Sciences*, 392(1802):45–57, 1984.

[58] G. Li, Z. Xiang, F. Yu, T. Asaba, B. Lawson, P. Cai, C. Tinsman, A. Berkley, S. Wolgast, Y. S. Eo, Dae-Jeong Kim, C. Kurdak, J. W. Allen, K. Sun, X. H. Chen, Y. Y. Wang, Z. Fisk, and Lu Li. Two-dimensional fermi surfaces in kondo insulator smb6. *Science*, 346(6214):1208–1212, 2014.

[59] Judit Romhányi, Karlo Penc, and R. Ganesh. Hall effect of triplons in a dimerized quantum magnet. *Nature Communications*, 6:6805 EP –, Apr 2015. Article.

[60] Di Xiao, Ming-Che Chang, and Qian Niu. Berry phase effects on electronic properties. *Rev. Mod. Phys.*, 82:1959–2007, Jul 2010.

[61] Luke Prichard-Cairns, Jean Philippe Reid, Robin S. Perry, Dharmalingam Prabhakaran, and Andrew Huxley. Thermal hall effect measurements on topological materials. APS March Meeting 2019, 2019.

[62] Christian Knetter, Alexander Bühler, Erwin Müller-Hartmann, and Götz S. Uhrig. Dispersion and symmetry of bound states in the shastry-sutherland model. *Phys. Rev. Lett.*, 85:3958–3961, Oct 2000.

[63] Christopher A. Pocs, Ian A. Leahy, Hao Zheng, Gang Cao, Eun-Sang Choi, S. H. Do, Kwang-Yong Choi, B. Normand, and Minhyea Lee. Giant thermal magnetoconductivity in $CrCl_3$ and a general model for spin-phonon scattering. *arXiv e-prints*, page arXiv:1908.07004, Aug 2019.

[64] S. Haravifard, D. Graf, A. E. Feiguin, C. D. Batista, J. C. Lang, D. M. Silevitch, G. Srajer, B. D. Gaulin, H. A. Dabkowska, and T. F. Rosenbaum. Crystallization of spin superlattices with pressure and field in the layered magnet srcu2(bo3)2. *Nature Communications*, 7:11956 EP –, Jun 2016. Article.

[65] Marcelo Jaime, Ramzy Daou, Scott A. Crooker, Franziska Weickert, Atsuko Uchida, Adrian E. Feiguin, Cristian D. Batista, Hanna A. Dabkowska, and Bruce D. Gaulin. Magnetostriction and magnetic texture to 100.75 tesla in frustrated srcu2(bo3)2. *Proceedings of the National Academy of Sciences*, 109(31):12404–12407, 2012.

[66] Y. H. Matsuda, N. Abe, S. Takeyama, H. Kageyama, P. Corboz, A. Honecker, S. R. Manmana, G. R. Foltin, K. P. Schmidt, and F. Mila. Magnetization of $\mathrm{srcu_2(bo_3)_2}$ in ultrahigh magnetic fields up to 118 t. *Phys. Rev. Lett.*, 111:137204, Sep 2013.

[67] T. M. Rice. To condense or not to condense. *Science*, 298(5594):760–761, 2002.